

## **ABSTRACT**

LAMONDS, DONALD LUCAS. Surface Finish and Form fidelity in Diamond Turning.  
(Under the direction of Thomas A. Dow.)

Fabrication of imaging systems requires nanometer precision of the optical form and micrometer precision in the position of that surface relative to the imaging system. To gain experience with production of optical systems and prepare for non-rotationally symmetric systems, a two-mirror axisymmetric Richey-Chrétien telescope was fabricated with a diamond turning machine; based on the measurements of the telescope, further modeling and experimentation was done to verify the form-error capability of the machine and surface finish with machine vibration.

Optical flats were fabricated in a fashion that revealed the error motions of the diamond turning machine. Squareness between the axes was found as the dominating error and compensation was first attempted by setting the tool path equal to the inverse of the error. Automatic error correction routines written prior to this work were re-activated and the correct squareness compensation was input. Several optical flats were fabricated using different tool locations on the DTM and all measurements showed traces at  $\lambda/4$ . A sphere was then fabricated that had less the  $\lambda/4$  form error with optical power (spherical radius error) removed and the spherical radius was within 6  $\mu\text{m}$  of the target. When observing the conditions described in this work, optical surfaces can repeatedly be fabricated with error levels of  $\lambda/4$ .

Initial surface finish tests were conducted at machining rates where the parabolic approximation should accurately predict peak-to-valley surface finish. These tests were designed to check for surface finish dependence on cutting depth, surface speed, and cross-feed rate. Results indicated that finish was dependant on cross feed-rate but that there were other factors causing increased roughness. Further examination of the results showed that machine vibration and minimum chip thickness (a variable dependant on tool edge sharpness) were adding to roughness. A model was created to predict surface roughness influenced by machine vibration and experiments to prove the model used a freshly sharpened tool. The model results predicted that surface finish can be improve beyond the vibration amplitude of the machine as did the experimental results. The model was expanded to further improve the finish quality by dithering the tool in the cross-feed direction such that diffraction patterns from diamond turned cusps were smooth rather than periodic. Scatter measurements were taken from the workpiece used in machine tests vibrations tests and it was found that the desired effects of tool dithering were present in the lower, optical surface quality feed-rates ( $1\text{-}2 \mu\text{m/rev}$ ). This result invalidated the need for optical-quality feed rates.

# Surface Finish and Form Fidelity in Diamond Turning

by  
Donald Lucas Lamonds

A thesis submitted to the Graduate Faculty of  
North Carolina State University  
In partial fulfillment of the  
requirements for the Degree of  
Master of Science

Mechanical and Aerospace Engineering

Raleigh, NC

2008

APPROVED BY:

---

Gregory D. Buckner

---

Ronald O. Scattergood

---

Thomas A. Dow  
Advisory Committee Chair

## **DEDICATION**

To Laura, whose patience was greater than any and whose love I did, and will eternally appreciate.

## **BIOGRAPHY**

D. Lucas Lamonds was born in Winston-Salem, NC and was raised in Mocksville, NC. He graduated from Davie County High School in the spring of 1997 and attended North Carolina State University in the fall. While attending NC State, he had internships with AMP, R.J. Reynolds machine shop and Getrag Gears LLC. Lucas graduated from NC State in 2002 with a Bachelor of Science in Mechanical Engineering. After graduation, he then began employment with Getrag Gears LLC in Charleston SC as a quality and manufacturing engineer. In January 2005, Lucas returned to NC State University to start work on a Masters Degree in Mechanical Engineer under Dr. Dow.

## **ACKNOWLEDGMENTS**

I would like to thank everyone who help me along the way. Acknowledgments

- Dr Dow, For his direction, drive, knowledge and scientific mentality.
- Ken Garrard and Alex Sohn, For their proficiency all the equipment, sharing their past PEC experiences and for fascinating discussions.
- Nadim Wanna and Rob Woodside, For their camaraderie in classes, at the PEC and away from NC State.
- The students at the PEC, Dave, Kara, Tim, Chen, For Friday lunches and relieving conversations.
- Laura, For her unwavering support.
- Mom and Dad, For their steady support and motivational talks.

# TABLE OF CONTENTS

|  |             |
|--|-------------|
| <b>LIST OF FIGURES.....</b>                                    | <b>ix</b>   |
| <b>LIST OF TABLES.....</b>                                     | <b>xvii</b> |
| <b>1 INTRODUCTION .....</b>                                    | <b>1</b>    |
| 1.1 BACKGROUND .....   | 1           |
| 1.2 PREVIOUS RESEARCH .....                                    | 2           |
| 1.3 PREVIOUS RESEARCH AT THE PEC .....                         | 3           |
| 1.4 PROBLEM STATEMENT .....                                    | 4           |
| <b>2 FABRICATION OF TWO MIRROR TELESCOPE.....</b>              | <b>6</b>    |
| 2.1 INTRODUCTION .....   | 6           |
| 2.2 MATERIAL PREPARATION .....                                 | 10          |
| 2.2.1 <i>Rough Machining</i> .....                             | 10          |
| 2.2.2 <i>Heat Treatment</i> .....                              | 11          |
| 2.2.3 <i>Material Hardness</i> .....                           | 11          |
| 2.3 DTM SETUP.....   | 13          |
| 2.3.1 <i>DTM Geometry</i> .....                                | 13          |
| 2.3.2 <i>Tooling Setup</i> .....                               | 16          |
| 2.3.3 <i>Tool Alignment to Spindle Centerline</i> .....        | 17          |
| 2.3.4 <i>Tool Z reference</i> .....                            | 28          |
| 2.3.5 <i>Surface Finish, Feed Rate and Spindle Speed</i> ..... | 29          |
| 2.4 CONTROLLER PROGRAMMING .....                               | 31          |
| 2.4.1 <i>Number of Points in the Programmed Path</i> .....     | 31          |
| 2.4.2 <i>Tool Radius Compensation</i> .....                    | 32          |
| 2.4.3 <i>Axes Following Error</i> .....                        | 35          |

|   |           |
|---|-----------|
| 2.5 DIAMOND TURNING OPERATIONS .....  | 38        |
| 2.5.1 <i>Step 1: Vacuum Chuck</i> .....   | 39        |
| 2.5.2 <i>Step 2: Primary Back</i> .....   | 41        |
| 2.5.3 <i>Step 3: Primary Mirror and Fiducial</i> .....                                    | 42        |
| 2.5.4 <i>Step 4: Secondary Mirror and Fiducial</i> .....                                  | 45        |
| 2.5.5 <i>Step 5: Tube</i> .....   | 51        |
| 2.5.6 <i>Step 6: Spacer</i> .....   | 54        |
| 2.5.7 <i>Machining Results, Discussion and Suggestions for the Future</i> .....           | 54        |
| 2.6 CONCLUSIONS.....  | 57        |
| <b>3 FORM ERROR OF ASG 2500 DIAMOND TURNING MACHINE.....</b>                              | <b>59</b> |
| 3.1 INTRODUCTION .....  | 59        |
| 3.2 DTM ERROR BUDGET.....   | 60        |
| 3.2.1 <i>Environment</i> .....  | 60        |
| 3.2.2 <i>Machine Geometry: Slide Straightness and Automatic Compensation</i> .....        | 61        |
| 3.2.3 <i>Thermal Growth of Spindle</i> .....  | 64        |
| 3.3 DIAMOND TURNED FLATS.....   | 65        |
| 3.3.1 <i>Yaw Error, Squareness of Spindle to X-axis and Automatic Compensation</i> .....  | 66        |
| 3.3.2 <i>Optical Flat Test Results</i> .....  | 68        |
| 3.3.3 <i>Table 3-1, Tests 1-4: Manual Compensation</i> .....                              | 73        |
| 3.3.4 <i>Table 3-1, Tests 5-16: Automatic Compensation</i> .....                          | 75        |
| 3.3.5 <i>Squareness Setting Revisited by Comparison with a Larger Diameter Flat</i> ..... | 75        |
| 3.3.6 <i>Table 3-1, Tests 17-20: Final Yaw and Squareness Setting</i> .....               | 78        |
| 3.4 DIAMOND TURNED SPHERE .....   | 80        |
| 3.5 CONCLUSIONS.....  | 83        |
| <b>4 SURFACE ROUGHNESS IN DIAMOND TURNING.....</b>  | <b>86</b> |
| 4.1 INTRODUCTION .....  | 86        |

|  |            |
|--|------------|
| <b>4.2 SURFACE FINISH EXPERIMENTS IN FIRST-ORDER REGIME WITH VARIATION OF SECOND-ORDER FACTORS .....</b>               | <b>87</b>  |
| 4.2.1 <i>Surface Finish Variables</i> .....  | 89         |
| 4.2.2 <i>Experimental Setup and Part Planning</i> .....  | 93         |
| 4.2.3 <i>Surface Speed Effects</i> .....   | 100        |
| 4.2.4 <i>Depth of Cut Effect</i> .....   | 103        |
| 4.2.5 <i>Cross-Feed Rate Effect</i> .....  | 105        |
| 4.2.6 <i>Groove Comparison with Instant Depth of Cut Change</i> .....  | 107        |
| 4.2.7 <i>Features in the Cutting Direction</i> .....   | 112        |
| 4.2.8 <i>Conclusions</i> .....   | 114        |
| <b>4.3 MACHINE VIBRATION .....</b>   | <b>115</b> |
| 4.3.1 <i>Vibration Motion in Diamond Turning Machines</i> .....  | 117        |
| 4.3.2 <i>Surface Finish Model with Vibration</i> .....   | 124        |
| 4.3.3 <i>Experimental Results and Discussion</i> .....   | 132        |
| 4.3.4 <i>Conclusions</i> .....   | 145        |
| <b>4.4 CROSS-FEED TOOL DITHERING TO REDUCE DIFFRACTION FROM DIAMOND TURNED CUSPS.....</b>                              | <b>146</b> |
| 4.4.1 <i>Principles of Optical Scattering from Diamond Turned Surfaces</i> .....                                       | 146        |
| 4.4.2 <i>Cross Feed Dither Model</i> .....   | 155        |
| 4.4.3 <i>Analytical Model Analysis</i> .....   | 157        |
| 4.4.4 <i>Predicted Machining Conditions</i> .....  | 165        |
| 4.4.5 <i>Scatter Measurements of a First Surface Mirror and Diamond Turned Grooves without Cross Feed Dither</i> ..... | 167        |
| 4.4.6 <i>Conclusions</i> .....   | 175        |
| <b>5 CONCLUSIONS AND FUTURE WORK .....</b>   | <b>176</b> |
| <b>5.1 FORM FIDELITY .....</b>   | <b>176</b> |
| 5.1.1 <i>Hyperbolic Mirrors and Fiducial Features</i> .....  | 176        |
| 5.1.2 <i>Flat and Spherical Surfaces</i> .....   | 177        |

|   |            |
|---|------------|
| 5.2 SURFACE FINISH .....  | 178        |
| 5.2.1 <i>PV Approximation Regime Test with Servo</i> .....                        | 178        |
| 5.2.2 <i>Machine Vibration</i> .....  | 179        |
| 5.2.3 <i>Cross-feed Tool Dithering</i> .....                                      | 179        |
| <b>REFERENCES.....</b>  | <b>181</b> |
| <b>6 APPENDIX .....</b>   | <b>187</b> |
| 6.1 APPENDIX A: MATLAB PROGRAMS .....   | 188        |
| 6.1.1 <i>Surface finish model with machine vibration and tool dithering</i> ..... | 188        |
| 6.1.2 <i>Hilbert Transform with Decay Fit and Autocovariance</i> .....            | 190        |
| 6.1.3 <i>Theoretical Tool Nose Radius &amp; DOC Alignment</i> .....               | 192        |
| 6.1.4 <i>Two Mirror Scripts</i> .....   | 195        |
| 6.1.5 <i>Spiral Alignment for Vibration Analysis</i> .....                        | 197        |
| 6.2 APPENDIX B: ASG-2500 DTM PROGRAMS FOR TWO MIRROR .....                        | 198        |
| 6.3 APPENDIX C: TWO MIRROR DRAWINGS .....   | 202        |

# LIST OF FIGURES

|  |    |
|--|----|
| FIGURE 2-1: ROUGH MACHINED COMPONENTS OF THE TWO-MIRROR TELESCOPE.....   | 7  |
| FIGURE 2-2: THE OPTICAL PATH OF THE RICHEY-CHRÉTIEN TELESCOPE WITH OPTICAL ELEMENTS AND<br>SPECIFICATIONS. INCIDENT LIGHT FROM THE OBJECT (INFINITE CONJUGATES) ENTERS FROM THE LEFT<br>AND THE IMAGE IS FORMED ON THE RIGHT. PATH GENERATED WITH OSLO-EDU® FROM LAMBDA<br>RESEARCH CORPORATION..... | 8  |
| FIGURE 2-3: CROSS SECTION OF TELESCOPE COMPONENTS WITH DARK LINES INDICATING SURFACES THAT<br>WERE DIAMOND TURNED. DASHED LINE SHOWS THE COMMON AXIS OF SYMMETRY/ROTATION.....   | 9  |
| FIGURE 2-4: FINAL ASSEMBLED OPTICAL SYSTEM.....  | 10 |
| FIGURE 2-5: RANK-PNEUMO ASG-2500 DIAMOND TURNING MACHINE.....  | 15 |
| <b>FIGURE 2-6:</b> FABRICATION OF RICHEY-CHRÉTIEN TELESCOPE COMPONENTS ON THE ASG-2500 DTM WITH<br>A DASHED LINE TO SHOW THE COLLINEAR OPTICAL, TUBE AND SPINDLE AXES.....   | 16 |
| FIGURE 2-7: TOOL LAYOUT ON THE DTM ILLUSTRATING THE RELATIVE LOCATION OF THE TWO TOOLS AND<br>THE 10X TELESCOPE (BLACK CYLINDER ON RIGHT OF PHOTO). .....  | 17 |
| FIGURE 2-8: OGIVE ERROR CAUSED BY TOOL GOING PAST SPINDLE CENTER IN X DIRECTION.....   | 18 |
| FIGURE 2-9: CENTERING PLUG MOUNTED IN HOLDER, WHICH IS VACUUMED TO CHUCK.....  | 20 |
| FIGURE 2-10: HEIGHT GAGE USED TO SET THE DIAMOND TOOL HEIGHT (Y-DIRECTION) AT SETUP. THE<br>DIAMOND IS RAISED INTO GAGE TIP BY TURNING THE KNOB ON THE TOOL POST.....  | 21 |
| FIGURE 2-11: TWO DIAMOND TURNED GROOVES CUT IN THE END OF A CENTERING PLUG.....  | 22 |
| FIGURE 2-12: SCREEN CAPTURE OF THE NEW VIEW MEASUREMENT SHOWING A CENTERING ERROR IN THE<br>VERTICAL DIRECTION (Y). THE CYLINDRICAL SHAPE INDICATES THE TOOL WAS LOW OF CENTERLINE.<br>.....   | 24 |
| FIGURE 2-13: SCREEN CAPTURE OF THE NEW VIEW MEASUREMENT SHOWING A CENTERING ERROR IN THE<br>VERTICAL DIRECTION (Y). THE CONE SHAPE INDICATES THE TOOL WAS HIGH OF CENTERLINE. ....   | 25 |

|   |    |
|---|----|
| FIGURE 2-14: SPIRAL AT CENTER OF WORKPIECE WHERE RADIAL LINES CREATED BY SPINDLE AIR-BEARING PADS ARE VISIBLE. DARK LINES HIGHLIGHT TWO OPPOSING MARKS THAT, WITH COUNTER CLOCKWISE SPINDLE ROTATION, INDICATE TOOL WAS LOW.....  | 26 |
| FIGURE 2-15: CROSS SECTIONAL ERROR SHAPES FOR A CENTERING PLUG SPHERE IN THE HORIZONTAL DIRECTION (X).....  | 27 |
| FIGURE 2-16: SCREEN SHOT OF GPI OUTPUT SHOWING A CENTERING ERROR IN THE HORIZONTAL DIRECTION (X) WHERE THE TOOL WAS LONG OF CENTER. TRACE SHAPE SEEN IN FIGURE 2-15A.....   | 28 |
| FIGURE 2-17: ILLUSTRATION OF SURFACE NORMAL VECTORS AND TOOL OFFSET TO FORM DISCRETE TOOL PATH. DESIRED SURFACE IS A CONTINUOUS FUNCTION AND THE NORMAL VECTOR LENGTH IS EQUAL TO THE TOOL RADIUS.....  | 32 |
| FIGURE 2-18: CROSS-SECTION OF DESIRED PRIMARY OPTICAL SURFACE (SOLID LINE) AND TOOL RADIUS COMPENSATED MACHINING PATH (DASHED LINE) WITH CIRCLES REPRESENTING THE TOOL RADIUS. TO SCALE.....  | 34 |
| FIGURE 2-19: PRIMARY (UPPER) AND SECONDARY (LOWER) MIRROR MOTION PLOTS DRAWN BY K. GARRARD. THE CIRCLES (O) IDENTIFY THE UNCOMPENSATED TOOL PATH WHILE LINES PASSING THROUGH THE CIRCLES LABELED <i>HYPERBOLA</i> ARE THE SURFACE AS SPECIFIED BY THE OPTICAL DESIGN. LINES LABELED <i>TOOL PATH</i> ARE THE TOOL RADIUS COMPENSATED PATH. .... | 35 |
| FIGURE 2-20: PRIMARY (LEFT) AND SECONDARY (RIGHT) MIRROR MOTION PATH ERROR FILTERED WITH 100 POINT MOVING AVERAGE BY K GARRARD. THIS SHOWS THE DIFFERENCE BETWEEN COMMANDED PATH AND THE ACTUAL PATH AS MEASURED BY THE LASER INTERFEROMETER FEEDBACK OF THE ASG-2500 CONTROL SYSTEM.....   | 37 |
| FIGURE 2-21: VACUUM CHUCK FLATNESS (LEFT) AND RUNOUT (RIGHT) AS MEASURED FOR TWO MIRROR FABRICATION.....  | 40 |
| FIGURE 2-22: DIAMOND TURNED PRIMARY BACK. CENTER PLUG IS RUBBER. ....   | 42 |
| FIGURE 2-23: PRIMARY OPTICAL AND FIDUCIAL CUTTING PATHS.....  | 44 |
| FIGURE 2-24: CROSS-SECTION OF PRIMARY SHOWING CRITICAL FIDUCIAL FEATURES. SURFACES CUT ARE DRAWN WITH BOLD LINES. ....  | 45 |

|   |    |
|---|----|
| FIGURE 2-25: SECONDARY MIRROR AND SUPPORT STRUCTURE AFTER DIAMOND TURNING. ....   | 46 |
| FIGURE 2-26: SECONDARY ON VACUUM CHUCK WITH VACUUM PLATE. CRITICAL FIDUCIAL SURFACES ARE<br>IN BOLD.....  | 47 |
| FIGURE 2-27: DIGITIZED SECONDARY BACK. OUTER RING REPRESENTS THE BACK OF THE FIDUCIAL STEP.<br>CENTER CLUSTER IS THE MIRROR BACK. POINTS ALONG THE THREE LEGS SHOWN FOR CLARITY.....  | 49 |
| FIGURE 2-28: CROSS SECTION OF SECONDARY MIRROR STRUCTURE ILLUSTRATING THE 20 $\mu\text{m}$ OFFSET<br>BETWEEN THE MIRROR BACK AND THE OUTER RING. ....   | 49 |
| FIGURE 2-29: TUBE CROSS SECTION SHOWING RADIAL SEATING SURFACES AND AXIAL SEATING SURFACES.   | 52 |
| FIGURE 2-30: MACHINING THE TUBE WITH DTM. ....  | 53 |
| FIGURE 3-1: GEOMETRICAL LAYOUT OF THE ASG-2500 SLIDES WITH DIRECTIONS LABELED. Z<br>INTERFEROMETER IS NEXT TO THE SPINDLE AND X INTERFEROMETER IS RIGHT OF TOOL HOLDER; FOR<br>CLARITY, THE INTERFEROMETER MOUNTING PLATES AND OIL GUARDS ARE NOT SHOWN. .... | 62 |
| FIGURE 3-2: X AND Z-AXIS STRAIGHTNESS (NOTE SCALE DIFFERENCE) WITH (SOLID LINE) AND WITHOUT<br>(DASHED LINE) COMPENSATION FROM THE ORTHOGONAL SLIDE. [4] .....  | 63 |
| FIGURE 3-3: TOOL PATH AND OIL SPRAY FOR DIAMOND TURNED FLATS EXPERIMENT. TO SCALE.....  | 65 |
| FIGURE 3-4: Z-AXIS YAW OVER FULL 150 MM RANGE IS 1.6 ARCSEC. ....   | 67 |
| FIGURE 3-5: ZYGO GPI HPXR FORM MEASURING INTERFEROMETER WITH METROPRO SOFTWARE. ....  | 69 |
| FIGURE 3-6: EXAMPLE TRACE (#13 FROM TABLE 3-1) OF 6061 T-6 FLAT MACHINED ON THE DTM WITH<br>YAW CORRECTION OF 0.7 ARC-SECONDS. ....   | 73 |
| FIGURE 3-7: SLOW VELOCITY X-AXIS MOVE. LINEAR CURVE FIT SLOPE = 0.0165 MM/S. ....   | 74 |
| FIGURE 3-8: FINAL MANUALLY CORRECTED SQUARENESS ERROR SHOWING CONVEX SHAPE.....   | 74 |
| FIGURE 3-9: COMPARISON OF 6061 WORKPIECE AND THE FINAL SHAPE OF THE FLAT TESTS. ....  | 76 |
| FIGURE 3-10: 6061-T6 WORKPIECE WITH 150 MM OPTICAL SURFACE DIAMETER. UPPER LEFT CORNER<br>TRIMMED OUT BECAUSE IT WAS NOT MACHINED DURING THIS PASS.....   | 78 |
| FIGURE 3-11: FINAL FLAT MEASUREMENT FROM GPI WITH FINAL SQUARENESS CORRECTION. PV ERROR OF<br>183 NM OR 0.29 $\lambda$ . ....   | 79 |

|   |     |
|---|-----|
| FIGURE 3-12: ZYGO GPI FORM MEASURING LASER INTERFEROMETER STAGE FITTED WITH A LENGTH<br>MEASURING INTERFEROMETER.....   | 81  |
| FIGURE 3-13: INTERFEROGRAM SEEN WHEN THE GPI FOCUS IS ALIGNED WITH THE APEX OF THE SPHERE<br>USING THE “CAT’S EYE” TECHNIQUE. POWER IS ALMOST ZERO ( $0.037 \lambda = 23$ NM RADIUS).<br>HORIZONTAL AND VERTICAL SCALES SHOULD BE IGNORED BECAUSE THIS MEASUREMENT IS AN<br>INTERFEROGRAM OF A SPOT (APEX OF THE SPHERE).....             | 82  |
| FIGURE 3-14: SPHERE MEASUREMENT WITH POWER REMOVED. PV ERROR WAS 150 NM OR $\Delta/4$ . ....  | 83  |
| FIGURE 4-1: TRANSITION FROM $2 \mu\text{m}$ CUTTING DEPTH TO $1 \mu\text{m}$ AT $37.7 \mu\text{m}/\text{REV}$ FEED RATE, AND $1.1 \text{ m/s}$<br>SURFACE SPEED IN ELECTROPLATED COPPER WITH A $0.750 \text{ mm}$ RADIUS TOOL. CROSS FEED DIRECTION<br>IS FROM LEFT TO RIGHT IN THIS AND ALL OTHER SURFACE PROFILES IN THIS SECTION. .... | 89  |
| FIGURE 4-2: SECOND-ORDER EFFECT OF MINIMUM CHIP THICKNESS CAUSED BY A WORN TOOL WITH A LARGE<br>EDGE RADIUS [13]......  | 91  |
| FIGURE 4-3: RAKE FACE AREA ENCLOSED BY THE PREVIOUS PASS, TOOL EDGE AND UNCUT SURFACE. THE<br>RATIO OF LENGTH TO HEIGHT IN THIS DRAWING WAS SET TO RESEMBLE FIGURE 4-1 AT<br>APPROXIMATELY 150:1.....   | 92  |
| FIGURE 4-4: DIAMOND TURNING MACHINE WITH FTS FOR INSTANT DEPTH OF CUT CHANGE.....   | 94  |
| FIGURE 4-5: OPEN LOOP RESPONSE OF FTS WITH $40 \text{ mm}$ PZT STACK .....  | 96  |
| FIGURE 4-6: $1 \mu\text{m}$ CUTTING DEPTH CHANGE COMMAND AT A CIRCUMFERENCE OF $125\text{mm}$ . RISE TIME IS $5.3$<br>MS.....   | 97  |
| FIGURE 4-7: EXAMPLE OF TOOL PATH WITH INSTANT DEPTH OF CUT CHANGES. THE ORIGINAL SURFACE IS<br>SEEN AT FAR LEFT AND RIGHT OF THE PROFILE. THE DEEPEST CUT IS ON THE LEFT AND WAS<br>PERFORMED FIRST. THE CUTTING DEPTHS WERE $10 \mu\text{m}$ , $5 \mu\text{m}$ , $2 \mu\text{m}$ AND $1 \mu\text{m}$ .....                               | 99  |
| FIGURE 4-8: SAMPLE NEW VIEW SCAN. TEST 1 AT $5 \mu\text{m}$ DOC. CIRCLES OVERLAIDED ONTO THE SURFACE<br>PROFILE REPRESENT THEORETICAL CUSPS.....  | 101 |
| FIGURE 4-9: ACTUAL AND THEORETICAL SURFACE ROUGHNESS VS. SURFACE SPEED FOR TESTS 1-3 (1.1, 0.3,<br>0.1 M/S, RESPECTIVELY). $F = 37.7 \mu\text{m}/\text{REV}$ .....  | 102 |

|   |     |
|---|-----|
| <b>FIGURE 4-10:</b> ACTUAL AND THEORETICAL SURFACE ROUGHNESS VS. DEPTH OF CUT FOR TESTS 1-3. THREE POINTS AT EACH CUTTING DEPTH FROM TESTS 1-3. $F = 37.7 \mu\text{m}/\text{rev}$ .....   | 104 |
| FIGURE 4-11: ACTUAL AND THEORETICAL PV SURFACE ROUGHNESS VS. FEED RATE FOR TESTS 1-7 IN TABLE 4-1.....  | 105 |
| <b>FIGURE 4-12:</b> ACTUAL AND THEORETICAL RMS SURFACE ROUGHNESS VS. FEED RATE FOR TESTS 1-7 IN TABLE 4-1.....  | 106 |
| FIGURE 4-13: 1 $\mu\text{m}$ DEPTH OF CUT CHANGE FOR 5.33 $\mu\text{m}/\text{rev}$ FEED RATE.....   | 107 |
| FIGURE 4-14: SURFACE PROFILE FROM A 37.7 $\mu\text{m}/\text{rev}$ FEED RATE (TEST 1) SHOWING SEVERAL CUSPS WITH THE LAST GROOVE CUT AT THAT DEPTH BEFORE THE FTS STEPPED THE TOOL UP COMPARED TO THE THEORETICAL PROFILE (SMOOTH LINE). .....   | 109 |
| FIGURE 4-15: SURFACE PROFILE FROM A 5.33 $\mu\text{m}/\text{rev}$ FEED RATE (TEST 4D) SHOWING SEVERAL CUSPS AND THE LAST GROOVE CUT AT THAT DEPTH BEFORE THE FTS STEPPED THE TOOL UP COMPARED TO THE THEORETICAL PROFILE (SMOOTH LINE). THIS GRAPH HAS 10X THE VERTICAL MAGNIFICATION OF FIGURE 4-14.....                             | 109 |
| FIGURE 4-16: 37.7 $\mu\text{m}/\text{rev}$ FEED RATE (TEST 1) ZOOMED TO SHOW ONLY A FEW CUSPS AND COMPARED TO THEORETICAL (SMOOTH LINE). FEED DIRECTION LEFT TO RIGHT.....  | 111 |
| FIGURE 4-17: 11.9 $\mu\text{m}/\text{rev}$ FEED RATE (TEST 4C) WITH CUTTING DEPTH CHANGE COMPARED TO THEORETICAL PROFILE (SMOOTH LINE). ASYNCHRONOUS VIBRATION CAUSED VALLEY-TO-VALLEY VARIATION OF 22 NM. FEED DIRECTION LEFT TO RIGHT.....  | 111 |
| FIGURE 4-18: ORIENTATION OF UP FEED TRACE IN FIGURE 4-19.....   | 112 |
| <b>FIGURE 4-19:</b> TRACE MEASUREMENT IN THE CUTTING DIRECTION (UP-FEED). TOOL MOVED FROM THE LEFT OF THE TRACE TO THE RIGHT. TEST 3: $F = 37.7 \mu\text{m}/\text{rev}$ , CUTTING DEPTH = 5 $\mu\text{m}$ , SURFACE SPEED = 0.085 M/MIN. FEATURE SPACING IS 1.5 $\mu\text{m}$ AS SEEN IN AUTOCOVARIANCE PLOT MENU <i>xPos</i> . ..... | 113 |
| FIGURE 4-20: DIAMOND-TURNED CUSPS FORMING SPIRAL FOUND AT CENTER OF WORKPIECE AFTER LAST TOOL CENTERING ADJUSTMENT. ....  | 120 |
| FIGURE 4-21: CENTER FEATURE FOUND IN FIGURE 4-23 WITH A SPIRAL TRACE ALIGNED TO THE GROOVE BOTTOMS.....   | 121 |

|   |     |
|---|-----|
| FIGURE 4-22: 3D PLOT OF INTERPOLATED POINTS FROM THE SPIRAL TRACE IN FIGURE 4-24.....   | 121 |
| FIGURE 4-23: FREQUENCY RESPONSE OF SPIRAL PROFILE SEEN IN FIGURE 4-24.....  | 122 |
| FIGURE 4-24: X AND $\Theta$ VECTORS OF TOOL CENTER SHOWING MODEL COORDINATE SYSTEM WITH<br>RELATIONSHIP TO WORKPIECE AND ROTATION CENTERLINE.....   | 126 |
| FIGURE 4-25: CERTAIN POINTS FROM MULTIPLE TOOL CUPS (CIRCLES), AT VARYING DEPTHS DUE TO<br>VIBRATION, PRODUCE A FINISHED SURFACE CONTOUR (LINE).....  | 129 |
| FIGURE 4-26: CONSECUTIVE SURFACE CONTOURS IN THE CROSS-FEED DIRECTION (X) WERE STACKED IN THE<br>UP-FEED DIRECTION (Y) INTO A 3-D SURFACE.....  | 130 |
| FIGURE 4-27: AT FINE CROSS-FEED RATES, SOME PASSES OF THE TOOL (+) ARE NOT REPRESENTED IN THE<br>FINISHED SURFACE. THIS PRODUCES A BETTER FINISH THAN WOULD BE EXPECTED FROM THE RMS OF<br>THE VIBRATION ALONE.....                             | 131 |
| FIGURE 4-28: AS THEORETICAL SURFACE FINISH DECREASES, THE EFFECTS OF MACHINE VIBRATION ON<br>SURFACE FINISHED ARE REDUCED. VIBRATION PV = 22 NM AND RMS = 7.7 NM.....   | 132 |
| FIGURE 4-29: TYPICAL SURFACE PROFILE MEASUREMENT ILLUSTRATING THE DEPTH CHANGE AS A RESULT<br>OF VIBRATION WITH LARGE FEED RATE OF 11.3 $\mu\text{m}/\text{rev}$ . THEORETICAL PV = 33 AND THEORETICAL<br>RMS = 10 NM DRAWN WITH BOLD LINE..... | 134 |
| FIGURE 4-30: TYPICAL MEASUREMENTS RESULT IN OBLIQUE PLOT FORM. THIS IS THE SAME SURFACE SHOWN<br>IN FIGURE 4-29.....  | 134 |
| FIGURE 4-31: RESULTS FROM EXPERIMENTAL AND MODEL DATA WITH THRESHOLD OF RMS Z-AXIS<br>VIBRATION, A CURVE TO REPRESENT THE THEORETICAL PARABOLIC RMS SURFACE ROUGHNESS AND A<br>DASHED LINE TO REPRESENT MODEL PREDICTION.....                   | 136 |
| FIGURE 4-32: MEASUREMENT OF 1.13 $\mu\text{m}/\text{rev}$ CROSS-FEED WITH 3D PROFILE, CROSS-FEED TRACE,<br>AUTOCOVARIANCE OF TRACE, AND PSD OF TRACE. GROOVES ARE PRESENT, BUT THERE IS LITTLE<br>INDICATION OF CROSS-FEED.....                 | 138 |
| FIGURE 4-33: MEASUREMENT OF 1.13 $\mu\text{m}/\text{rev}$ CROSS-FEED WITH 3D PROFILE, CROSS-FEED TRACE,<br>AUTOCOVARIANCE OF TRACE, AND PSD OF TRACE. AUTOCOVARIANCE SHOWS RECURRENT FEATURES<br>AT 8X (9 $\mu\text{m}$ ) THE FEED RATE.....    | 139 |

|   |     |
|---|-----|
| FIGURE 4-34: MEASUREMENT OF 1.13 $\mu\text{M}/\text{REV}$ CROSS-FEED WITH 3D PROFILE, CROSS-FEED TRACE,<br>AUTOCOVARIANCE OF TRACE, AND PSD OF TRACE. LITTLE INDICATION OF CROSS-FEED IS SEEN BUT<br>LARGER SPACING IS SHOWN.....   | 140 |
| FIGURE 4-35: MEASUREMENT OF 3.58 $\mu\text{M}/\text{REV}$ CROSS-FEED WITH 3D PROFILE, CROSS-FEED TRACE,<br>AUTOCOVARIANCE OF TRACE, AND PSD OF TRACE. PSD SHOWS SMALL PEAK AT FEED RATE (3.58<br>$\mu\text{M}/\text{REV} = 0.27 \text{ } 1/\mu\text{M})$ .....  | 141 |
| FIGURE 4-36: PSD OF MODELED SURFACE PROFILE WITH 3.58 $\mu\text{M}/\text{REV}$ . VIBRATION AMPLITUDE REDUCED TO<br>9 NM (FROM 11 NM) WHERE A PEAK AT 0.27 $1/\mu\text{M}$ WAS EVIDENT. THIS MATCHES THE PSD IN FIGURE<br>4-35.....  | 142 |
| FIGURE 4-37: MEASUREMENT OF 5.06 $\mu\text{M}/\text{REV}$ CROSS-FEED WITH 3D PROFILE, CROSS-FEED TRACE,<br>AUTOCOVARIANCE OF TRACE, AND PSD OF TRACE. PSD HAS A PEAK AT THE FEED RATE (5.06 $\mu\text{M}/\text{REV}$<br>= 0.20 $1/\mu\text{M})$ .....   | 143 |
| FIGURE 4-38: PSD OF MODELED SURFACE PROFILE WITH 5.06 $\mu\text{M}/\text{REV}$ . VIBRATION AMPLITUDE WAS<br>REDUCED TO 9 NM (WAS 11 NM) WHERE A PEAK AT 0.20 $1/\mu\text{M}$ WAS EVIDENT.....   | 144 |
| FIGURE 4-39: DIFFRACTION PATTERN FROM A SINUSOIDAL SURFACE.....   | 147 |
| FIGURE 4-40: SURFACE PROFILE OF PERFECT DIAMOND TURNED CUSPS. $F = 5 \text{ } \mu\text{M}/\text{REV}$ , $R = 570 \text{ } \mu\text{M}$ , $PV =$<br>5.4 NM AND $RMS = 1.6 \text{ NM}$ .....  | 151 |
| FIGURE 4-41: AUTOCOVARIANCE FOR SURFACE IN FIGURE 4-40.....   | 152 |
| FIGURE 4-42: LOG OF PSD NORMALIZED FOR THE MAXIMUM PEAK FROM AUTOCOVARIANCE IN 4-41. FIRST<br>PEAK IS AT 0.2 FEATURES/ $\mu\text{M}$ OR 5 $\mu\text{M}/\text{FEATURE}$ .....  | 152 |
| FIGURE 4-43: SCATTER PATTERNS FOR VARIOUS SURFACE PROFILES.....   | 154 |
| FIGURE 4-44: EXAMPLE OF DITHER CONCEPT (WITHOUT MACHINE VIBRATION DISTURBING THE CUSPS IN THE<br>Z-DIRECTION) SHOWING APEX OF TOOL (+) MOVED FROM REGULARLY SPACED INTERVALS (CROSS-<br>FEED) AND RESULTANT CONTOUR OF CIRCULAR CUSPS. A 570 $\mu\text{M}$ NOSE RADIUS TOOL WAS USED WITH<br>A 5 $\mu\text{M}/\text{REV}$ CROSS FEED. $PV = 10 \text{ NM}$ AND $RMS = 2.4 \text{ NM}$ ..... | 156 |
| FIGURE 4-45: SAMPLE 3D SURFACE PROFILE WITH CROSS FEED DITHERING (MOTION ALONG THE X-AXIS<br>AND Z-AXIS MACHINE VIBRATION).....   | 157 |

|  |     |
|--|-----|
| FIGURE 4-46: SURFACE PROFILE FOR AUTOCOVARIANCE SEEN IN FIGURE 4-47. $F = 5 \mu\text{M}/\text{REV}$ AND $R = 570$<br>$\mu\text{M}$ .....   | 160 |
| FIGURE 4-47: AUTOCOVARIANCE OF THEORETICAL PROFILE IN FIGURE 4-43 WHERE $F=5 \mu\text{M}/\text{REV}$ , $R = 570$<br>$\mu\text{M}$ , $PV=5.5 \text{ NM}$ , $RMS = 1.6 \text{ NM}$ , $G(0) = RMS^2 = 2.56 \text{ NM}^2$ .....  | 161 |
| FIGURE 4-48: AUTOCOVARIANCE (DOTS), HILBERT TRANSFORM (SOLID) AND EXPONENTIAL DECAY FIT<br>(DASHED) OF FIGURE 4-47 .....   | 163 |
| FIGURE 4-50: DITHER EXAMPLES FOR THE $11.55 \mu\text{M}/\text{REV}$ FEED RATE. MACHINE VIBRATION IS INCLUDED ( $11$<br>$\text{NM AMPLITUDE AT } 63.6 \text{ Hz}$ ) .....   | 164 |
| FIGURE 4-51: Y-AXIS INTERCEPTS ( $B$ ) VS DITHER AMPLITUDE WITH MACHINE VIBRATION PRESENT. LOWER<br>VALUES OF $B$ INDICATE LESS SURFACE AGREEMENT. SAME MODELED CUTTING CONDITIONS ARE SHOWN<br>BELOW IN FIGURE 4-51.....  | 166 |
| <b>FIGURE 4-52:</b> RMS SURFACE FINISH VS DITHER AMPLITUDE FOR THREE CROSS FEED RATES ( $\mu\text{M}/\text{REV}$ ) WITH<br>MACHINE VIBRATION PRESENT. SAME MODELED CUTTING CONDITIONS USED ABOVE IN FIGURE 4-50.<br>.....  | 166 |
| FIGURE 4-53: SCATTER PATTERN MEASUREMENT SETUP. DASHED LINE SHOWS BEAM PATH. THE MIRRORED<br>GLASS REFERENCE IS LYING BESIDE THE OPTICAL SETUP. THE FINAL FOLD MIRROR, PINHOLE<br>APERTURES AND THE DIAMOND TURNED SAMPLE ARE MOUNTED ON THE OPTICAL RAIL.....   | 169 |
| FIGURE 4-54: ALTERNATE VIEW OF PAPER PINHOLE APERTURES. FROM FOREGROUND TO BACKGROUND:<br>FINAL FOLD MIRROR, FIRST APERTURE AND FINAL APERTURE. THE LARGE DOT ON THE FIRST APERTURE<br>REPRESENTS A BEAM DIAMETER OF ABOUT $4 \text{ MM}$ . .....  | 170 |
| FIGURE 4-55: SCATTER PATTERNS FOR MIRRORED GLASS AND $7$ FEED RATES DIAMOND TURNED IN<br>ELECTROPLATED COPPER. IN FIGURE 4-54B, THE DETECTOR WIDTH AND POSITION ALLOWED ROOM<br>FOR ONE MORE MODE TO THE LEFT OF CENTER. IN FIGURE 4-54F, THE REFLECTED BEAM IS OFF CENTER<br>TO OBSERVE THE FIRST MODE THAT WAS OUTSIDE THE DETECTOR WHEN CENTERED..... | 173 |

## LIST OF TABLES

|  |     |
|--|-----|
| TABLE 2-1: VICKERS HARDNESS VALUES FOR ROUGH MACHINED TELESCOPE COMPONENTS.....  | 13  |
| TABLE 3-1: RESULTS OF 6061 T-6 ALUMINUM MACHINING TEST TO PRODUCE FLAT SPECIMENS. *FOR TESTS<br>15 & 16, THE AUTOMATIC MASK WAS SET TO 5% ID AND STILL USED 95% OD.....  | 71  |
| TABLE 4-1: LAYOUT OF TESTS ON COPPER WORKPIECE .....   | 100 |
| TABLE 4-2: ANGLES OF DIFFRACTION FOR FOUR DIFFRACTION ORDERS AND FOUR WAVELENGTHS OVER<br>VISIBLE (WHITE LIGHT) SPECTRUM. INCIDENT BEAM IS PARALLEL WITH THE SURFACE NORMAL ( $\theta_i =$<br>$0^\circ$ ) AND THE SURFACE SPATIAL FREQUENCY IS 0.2 WAVES/ $\mu\text{M}$ (OR 5 $\mu\text{M}$ SINUSOID WAVELENGTH).... | 149 |
| TABLE 4-3: HILBERT TRANSFORMS []. .....  | 162 |
| TABLE 4-4: EXPECTED MODES IN THE SCATTER IMAGES FOUND IN FIGURE .....  | 174 |

# 1 INTRODUCTION

## 1.1 BACKGROUND

Diamond turned optics have been widely utilized in infrared and near-infrared imaging systems. These systems were placed in military applications including missile defense systems [9, 30]. They are typically rotationally symmetric and fabricated from an aerospace material, such as 6061-T6 aluminum alloy and the surface is sometimes coated with an impurity-free homogeneous (from the diamond tool perspective) material to improve surface finish [9].

Future applications include three-mirror systems that utilize free-form optical surfaces with no axis of rotation. Surfaces with no axis of rotation are currently being fabricated with diamond turning machines [21]. The performance of systems designed with free-form optics is often diffraction limited [28] and, according to the Rayleigh criterion, this performance is maintained for up to a quarter-wave peak-to-valley deviation from the designed wavefront [31]. Before fabrication of these non-rotationally symmetric optical components is attempted, the ability to fabricate less complicated axisymmetric systems with the Rayleigh criterion as a reference must be explored. Challenges in fabrication of these systems are not limited to the optical surfaces themselves. Special attention must be paid to the fiducial alignment feature on both the mirror and metrology frames used to locate the mirrors relative to one another and to the imaging sensors.

## 1.2 PREVIOUS RESEARCH

Single-point diamond turning machines commercially available in the late 1980s and early 1990's (like the Rank Pneumo ASG 2500) are typically equipped with oil hydrostatic bearings, ball screw drives for axis actuation, air bearing spindles, and laser interferometers for position feedback [9]. These machines are reported to create surface finishes in 6061 aluminum of approximately 40 nm PV and 6-7 nm RMS [9]. This is useful for the wavelengths in the near infrared spectrum and larger because these wavelengths will scatter from diamond turned surfaces at large angles (incoherent scatter) [16]. Newer machines with brushless DC linear motors for axis actuation and high-speed spindles have been reported to produce smoother roughness on surfaces coated with a single-phase material such as pure aluminum plating (Alumaplate®). Surface Roughness approaching 1 nm RMS has been reported and these diamond turned surfaces are reportedly adequate for use in the visible light spectrum. [6]

More recent research [19] has further explored the use of diamond turned 6061-T6 aluminum surfaces in white light applications. The optical surfaces fabricated for the Ralph telescope, a Three Mirror Antistigmat with 6061-T6 optical surfaces and metrology frame, were diamond turned but typical diamond turning characteristics were largely absent [19]. Measurements of the optical surfaces showed little indication of a tool nose radius and the frequency analysis of the surface more resembled that of an isotropic surface than a grooved diamond turned surfaces. RMS roughnesses of the Ralph telescope mirrors were reported from 4.9 nm to 7.1 nm. The optical elements were

off-axis conics and turned on-axis using a specialized chucking apparatus with allowances for centrifugal distortions.

### 1.3 PREVIOUS RESEARCH AT THE PEC

An error budget of the ASG-2500 was performed upon its delivery to the PEC. Slide straightness and squareness were measured as well as the yaw characteristics of each axis [3,4,5,6]. The repeatable errors were quantified and an automatic error compensation routine was created [3,4,5]. It was incorporated into the custom designed and built machine controller. The effects of spindle growth due to heating and environmental factors were also explored [7]. Axes vibration has been examined and closed-loop control for spindle error motions was attempted [14].

Drescher and Arcona performed a great deal of research oriented towards the improvement of the diamond turning process through modeled and experimental measurement of tooling forces and surface finish [12,13]. Many experiments were conducted using various materials and cutting conditions. The effects of tool wear on cutting forces and second order surface roughness effects were studied and described. Minimum chip thickness was examined and chip segmentation formulas were derived.

## 1.4 PROBLEM STATEMENT

To establish an understanding of optical system fabrication, a two-mirror Ritchey-Chrétien telescope was fabricated. Fabrication of this rotationally symmetric design was intended to establish a baseline capability for the diamond turning machine. Challenges include alignment of fiducial features of each element to the optical surface, optical surface finish quality, optical surface figure quality and alignment of fiducial features in the metrology frame. Also, fiducial feature shape and size are of interest because of interactions between the metrology frame and the optical elements.

A set of experiments was devised to characterize the form error capability of the diamond turning machine. Optical flats present the simplest geometry for a t-lathe to produce because one slide simply holds a position while the other slide moves the tool at a constant velocity. The goal figure error of an optical flat was  $\lambda/4$  peak-to-valley. Proper parameters for the automatic figure error correction scheme were desired such that it could be reactivated. Proof of machine repeatability at several axis locations was desired. A test was designed to fabricate a sphere such that the figure error of a workpiece when both axes were moving in concert could be measured. The goal for the sphere was also  $\lambda/4$  peak-to-valley figure error with a spherical radius error of  $\pm 3 \mu\text{m}$ .

After inspection of the Two-Mirror, it was desired that surface roughness be studied. A model was developed to describe surface finish based on theoretical tool cusps and how they are affected by machine vibration. In efforts to improve the surface finish of a

diamond turned surface, the model was expanded to incorporate tool dithering such that diffraction from a diamond turned surface could be modeled.

## 2 FABRICATION OF TWO MIRROR TELESCOPE

### 2.1 INTRODUCTION

Diamond turning is a standard technique for creating rotationally symmetric reflective optical surfaces. The workpiece is mounted on a rotating spindle and the diamond tool is moved along a path in space that is described by the cross-section of the surface to be created. The rotating spindle of the Diamond Turning Machine (DTM) turns the tool path into a three dimensional surface. The rotationally symmetric Ritchey-Chrétien telescope diamond turned here consists of a concave hyperbolic primary mirror, a convex hyperbolic secondary and a thin-wall tube to align the optics. A Ritchey-Chrétien (also called aplanatic Cassegrain) telescope has advantages over other classic axisymmetric two-mirror systems because two hyperboloid mirrors can simultaneously correct for coma and spherical aberration over the full field. However, as with all axisymmetric two-mirror systems, astigmatic aberration of this system increases with field angle. The rough machined components (pre-diamond turning) are seen in Figure 2-1. In addition to the two optical elements and the tube, the mounting plate to attach an SLR camera and the mounting brackets to attach a tripod are shown.

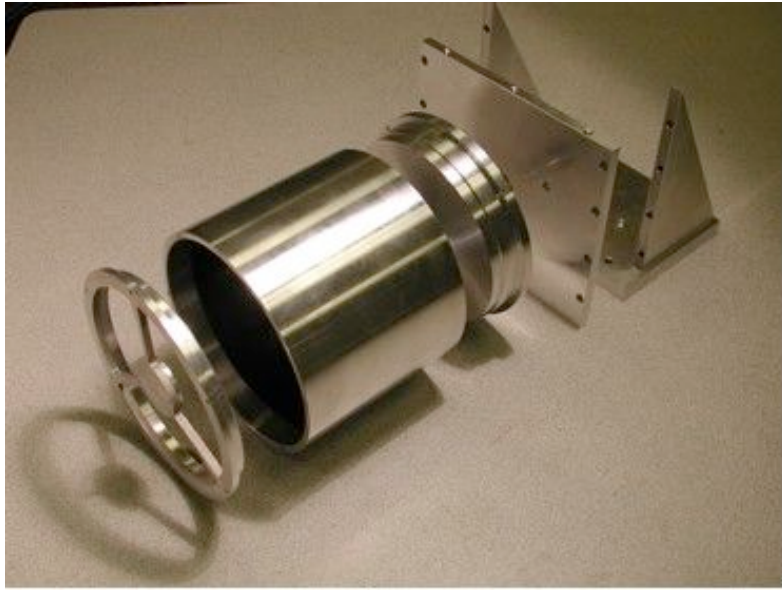


**Figure 2-1:** Rough machined components of the two-mirror telescope.

Figure 2-2 shows the optical path of the final telescope design and gives the specifications for the hyperbolic mirrors as described by Wanna [25]. The design requirements for the Ritchey-Chrétien called for a primary with  $f/\text{number} = f/1$  for high light-gathering ability ( $f/\text{number} = \text{aperture diameter}/\text{focal length}$ ), a 150 mm primary mirror aperture, a 15 mm detector height,  $1^\circ$  total field angle ( $\pm 0.5^\circ$ ) and 20% secondary mirror obscuration (distance from the primary focal point as percentage of primary focal length). For a concave mirror reflecting a collimated wavefront (infinite conjugate) the radius of curvature is twice the focal length; so for a  $f/1$  primary with 150 mm aperture the radius of curvature is 300 mm. The remaining parameters in Figure 2-2, in addition to the primary-secondary spacing of 113.625 mm and the secondary-image spacing of 208.519 mm, were optimized with CODE V by Optical Research Associates (ORA) as discussed by Wanna [25].

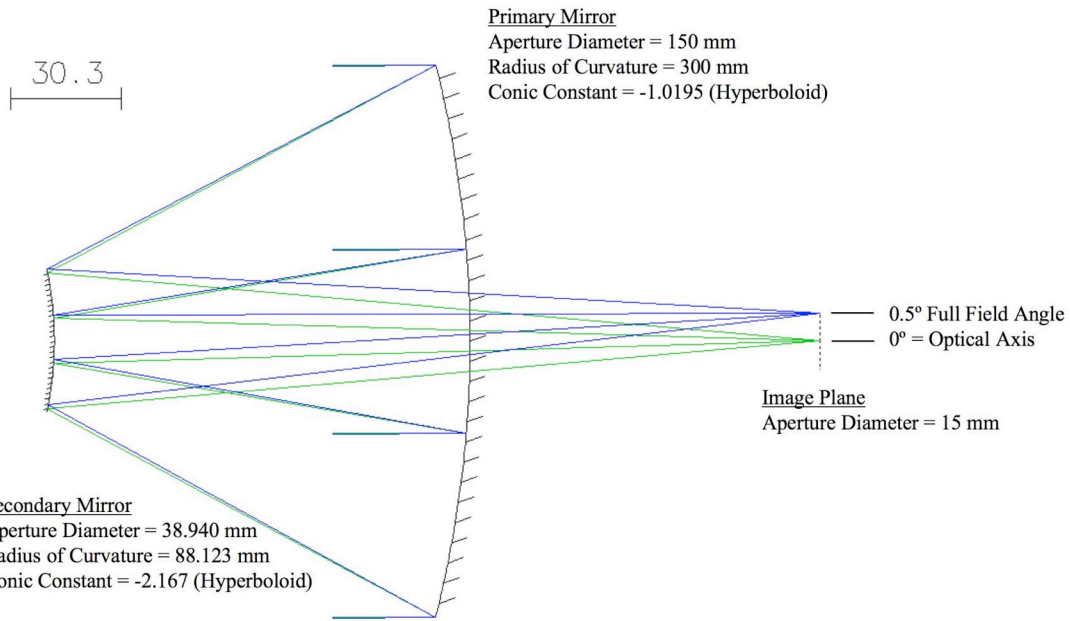


**Figure 2-2:** The optical path of the Richey-Chrétien telescope with optical elements and specifications. Incident light from the object (infinite conjugates) enters from the left and the image is formed on the right. Path generated with OSLO-EDU® from Lambda Research Corporation.

To create the optical surfaces, the tool moves through the prescribed hyperbolic path (from the outer radius to spindle centerline) with some compensation based on the circular edge shape of a diamond tool. The geometry (straightness and squareness) and control system of the machine slides determine the optical shape form error. The circular tool radius, tool edge quality, speed at which the tool is fed across the part, machine vibration and workpiece material determine the surface finish.

Fiducial surfaces are used to locate the two mirrors with respect to each other as prescribed by the optical design specifications. In this two-mirror system, a step on OD of the primary mirror locates one end of the tube while a step on the OD of the secondary support structure locates the other. The distances between the optical apexes and fiducial steps, combined with the length of the tube, set the mirror spacing. High resolution (2.5 nm) length measuring laser interferometers mounted on the DTM slides were used to control these distances during machining. Figure 2-3 shows a cross section of the components with heavy lines to indicate surfaces that were diamond turned. The assembled system can be seen in Figure 2-4.

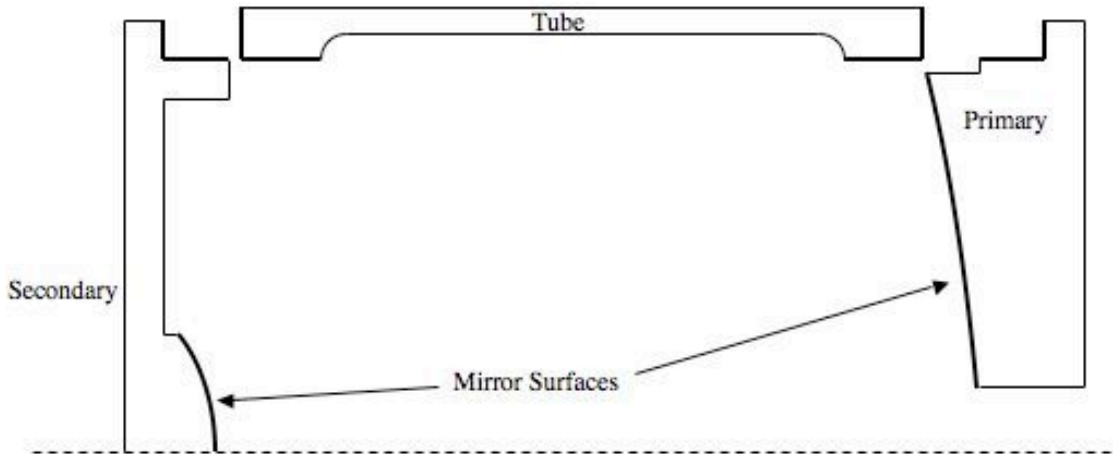


**Figure 2-3:** Cross section of telescope components with dark lines indicating surfaces that were diamond turned. Dashed line shows the common axis of symmetry/rotation.

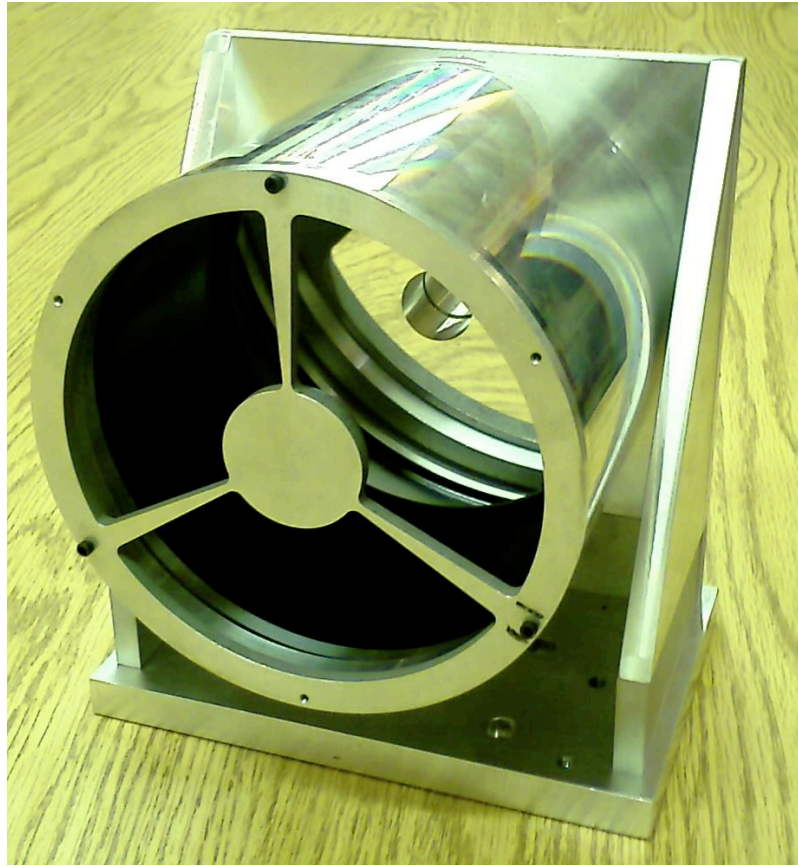


**Figure 2-4:** Final assembled optical system.

## 2.2 MATERIAL PREPARATION

### 2.2.1 *Rough Machining*

The telescope components shown in Figure 2-1 were rough machined with allowances for diamond turning of the optical and fiducial surfaces. The drawings of the rough machined components are found in Appendix C. All surfaces diamond turned had at least 150  $\mu\text{m}$  of extra material that was removed during final machining. The optical surfaces were rough machined to their spherical base radii. The locating steps on the

primary and secondary mirrors each have a tapered OD to align their centerline with the tube centerline when assembled. Rough machining of the step was specified at 90° so it had the extra 150  $\mu\text{m}$  plus the material removed to create the taper. The interior of the tube was anodized black with a matte finish to minimize internal reflections.

### *2.2.2 Heat Treatment*

To relieve residual stresses introduced during the rough machining process, the components were heat-treated. The procedure was as follows:

1. Cool the parts in a -100 °F environment at a natural rate for one hour.
2. Warm to room temperature in a still, ambient atmosphere.
3. Heat in a 300 °F environment at a natural rate for 2 hours.
4. Cool to room temperature in a still, ambient atmosphere.
5. Repeated steps 1-4 once.

### *2.2.3 Material Hardness*

The hardness of the system was measured following the stress reduction heat-treatment process. A Vickers indenter (pyramid shaped diamond with 136° included angle between the faces) was used for the experiments. Vickers Hardness Number (VHN) is a function of the load,  $P$  (kg), and the diagonal of the indentation,  $d$  (mm), as described in Equation 2-1.

$$VHN = \frac{1.72P}{d^2} \quad (2-1)$$

All tests were performed using a 1 Kg load, which is well suited to the hardness of machined aluminum because it provided small indentation marks (0.1 mm) that had crisp edges and corners. Increasing the load would cause a larger indentation and the original surface would extrude upward at the indentation edge.

Three pieces were tested: the heat-treated spacer and two reference specimens of 6061-T6. The diagonal lengths of the indentation were measured with two methods on the Zygo NewView white light interferometer and its software, MetroPro. The first method measured the diagonal lengths on an interferometric image with manually drawn trace lines across the indenture corners. MetroPro reported the trace length. The second method utilized the translating stage to align a cross-hair on the video monitor with each corner. MetroPro reported the X and Y position of the stage (crosshair) when aligned with a corner and the diagonal lengths were calculated using the Pythagorean theorem. This yielded two diagonal lengths for each method and the average of all four measurements was used to calculate the VHN. The resultant indentation lengths and calculated VHN are found in Table 2-1.

**Table 2-1:** Vickers Hardness Values for Rough Machined Telescope Components

| Sample      | Diagonal (mm) | Hardness (VHN)<br>Equation 2-1 (kg/mm <sup>2</sup> ) | Hardness (GPa) |
|-------------|---------------|--|----------------|
| Spacer      | 0.125         | 110  | 0.110          |
| Reference 1 | 0.139         | 90   | 0.90           |
| Reference 2 | 0.126         | 108  | 0.108          |

The published hardness of 6061-T6 Aluminum is 107 VHN or 95 Brinell hardness [18].

Both the spacer and Reference 2 are close to this value but Reference 1 is lower. None of the samples approach the hardness of un-tempered 6061: 30 Brinell hardness. Based on the results shown in Table 2-1, the heat treat process used to relieve residual stresses from rough machining had no effect on the hardness of the optical surfaces.

## 2.3 DTM SETUP

### 2.3.1 *DTM Geometry*

The fabrication of axisymmetric, Richey-Chrétien optical systems can be carried out using a t-based Diamond Turning Machine (DTM) shown in Figure 2-5. It is a Rank-Pneumo ASG-2500 and is further described in Section 2.5. The optical axis of each element is collinear, which means each can be machined using the face of the vacuum chuck as a reference surface and the spindle axis as the optical axis (the dashed line as shown in Figure 2-6). The process began with an operation to machine the back surface

of the primary mirror for vacuum chucking. The diamond cut back of the primary is then vacuumed to the spindle and the fiducial surface is machined during the same setup that cuts the optical surface. The distance between the fiducial surface and the apex of each optical surface is set during the single part chucking. After the primary is removed, the secondary is mounted and machined in the same manner with the same tool setup. The tube is then machined with a different tool layout because of its length and inner diameter fiducials. The tube length, face parallelism, and ID alignment set the relative position of the two optical elements. While the tube shown in Figure 2-6 is only one way to create the spacing between elements, it is a good illustration of the technique used to build rotationally symmetric systems because lengths and diameters are controlled with the DTM axes laser interferometers.

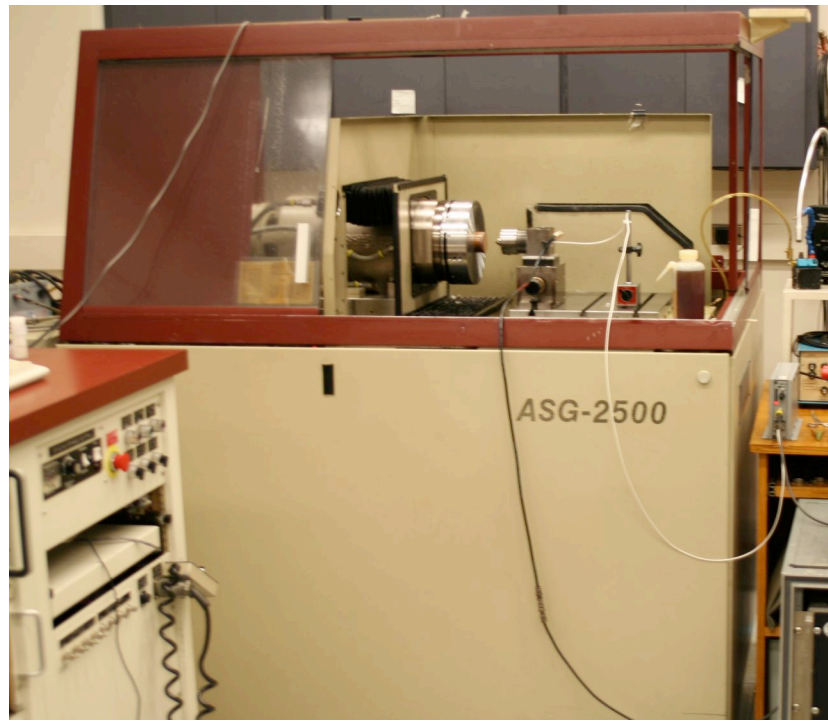


**Figure 2-5:** Rank-Pneumo ASG-2500 Diamond Turning Machine.

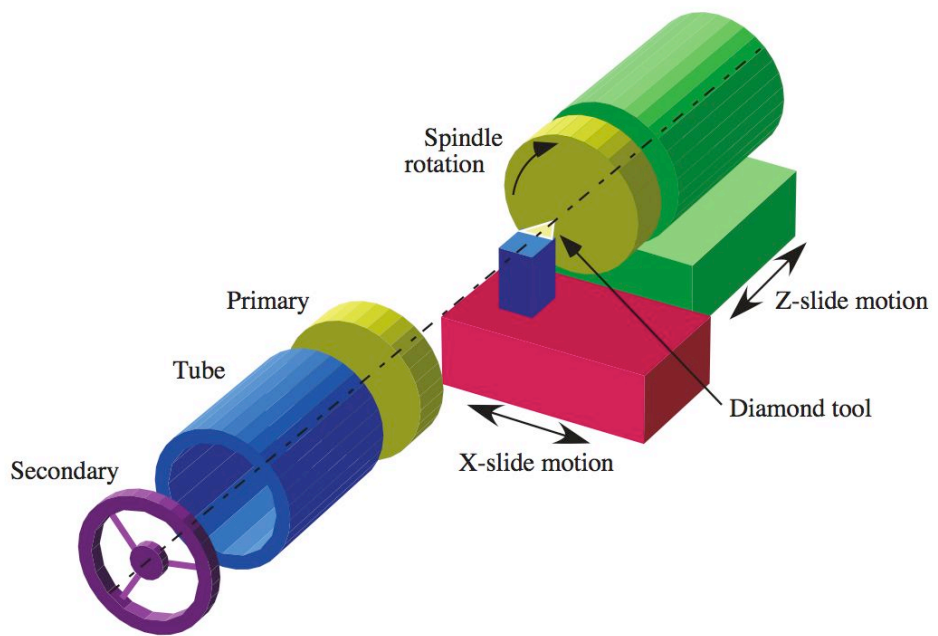


**Figure 2-6:** Fabrication of Richey-Chrétien telescope components on the ASG-2500 DTM with a dashed line to show the collinear optical, tube and spindle axes.

### 2.3.2 Tooling Setup

To create both the optical surface and the fiducials in one setup, two tools were used: a large nose radius (3.135 mm) for low optical surface roughness with shorter machining times and a small radius tool (0.1057 mm) for the sharp corners at the intersection of the fiducial surfaces on the primary and secondary. The DTM X-axis table provides room for multiple tool holders. Figure 2-7 shows the orientation and relative distance between the tools that was necessary to insure that neither contacted the workpiece while the other was in use. The tool holders and diamond tools were situated in this fashion before they were aligned to the DTM coordinate system. The small radius tool is angled towards the spindle centerline (angle set at  $\sim 30^\circ$  for adequate tool holder clearance) as seen in Figure 2-6 so that it can machine both the fiducial OD and step. The complete fiducial machining path is discussed later in Section 2.5.3 through 2.5.5. Since the back of the primary mirror is mounted to the spacer plate, overall thickness is a critical feature. It was then necessary to simultaneously know the position of the both tools with respect to the vacuum check face.

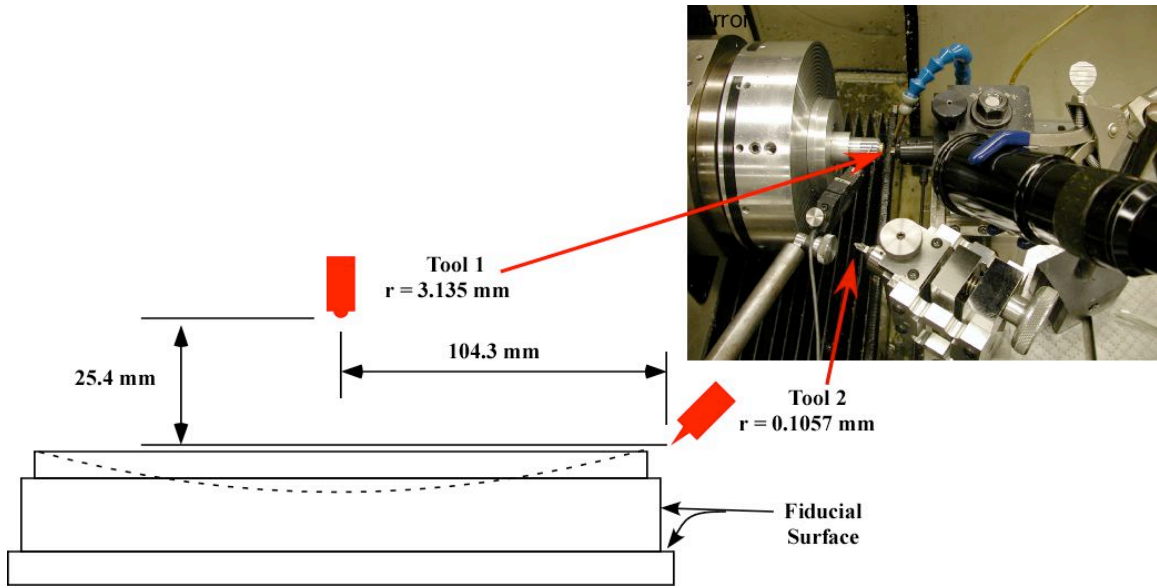


**Figure 2-7:** Tool layout on the DTM illustrating the relative location of the two tools and the 10x telescope (black cylinder on right of photo).

The X and Y position of each tool apex were located relative to the spindle centerline while the Z positions were located relative to the vacuum chuck face. Both tools were aligned to the spindle axis in the Y and X directions within  $1.5 \mu\text{m}$ . The absolute positions of each tool in the X direction were recorded so that they could easily be switched between during machining.

### 2.3.3 Tool Alignment to Spindle Centerline

Finding tool center is a multi-step process that takes considerable time and, if not preformed adequately, will significantly increase form error of the optical surface. The goal is to place the apex of the tool ( $X=Y=0$ ) at the centerline of the spindle. Figure 2-7

in Section 2.3.2 shows the larger tool being centered with respect to the spindle centerline. For fine centering errors in the horizontal direction (short or long in the X direction) an “Ogive Error” appears in the surface profile as measured with the laser interferometer [2]. Ogive error is named so because its characteristic shape often appears in arches of Gothic architecture and is seen in Figure 2-8. Gerchman discusses centering errors and calculated that the impact on form error is much greater for horizontal errors (X-direction) than vertical errors (Y=direction) [2]. It has been shown by others that the horizontal centering error can be modeled by adding an offset to the radial position in the standard aspheric sag formula [34].

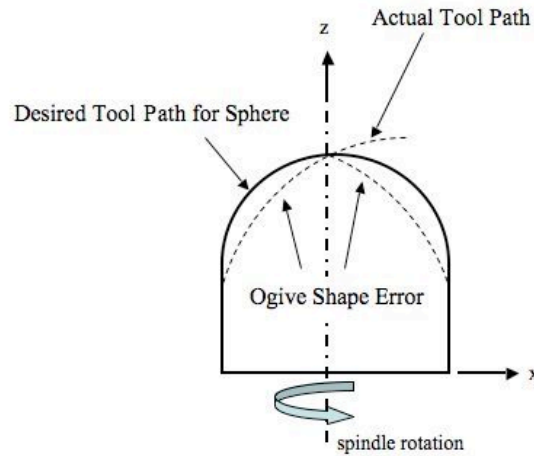


**Figure 2-8:** Ogive error caused by tool going past spindle center in X direction.

The technique used here was a multi-step method where several cuts in a centering plug were performed. The first step was to visually align the spindle during setup. The second

step (first cutting stage) set the rough center by finding the center error in both directions simultaneously because large errors are difficult to separate into X and Y components. The third stage of alignment sets the final tool center through error shapes seen in the centering plug and features seen at the tip. This stage generally requires several iterations and with each iteration, the X and Y direction errors are reduced independently of one another.

#### 2.3.3.1 Step 1: Visual Alignment at Setup

A centering plug in its holder is seen in Figure 2-9. An obvious feature may still be visible at the center of the plug through the 10X telescope if a previous centering exercise had a large height error (Y direction). If the small feature is visible (with the spindle running), the initial centering in the X direction can be accomplished by aligning the tool apex with the feature while looking through the telescope. If no feature was visible, initial X center was set by simply judging the apex of the tool with respect to the Z-axis (best done while standing behind the tool and looking towards the chuck face) and aligning it with the center of rotation. Both of these techniques yield alignment between spindle centerline in the X direction and the tool to within 500  $\mu\text{m}$ .

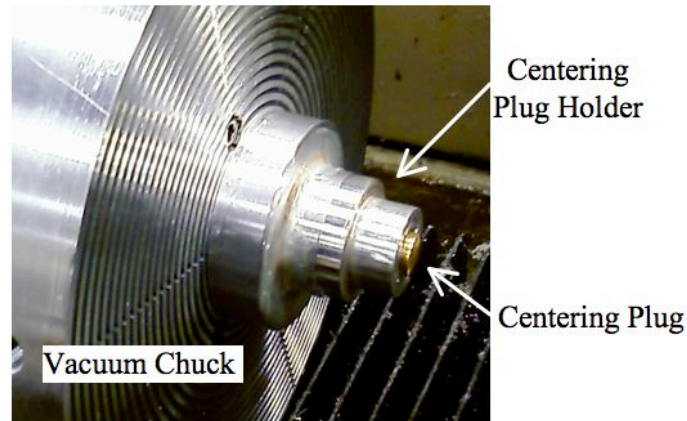


**Figure 2-9:** Centering plug mounted in holder, which is vacuumed to chuck.

To set the initial tool height (Y direction), a height gage was set to the nominal spindle height (6.007 in) and tool post was raised until the back edge of the diamond was seen to touch the gage tip; extreme care must be used here, as it is especially easy to damage the diamond. Figure 2-10 shows the height gage tip just above the diamond edge.

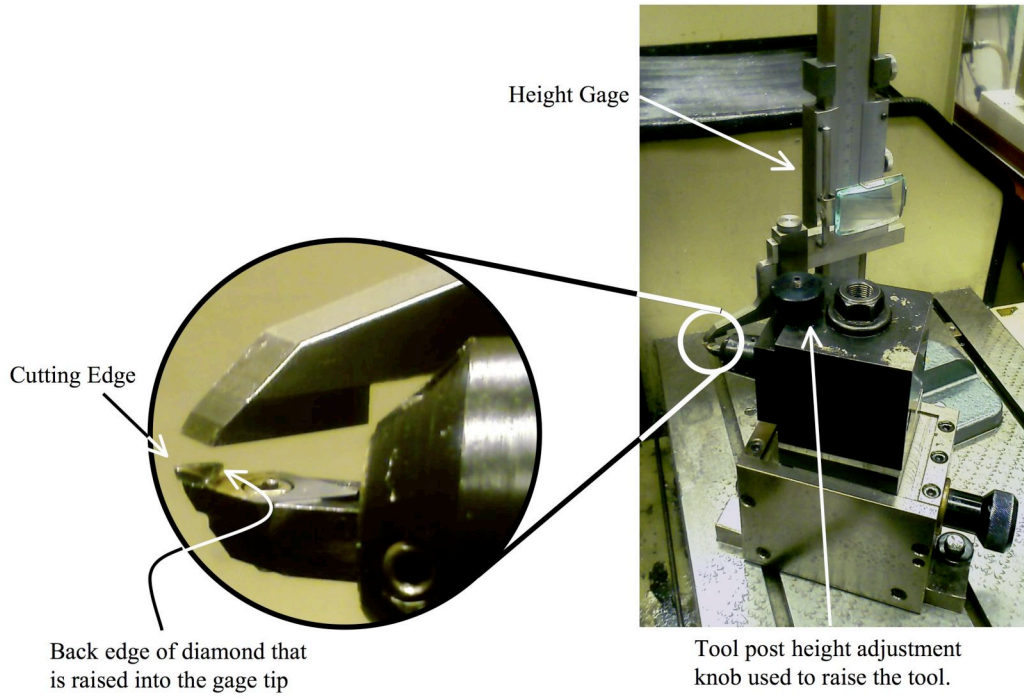


**Figure 2-10:** Height gage used to set the diamond tool height (Y-direction) at setup.

The diamond is raised into gage tip by turning the knob on the tool post.

### 2.3.3.2 Step 2: Rough Center

Rough centering was accomplished through use of the two-circles method. At larger alignment errors, the error in the horizontal (X-direction) and vertical (Y-direction) are not easily separated. Once initial alignment had been visually set, the tool was jogged some distance to the left of the spindle centerline and the X direction error was set to zero; this is called  $e_x$  in Figure 2-11. The distance may need to vary with tool radius but a distance often selected is 200  $\mu\text{m}$ . The tool is then slowly plunged into the part (1 mm/min) to make a single groove with radius  $r_i$ ; the plunge depth need not be greater

than  $2 \mu\text{m}$  so a few open-loop jog pulses at the slow speed, once the tool has contacted the part, are adequate. The tool is then jogged away from the part and moved in the X-direction some distance to create the second outer groove at radius  $r_o$ . The X-distance moved is recorded and seen in the Figure 2-11 as  $d_x$ . The part is removed from the DTM and the groove diameter is measured with the NewView using the crosshair and translating stage technique discussed in Section 2.2.3.

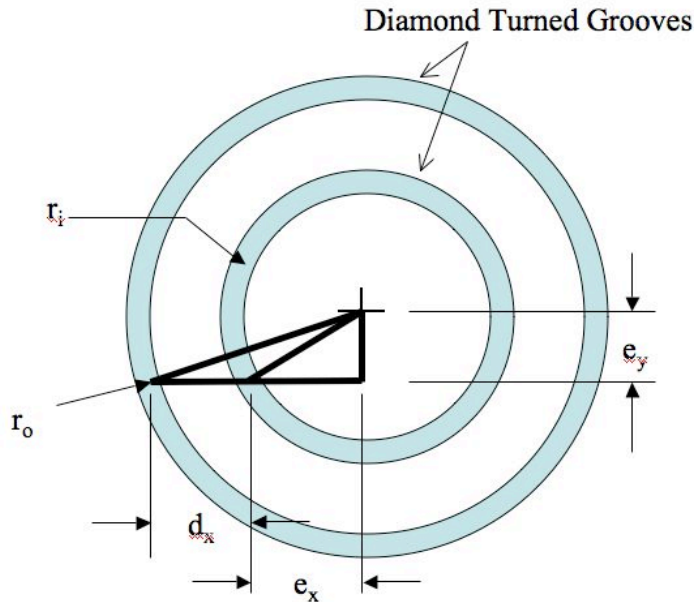


**Figure 2-11:** Two diamond turned grooves cut in the end of a centering plug.

Since the radii of the grooves ( $r_i$  and  $r_o$ ) and the distance moved in the X-direction ( $d_x$ ) are known, two equations with two unknowns can be written using the Pythagorean theorem for the triangles seen in Figure 2-11. The bases of the triangles are  $e_x$  and  $d_x + e_x$

with respective hypotenuses of  $r_i$  and  $r_o$  that share the common height,  $e_y$ . Solving for the two error terms yields the following system of equations:

$$\begin{aligned} e_x &= \sqrt{\frac{r_o^2 - d_x^2 - 2d_x}{2d_x}} \\ e_y &= \sqrt{r_i^2 - e_x^2} \end{aligned} \quad (2-2)$$

which gave the errors from the current tool location. The new offsets were programmed into the DTM and the fine centering steps were started.

### 2.3.3.3 Step 3: Fine Tool Center in the Vertical (Y) Direction

To set the fine position of the tool a small convex sphere was machined on a test part and measured to find its error shape. This technique requires a few iterations to set the tool center within 2  $\mu\text{m}$  of the spindle centerline. For centering errors in the vertical direction (low or high in the Y direction), a center defect will be created and the micro-height adjustor can be used to center the tool in the Y direction. The center defect was measured with the Zygo NewView white light interferometer. If the tool is lower than the spindle centerline, it simply fails to remove a small portion of material that is shaped like a cylinder as seen in Figure 2-12. If the tool is higher than the spindle centerline, a defect is created by the clearance face and has the shape of a cone as seen in Figure 2-13.

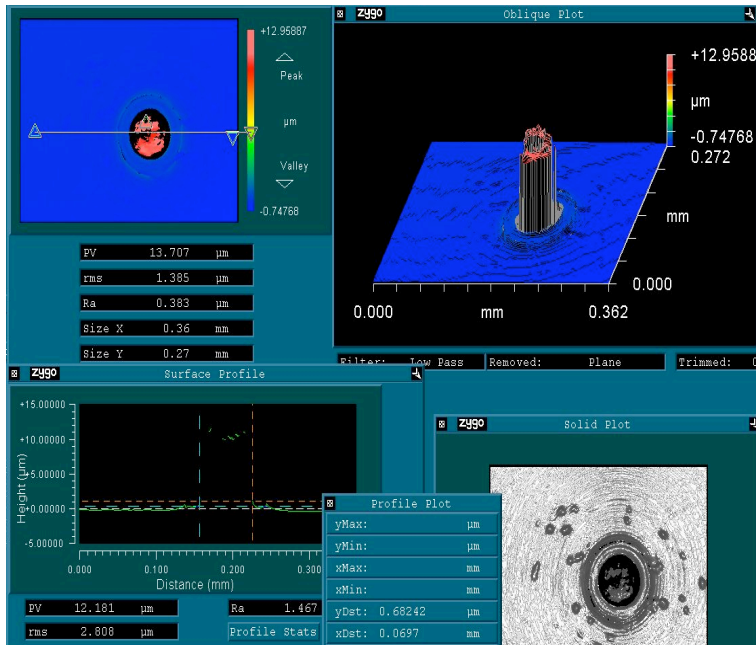


**Figure 2-12:** Screen capture of the New View measurement showing a centering error in the vertical direction (Y). The cylindrical shape indicates the tool was low of centerline.

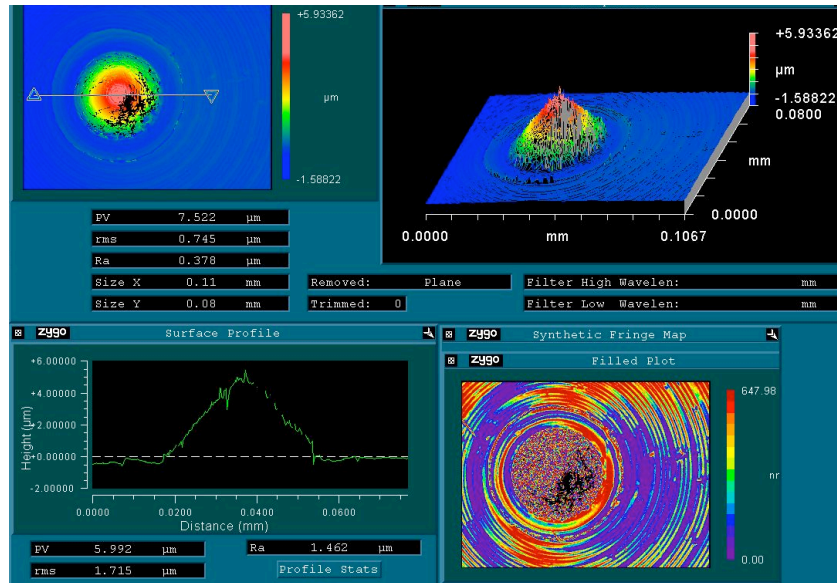


**Figure 2-13:** Screen capture of the New View measurement showing a centering error in the vertical direction (Y). The cone shape indicates the tool was high of centerline.

When working with small center features or center features without a clear shape, marks left on the workpiece from seams in the spindle air-bearing pads are useful to determine the direction and magnitude of the vertical error. When the spindle shaft passes a seam in air-bearing pad, it moves the chuck and workpiece into the diamond tool. This spindle motion is synchronous and is sometimes called ‘spindle star.’ Figure 2-14 shows the spindle star and has lines overdrawn to show the relationship between two marks that are  $180^\circ$  apart (there are 12 pads which make 12 marks so there are 6 opposing pairs). With counter clockwise spindle rotation the tool was moving from the left side towards the center. Following the line on the left in Figure 2-14 from the left to the center of rotation shows that the tool was lower than the center feature.

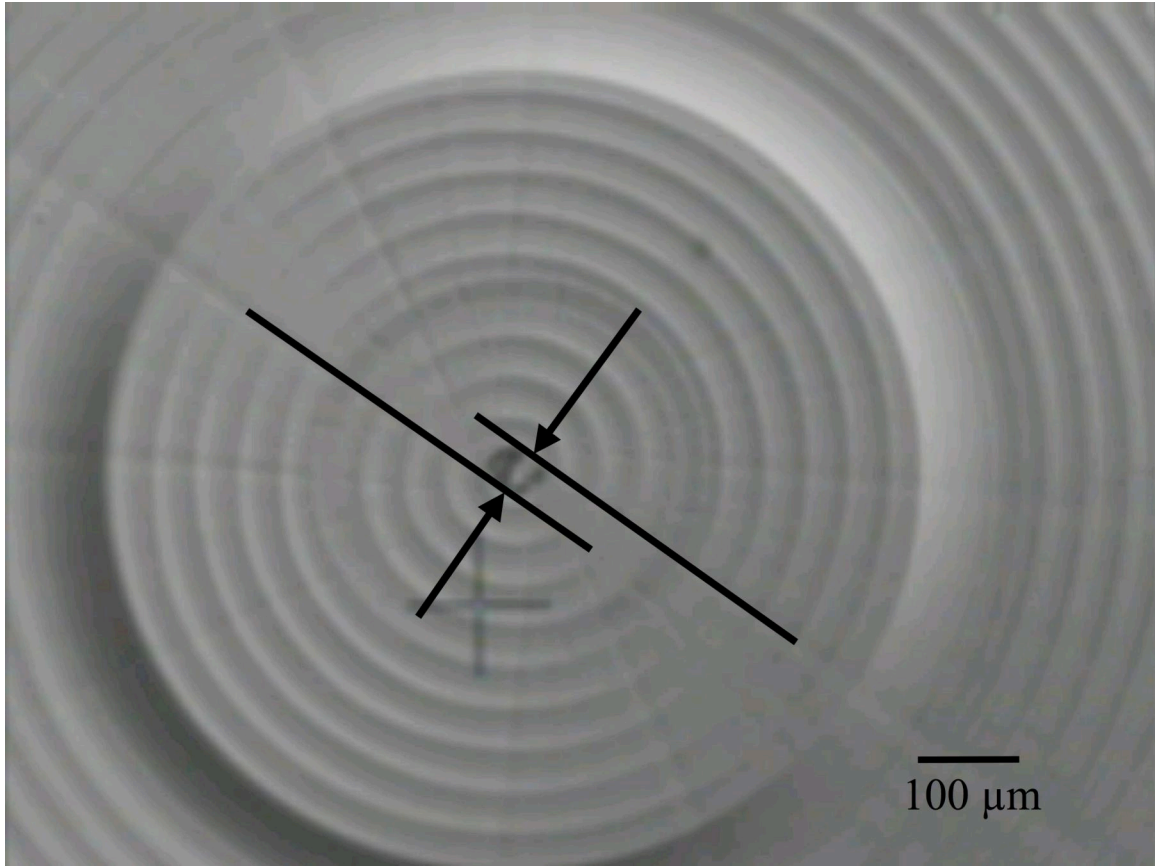


**Figure 2-14:** Spiral at center of workpiece where radial lines created by spindle air-bearing pads are visible. Dark lines highlight two opposing marks that, with counter clockwise spindle rotation, indicate tool was low.

#### 2.3.3.4 Step 3: Fine Tool Centering in the Horizontal (X) Direction

Figure 2-15 shows the form error for X-direction errors where the plug shapes are at the top (dashed line indicates tool path) and the error shapes with respect to a best-fit sphere (horizontal line) are at the bottom. If the tool is sweeping out a circular path from some

value of X corresponding to the aperture radius to the programmed point of X=0 and the tool goes beyond the spindle centerline, the interferogram will have the Ogive shape as seen in Figure 2-15a. If it stops short of the spindle centerline the interferogram will have a wavy dip in the center as seen in Figure 2-15b. The peak in the center of the error in Figure 2-15b is caused by the center feature remaining when the tool stops short and, if the error is small, is not always observed in the part measurement. For a concave sphere test part, the ogive error shapes are inverted about the best fit sphere line.

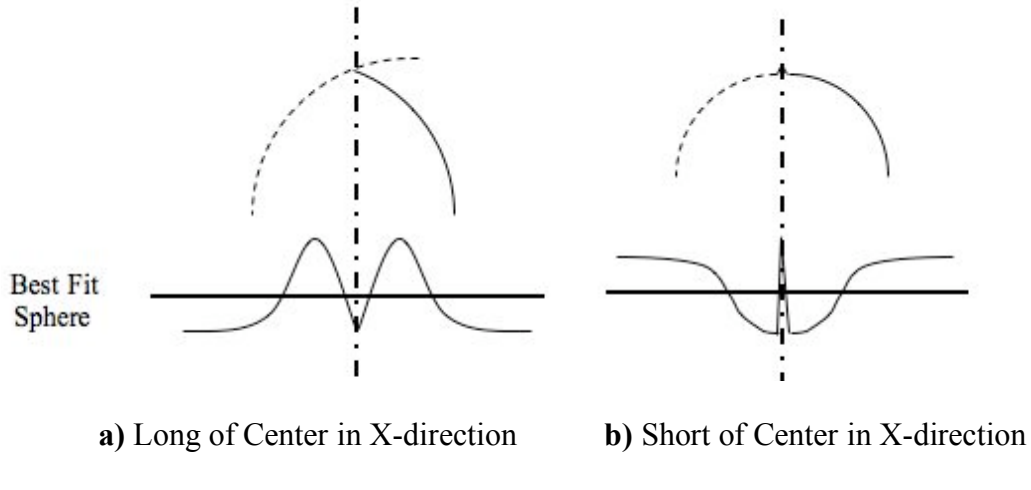


**Figure 2-15:** Cross Sectional Error Shapes for a Centering Plug Sphere in the Horizontal Direction (X).

Based on the measured form error, the X value is offset until a sphere with minimal form error magnitude (approximately 100 nm to 150 nm) is created. At that point, the tool location relative to the spindle centerline is known within 2  $\mu\text{m}$  as calculated by the Zygo GPI software. An example of a center plug measurement where the tool traveled beyond

the spindle centerline is seen in Figure 2-16 and the error shape can be matched to the one seen in Figure 2-15a.

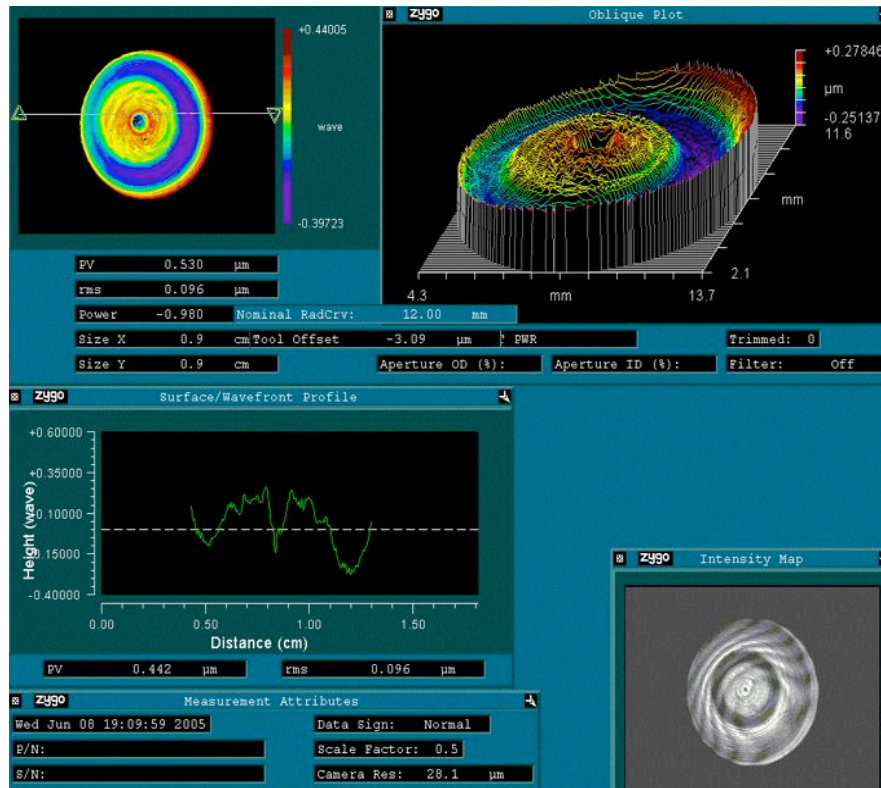


**Figure 2-16:** Screen shot of GPI output showing a centering error in the horizontal direction (X) where the tool was long of center. Trace shape seen in Figure 2-15a.

#### 2.3.4 Tool Z reference

After the tools were centered with respect to the spindle axis (X and Y), each apex was referenced to the face of the vacuum chuck to define a common Z reference. By setting the apex of the tool, instead of the radius center, as the point of reference where

X=Y=Z=0, the Z direction offset could be easily found by bringing the tool into contact with the vacuum chuck. The small tool was used to face the vacuum chuck to ensure that no raised material that would influence mirror fabrication. The large tool was “touched” to the chuck using a closed loop program with 100 nm step sizes. Because the tool radius was large, even a depth of cut of 100 nm produced a chip large enough to see with the 10x telescope seen in the bottom right of the photo in Figure 2-7. The Z-axis offsets of each tool were recorded after they were referenced to the spindle face so they could be switched between while performing various operations on the ASG-2500. As discussed later in Section 2.5.1, the chuck had a convex shape with a peak to valley error of about 700 nm due to squareness error between the slide axes. The large tool was touched to the chuck at an intermediate radius, so the error in offsets was about 350 nm.

### ***2.3.5 Surface Finish, Feed Rate and Spindle Speed***

Feed rate and spindle speed are selected based on the desired surface finish, machining time and error characteristics of the spindle. The theoretical peak-to-valley ( $PV$ ) surface finish is calculated from Equation 2-2 with a parabolic approximation of the tool shape using the feed rate ( $f$ =feed/rev) and the tool radius ( $R_t$ ).

$$PV = \frac{f^2}{8R_t} \quad (2-2)$$

Smaller feed rates and larger tool radii will improve the finish. However, there is a roughness minimum that is based on the asynchronous vibration of the spindle, the tool sharpness and the material to be machined. Asynchronous spindle vibration will change the cutting depth from one revolution to the next for any angular position across the face of the part thus increasing the surface roughness. The tool edge sharpness will affect the minimum chip thickness and can increase the roughness [12, 13]. Finally, the material structure (for example second phase particles in 6061 Al [10, 11]) will create imperfections that will degrade the surface finish. The sharpness of the tool can interact with the second phase particles in 6061-T6 and a less sharp tool can produce better surface finish than a sharp one [12].

For the proposed mirror surfaces, a spindle speed of 530 rpm was selected (minimum error motion as measured), feed rate of 2 mm/min for the primary, 1 mm/min for the secondary, and a tool nose radius of 3.135 mm. At these feed rates, each finish pass was approximately 40 minutes long, indicating the need for excellent temperature control because of the temperature sensitive of the laser interferometers in the ASG-2500 [5]. For these machining conditions the theoretical PV surface roughness from Equation 2-2 will be 0.57 nm for the primary and 0.19 nm for the secondary. The ASG-2500 has created surface finishes on the order of 2 nm in pure materials (plated copper and 1100 aluminum) but not in 6061- T6 [8]. The actual surface finish was on the order of 5 nm

RMS due to the issues discussed above which are further explored in the Chapter 4 of this thesis.

## 2.4 CONTROLLER PROGRAMMING

### 2.4.1 *Number of Points in the Programmed Path*

The hyperboloid surfaces of the primary and secondary mirrors are created with a programmed path that consists of a series of X, Z commands. As a result, the controller prescribes a series of straight lines that approximate the hyperbolic shape. If the acceptable deviation between the programmed straight lines and curved tool path is 1 nm and the reflective surface is approximated as a parabola, Equation 2-2 can be used to calculate the acceptable distance between points for the primary mirror. Equation 2-3 shows Equation 2-2 solved for  $f$ , where  $f = d_p$  is the distance between points along the straight line,  $PV$  is the peak-to-valley sag between the line and curve it represents, and  $R_t$  is the parabolic base radius. The cutting path length of the primary mirror is 62 mm, so 62 mm divided by 48.9  $\mu\text{m}/\text{point}$  yields 1266 X, Z points. Employing the same method for the secondary mirror yields 735 X, Z points.

$$d_p = \sqrt{(PV)^* 8 * R_t} = \sqrt{(1 \text{ nm})^* 8 * 300 \text{ mm}} = 48.9 \mu\text{m}/\text{point} \quad (2-3)$$

### 2.4.2 Tool Radius Compensation

The shape of the diamond tool must be considered when cutting non-flat surfaces. For a circular tool cross-section, the theoretical tool center traces out a path that is offset from the cutting edge by the radius of the tool as seen in Figure 2-17. The direction of this offset is perpendicular to the slope of the surface at the point of contact. The tool radius was measured using the translating stage and video output of the NewView to position a crosshair on the diamond edge. The MetroPro software gives coordinates of the stage (taken as the coordinates of the crosshair) and, with several points recorded along the cutting window, the data are input to a curve fitting function in MATLAB to find the best fit radius.

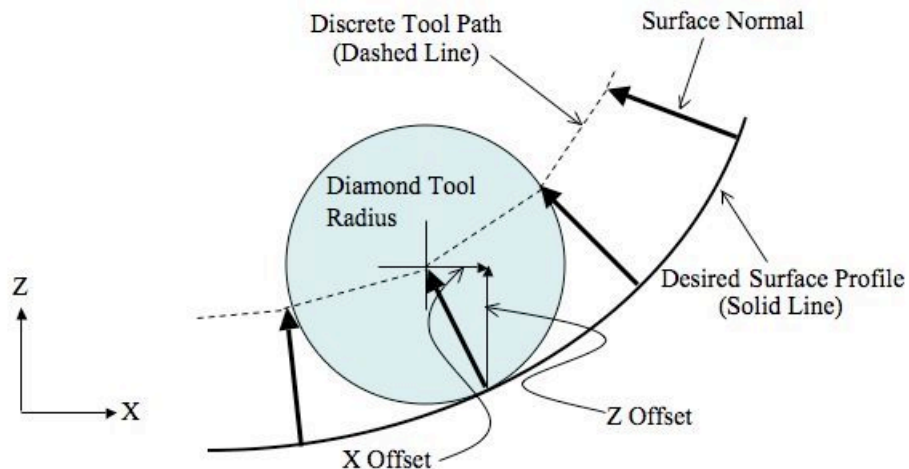


**Figure 2-17:** Illustration of surface normal vectors and tool offset to form discrete tool path. Desired surface is a continuous function and the normal vector length is equal to the tool radius.

The programmed tool path can be corrected for the radius of the tool by finding the normal vector at each point in the path and offsetting the axes locations by the tool radius along this vector (in the correct direction). Figure 2-17 shows a hypothetical surface shape with evenly spaced normal vectors that are equal in length to the radius of the diamond tool in that figure. The dashed line represents the discrete tool command, which is a series of straight lines between successive points as discussed in the previous section. The discrete tool path length between the two right most normals is smaller than the length between the left most normals because the curvature between the right most normals is greater. Normal vectors can be found analytically for geometrical surfaces or estimated numerically for a closely spaced path of discrete data points. The offset for each discrete point is simply the product of the tool radius with the sine (for X) and the cosine (for Z) of the normal angle. Figure 2-18 shows the desired primary surface (solid line), the tool radius compensated machining path (dashed line), and has three circles representing the tool nose radius.

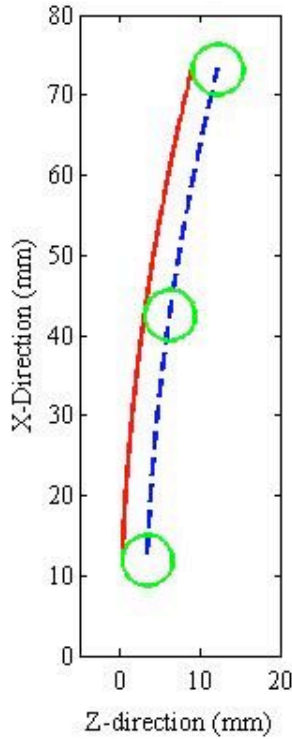


**Figure 2-18:** Cross-section of desired primary optical surface (solid line) and tool radius compensated machining path (dashed line) with circles representing the tool radius. To scale.

The sequence of corrected points defines the commanded path of the tool center. The result of this process is illustrated in Figure 2-19 where the upper curve in each plot labeled “Tool Path” (i.e., the tool center) is at a constant offset (the tool radius) from the hyperbolic surface swept out by the tool edge during machining. The upper curves are the recorded tool paths as measured by the laser interferometer and are discussed in the next section. The same data *uncompensated* for tool radius is shown as dots and the desired hyperbola is the solid line that passes through the circles.

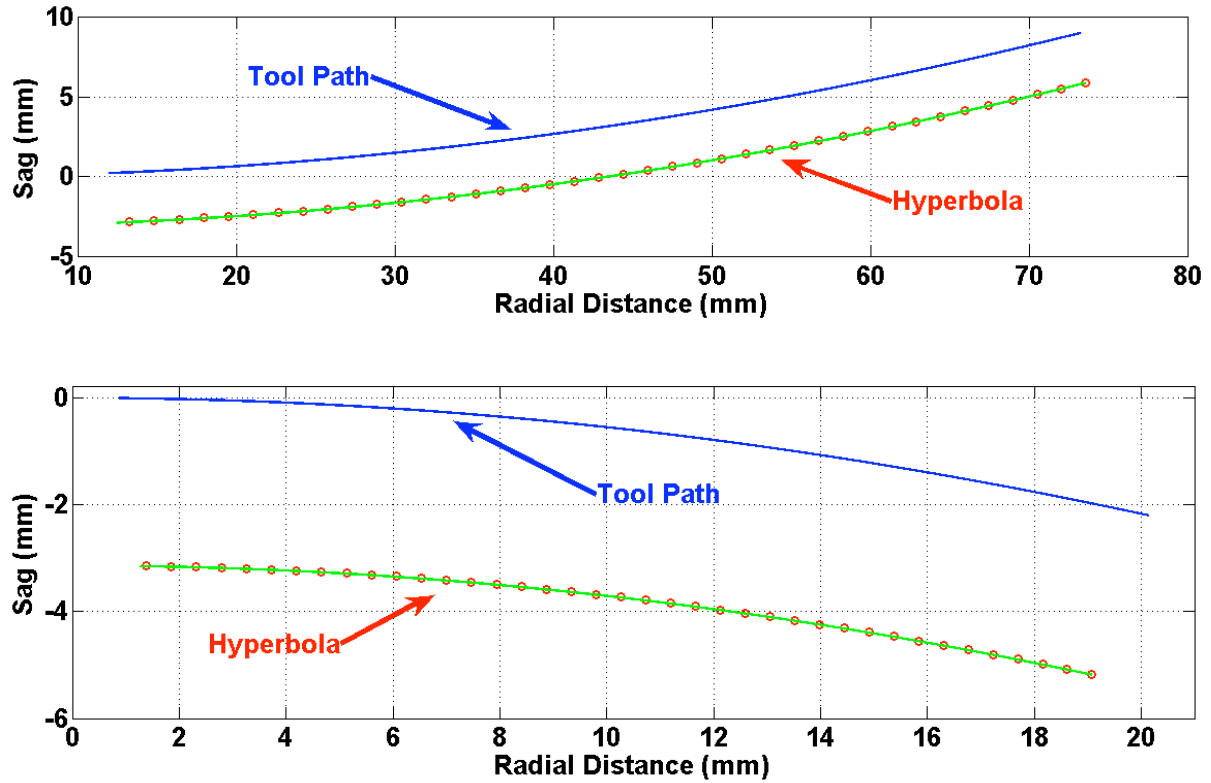


**Figure 2-19:** Primary (upper) and secondary (lower) mirror motion plots drawn by K. Garrard. The circles ( $\circ$ ) identify the uncompensated tool path while lines passing through the circles labeled *Hyperbola* are the surface as specified by the optical design. Lines labeled *Tool Path* are the tool radius compensated path.

#### 2.4.3 Axes Following Error

The programmed tool path for the hyperbolic mirrors with correction for the tool radius was input to the controller. To check for error in this path, the trajectory following capability of the ASG 2500 DTM was evaluated while running the primary and secondary hyperbolic mirror finish pass motion programs. The controller recorded data

every 32<sup>nd</sup> iteration of its 500 Hz servo loop, for a 15.625 Hz sample rate (64 milliseconds/sample). The finish pass cross-feed rates for the secondary and primary mirrors were 1 and 2 mm/min, respectively. Approximately 30,000 data points were collected for the primary mirror motion program and 22,000 data points for the secondary mirror. Each sample contains the commanded positions of the X and Z axes, their actual positions as measured by the laser interferometer, and the servo loop voltage commands sent to the pulse width modulated motor amplifiers. This is the data seen in Figure 2-19 and Figure 2-20. Each axis of the DTM vibrates at its natural frequency (Z axis with spindle is 64 Hz and X axis is 89 Hz) with amplitude of about 30 nm [12, 13, 14] but this vibration will appear as aliased high frequency information in the sampled data because the Nyquist frequency of the sampled data is 7.8126 Hz [29]. In Figure 2-20 this aliased high frequency vibration was removed with a 100 point running average filter.

The error in tool trajectory caused by the control system for each mirror is a combination of the X and Z command following errors. To evaluate this error, X and Z axis positions were compared with the ideal trajectory in Figure 2-19. As discussed previously, the commanded tool path and the resulting motion of the axes were compensated for tool radius. The direction of the offset is determined by whether the shape is a concave or convex. Therefore, to compare the actual motion to the desired path, the recorded data was uncompensated for tool radius by applying a radius compensation algorithm in a direction normal to the tool path and toward the ideal surface. Then, for each X position in the data set, a sag value on the desired hyperbola was generated and the sag error was calculated.

Figure 2-20 shows the difference between the dots and the solid lines that pass through them from the two plots in Figure 2-19. This difference is the sag error as recorded by the ASG-2500 control system laser interferometer feedback. For the primary mirror the PV motion path error is 16.75 nm (2.4 nm RMS) and for the secondary mirror the error is 12 nm PV (2 nm RMS). The pitch of the lead screws is 5 mm and neither plot exhibits that spatial frequency because the laser interferometers measure in the direction of axis motion as discussed later in Section 3.2.2. At the relatively slow feed rate used to machine both mirrors, the dead band from the controller DACs, ball screw friction, and motor friction were most likely responsible for the error magnitude [32]. The actual tool motion is close enough to the programmed tool path to create no figure errors.

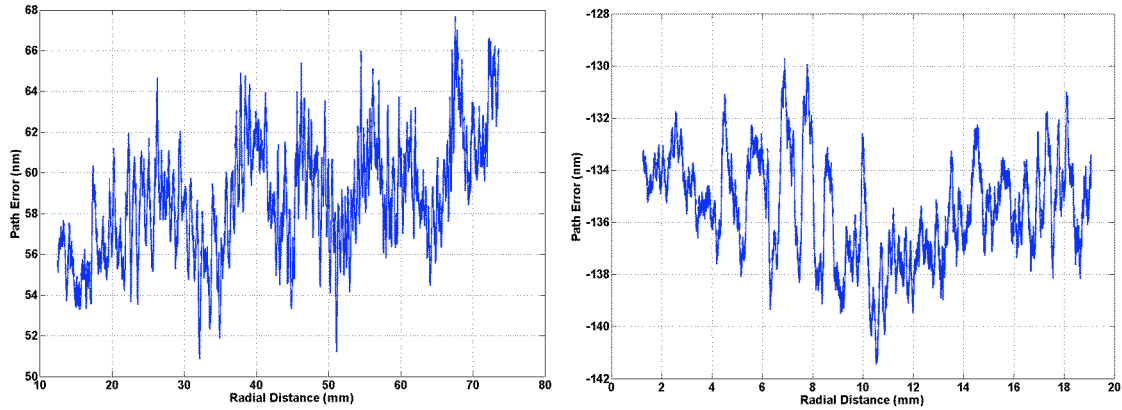


**Figure 2-20:** Primary (left) and Secondary (right) mirror motion path error filtered with 100 point moving average by K Garrard. This shows the difference between commanded path and the actual path as measured by the laser interferometer feedback of the ASG-2500 control system.

## 2.5 DIAMOND TURNING OPERATIONS

The diamond turning machine used for machining the optical and fiducial surfaces is a Rank-Pneumo ASG-2500 T-lathe and is seen in Figure 2-5. It is equipped with hydrostatic oil bearing slide-ways, laser interferometer position feedback for slide-way position (2.5 nm resolution), ball screw slide drives, air bearing spindle with angular encoder (20,000 points/rev) and a vacuum chuck to hold parts to the spindle. A controller developed at the PEC is used to command the position of the axes. It uses a Motorola 68020 processor board with Burr-Brown input/output boards for motion control. The host PC for the 68020 was an early 1990's PC-AT 80286.

The fabrication capability of a modern DTM allows the optical elements to be machined with a form tolerance of  $\lambda/4$  (150 nm) on the optical and fiducial surfaces while diameters and lengths can be fabricated to a tolerance of  $\pm 2 \mu\text{m}$ . For the R-C telescope discussed in Section 2.1, machining errors of this magnitude double the wave front error ( $0.15 \lambda$  to  $0.30 \lambda$ ) of the best performing field angle ( $0.35^\circ$ ) and increase the other field angle ( $0^\circ$  and  $0.5^\circ$ ) errors by about 10% ( $0.7 \lambda$  to  $0.8 \lambda$ ) [28].

The remainder of this section describes the steps in the fabrication of the mirror and fiducial surfaces.

### **2.5.1 Step 1: Vacuum Chuck**

#### **2.5.1.1 Flatness**

The face of the vacuum chuck was used in the machining process as the reference surface for position of the optical and fiducial surfaces. It was faced off prior to machining and was assumed to be flat. Unfortunately, this was not true. Figure 2-21 shows the flatness of the chuck around the periphery measured with an electronic LVDT indicator by the PEC staff after the optic was fabricated. Comparing the slope of the flat and tapered faces, the relative angle is about 2 arc-seconds. This is a result of the spindle axis (mounted to but not necessarily perfectly aligned with the Z-Axis) to X-Axis squareness error and not activating the yaw and squareness correction built into the machine tool controller as discussed in the next chapter. The surface of the chuck was cone shaped with a peak in the center and the taper had a magnitude of about 710 nm. This lack of flatness had an effect of the shape of the finished mirrors and suggestions for future operations are discussed in Section 2.5.7.

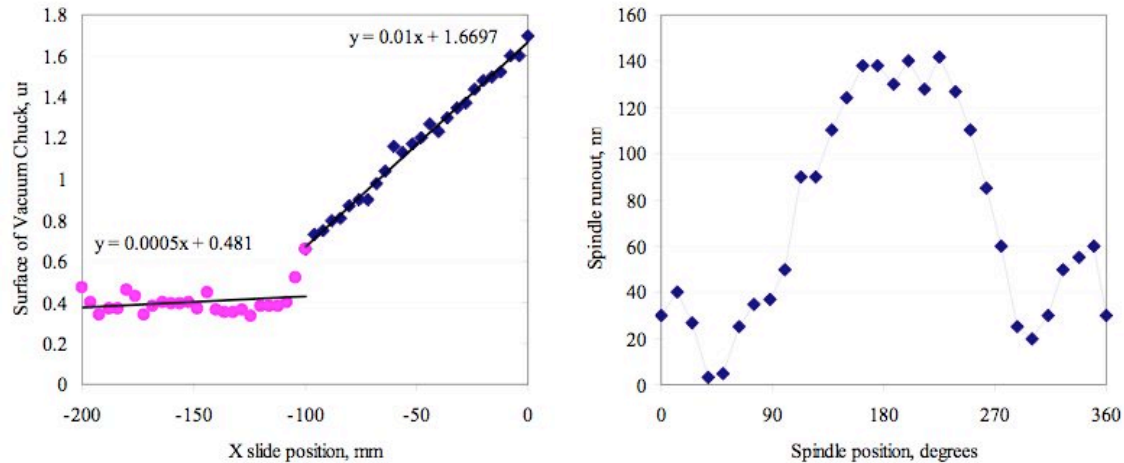


**Figure 2-21:** Vacuum chuck flatness (left) and runout (right) as measured for two mirror fabrication.

### 2.5.1.2 Axial Runout

The axial runout of the chuck was also measured with a LVDT indicator while the spindle rotated at low speed and is shown at the right in Figure 2-21. The indicator was 80 mm from the center of the spindle (spindle radius is 101.6 mm). The peak-to-valley runout is low (140 nm), which should produce an optical surface that has less than  $\lambda/4$  non-rotationally symmetric error. If this value is deemed too high, the chuck could be machined with the FTS or a workpiece aspect ratio could be designed to tolerate this runout as described in Section 2.5.7

### 2.5.2 Step 2: Primary Back

The back of the rough machined primary mirror was diamond turned to create a flat reference surface for attaching it to the vacuum chuck. The back of the primary is seen in Figure 2-22. A small flat ring was first cut into the outer rim of the optical surface (front) to create a chucking surface. When this component was vacuumed to the chuck, the support at the edge would cause it to take on a concave shape. If machined flat and removed from the chuck, it would elastically deflect into a convex shape because the aspect ratio was low of (thickness to diameter = 1:6) [28]. However, the tool path could be modified to counteract this effect. The shape of the back while the primary vacuumed to the chuck was measured ( $\sim 0.7 \mu\text{m}$  concave) with an LVDT indicator with involute tip. The back was measured off the chuck ( $1.3 \mu\text{m}$  convex) and then machined with a concave radius that had sag equal to  $2 \mu\text{m}$ . When the back was inspected after the first pass, an edge of the surface remained uncut which indicated the rough machined component was non-rotationally symmetric, so the operation was performed again with a larger depth of cut. The final shape of the primary found in Woodside's measurements [1] shows a convex shape with about  $0.6 \mu\text{m}$  of magnitude. The convex shape in the vacuum chuck described previously in Section 2.5.1 would indicate that the machine axes were not square for this operation and explain why the back of the primary had a convex shape after final machining. The measurements also showed a non-rotationally symmetric shape remained with a magnitude of  $0.6 \mu\text{m}$  when the convex shape is removed with the interferometer software. This, the need for two machining passes, and the small level of measured runout in the chuck indicate that the rough machined

workpiece contained non-rotationally symmetric distortion. Future suggestions to address this issues are discussed in Section 2.5.7.

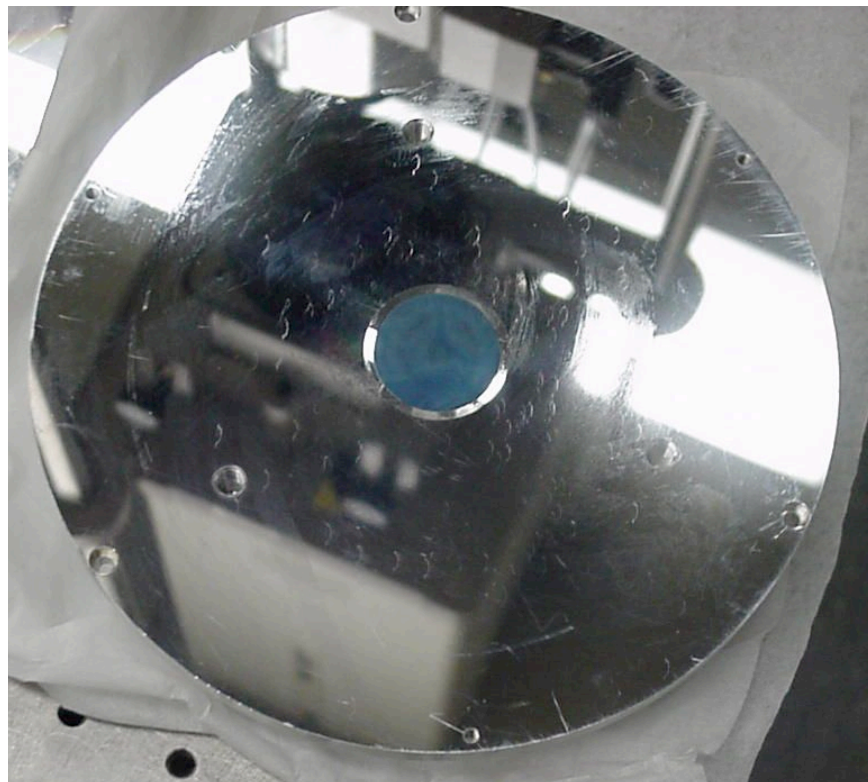


**Figure 2-22:** Diamond turned primary back. Center plug is rubber.

### 2.5.3 Step 3: Primary Mirror and Fiducial

The programmed path of X, Z commands is based on the mathematical description of the optical surface. The optical surface is a hyperbola with a  $k=-1.0195$ , a base radius of 300 mm, an OD of 150 mm and a 26 mm hole in the center. Because there is a hole in the center of the mirror, a rubber plug was used to create a seal for the vacuum chuck. The

optical surface was first rough machined to the desired hyperbola shape with the 0.1057 mm tool (used for the fiducials, not the optical surfaces) to preserve the edge sharpness of the 3.135 mm tool. When cutting 6061-T6 aluminum, second phase particulates cause high tool wear rates and can easily damage a sharp nose radius [8,12,13]. The finished optical surface was cut using the 3.135 mm tool and multiple passes were performed at increasing depth until the surface was completely machined. At this point, machining logs indicated that apex to chuck distance was 22.571 mm. The designed distance was 22.5 mm; however, tool wear concerns dictated the decision to cease machining at the larger thickness. Fiducial step height was adjusted accordingly so the relationship of the fiducial step to the apex was preserved at 15 mm and there was no impact on the distance from the primary apex to the secondary apex (measurements indicated that machining error between the fiducial and apex were 3  $\mu\text{m}$  [33]). Because the overall thickness of the primary was larger, the relationship between the system apex and the camera-mounting surface was affected. Adjusting the spacer washers between the primary and the spacer plate could compensate for this difference.

The cutting paths are seen in Figure 2-23. Unfortunately, the tool radius was input to the controller as 3.125 mm instead of the measured radius of 3.135. As a result, sag in the primary was reduced by 300 nm or the radius of the hyperbola was increased. This had minimal effect on the optical performance. It mostly increased the optical power (or speed) of the primary and is partly responsible for the difference between the location of the designed and measured focal point [1].

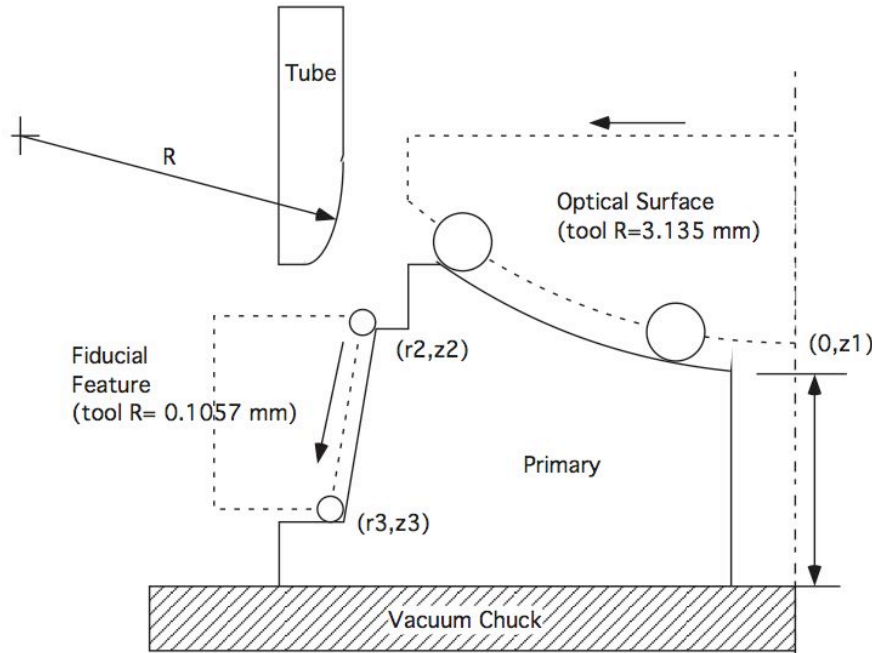


**Figure 2-23:** Primary optical and fiducial cutting paths.

The fiducial feature that transfers the primary optical shape to the secondary is a step on the OD that mates with the tube and is shown in Figure 2-23. Figure 2-24 shows the critical features of this fiducial: the taper angle ( $1^\circ$ ), the taper radius and the step height from the vacuum chuck. This feature was machined with the 0.1057 mm radius diamond tool, which was set to Z reference and spindle centerline as discussed in Section 2.3.3 – 2.3.4.

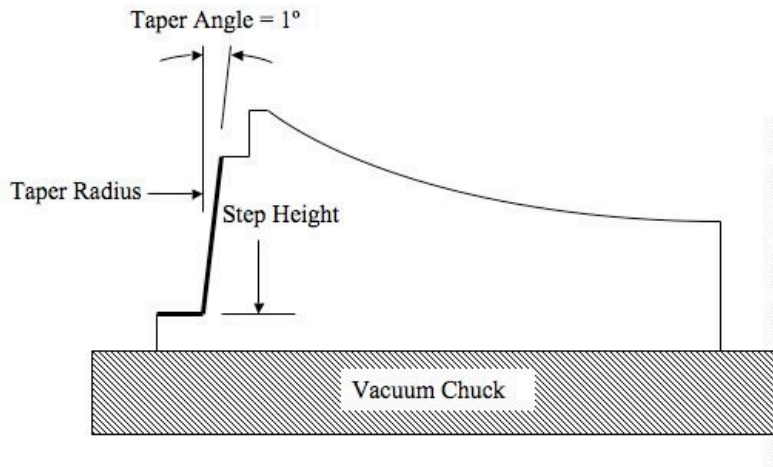


**Figure 2-24:** Cross-section of Primary showing critical fiducial features. Surfaces cut are drawn with bold lines.

Cutting parameters used for the primary were dependant on machining operation. For machining the optical surface with the fiducial tool, a feed rate of 25 mm/min and a cut depth of 25  $\mu\text{m}$  was used to reduce the time needed for each pass. 7 passes were required to create the hyperbolic shape. For rough machining of the fiducial, the feed rate was 10 mm/min and cutting depth was 20  $\mu\text{m}$ . The final pass on the fiducial was done at 1 mm/min. The final depth of cut for both surfaces was 1  $\mu\text{m}$  and the spindle speed was 530 RPM for all operations.

#### 2.5.4 Step 4: Secondary Mirror and Fiducial

The secondary mirror is also a hyperbolic surface but much smaller (~40 mm diameter) -- - a convex rather than concave shape. The optical surface is supported by three arms that

extend to a ring that mates with the tube via the same interference fit method as the primary. As with the primary, to guarantee axisymmetric features the optical surface and the fiducial were diamond turned sequentially without removal from the vacuum chuck between operations. The diamond turned secondary is seen in Figure 2-25.



**Figure 2-25:** Secondary mirror and support structure after diamond turning.

To vacuum this mirror to the spindle, a thin plate with a hole in the center (to allow the optical surface to protrude) was used to seal the area between the outside ring and the optical surface. The thin plate contacted the support arms, a ridge on the inside of the

ring and a ridge on outside the mirror surface; all three were co-planer and the ridges are shown in Figure 2-26.

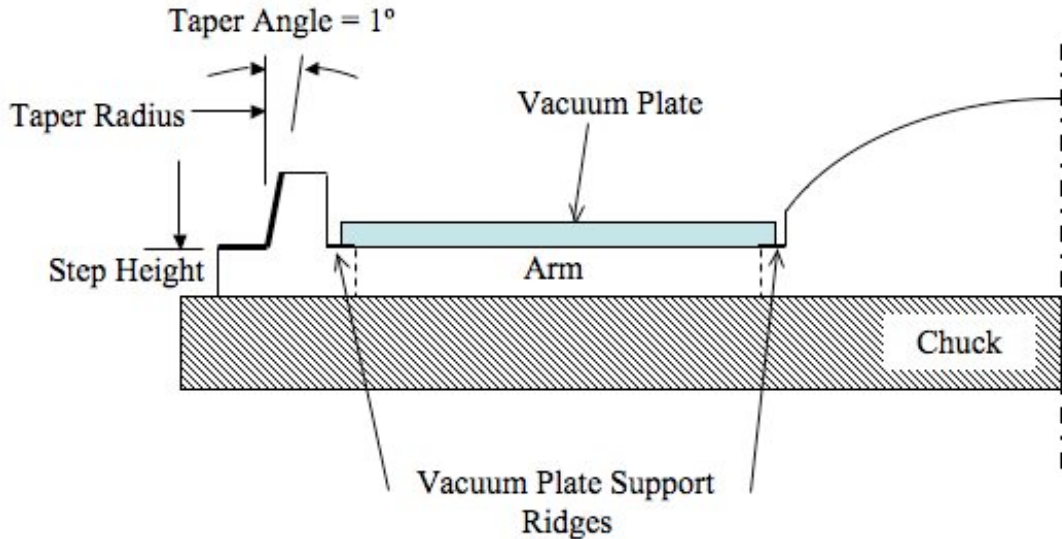


**Figure 2-26:** Secondary on Vacuum Chuck with Vacuum Plate. Critical Fiducial Surfaces are in Bold.

The machining processes for the critical surfaces were performed in the same manner as those used to fabricate the primary mirror because the secondary was designed with almost identical fiducials. The critical features were the step height from the chuck to the fiducial surface, the tapered surface ( $1^\circ$ ) and the radial location of the taper as shown in Figure 2-26. Again like the primary, the step height and apex height are both machined with respect to the chuck face which was set to Z reference and spindle centerline as discussed in Section 2.3.3 – 2.3.4.

The rough machined secondary was measured on a Brown & Sharp Gage 2000 Coordinate Measuring Machine (CMM). This CMM has micrometer resolution and the accuracy was verified to within 3  $\mu\text{m}$  using a 50.8 mm (2") gage block. The back surface of the mirror was measured by placing the reflective surface down, taking several points on the back of the fiducial step (set the reference plane), taking several points on the back of the mirror surface (set as the second plane) and calculating the distance between the planes along the optical axis with the CMM software. Figure 2-27 shows the digitized back of the secondary where the outer ring represents the back of the fiducial step and the mirror back is the cluster of points in the center (shown with points along the three legs for clarity). The measurement found that the back was offset approximately 20  $\mu\text{m}$  from the outer ring and the relationship between the surfaces is shown in Figure 2-28.

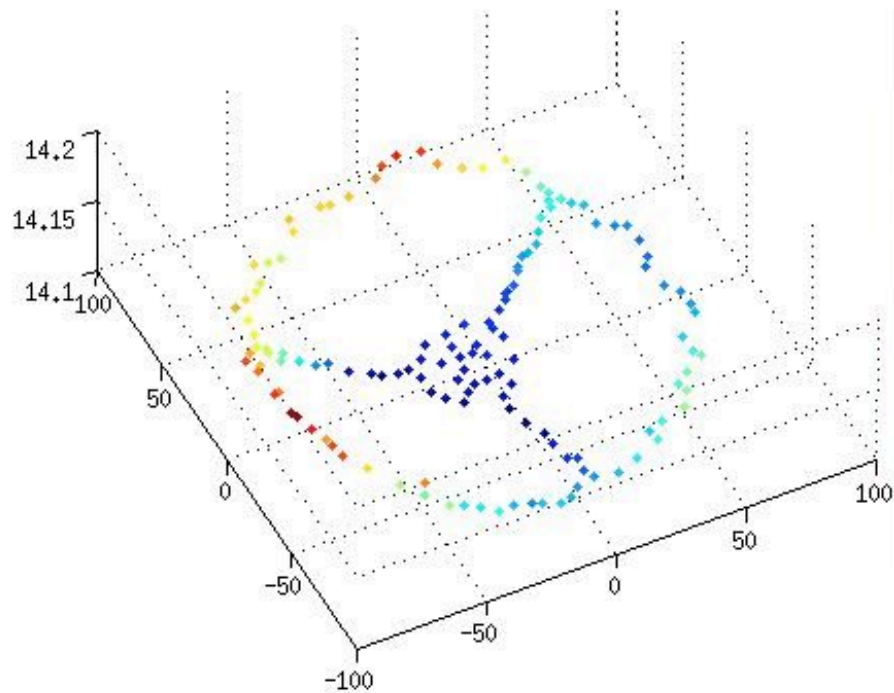


**Figure 2-27:** Digitized Secondary Back. Outer ring represents the back of the fiducial step. Center cluster is the mirror back. Points along the three legs shown for clarity.

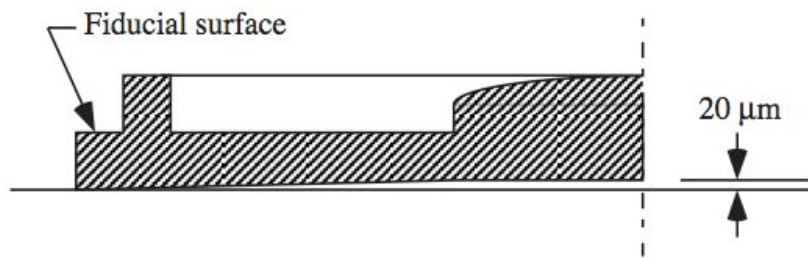


**Figure 2-28:** Cross section of secondary mirror structure illustrating the  $20 \mu\text{m}$  offset between the mirror back and the outer ring.

A force experiment was performed to measure the displacement of the optical surface when the secondary is vacuumed to the chuck. Because of the relationship between the

outer ring and the inner back, the secondary was placed on a marble metrology table with the reflective surface (pre diamond turned) facing up. A Chilton force gage was used to load the secondary with a force equal to that experienced while vacuumed to the chuck with 20 in. Hg. (approximately 90 N) and a Federal Gage LVDT indicator with involute tip was used to measure the deflection. The force gage was pressed against the rough reflective surface such that it deflected downwards into the surface of the marble table and the 20  $\mu\text{m}$  gap measured with the CMM was verified with the deflection observed with the LVDT. This critical distance on the diamond turned secondary is from the apex of the hyperbola to the fiducial surface. When loaded by the vacuum chuck, this distance is 20  $\mu\text{m}$  smaller than in the unloaded state. Therefore the controller was programmed to compensate this deflection by cutting the optical surface 20  $\mu\text{m}$  deeper with respect to the fiducial surface than designed and the result is discussed in Section 2.5.7.

Machining parameters used for the secondary were similar to those used for the primary. For machining the optical surface with the fiducial tool, a feed rate of 25 mm/min and a cut depth of 20  $\mu\text{m}$  was used because several passes were needed to create the hyperbolic shape from the rough-cut spherical surface. 4 passes were required machine the entire surface. For rough machining of the fiducial, the feed rate was 10 mm/min and cutting depth was 20  $\mu\text{m}$ . 7 roughing passes were required. The final pass on the fiducial was done at 1 mm/min. The final depth of cut for both surfaces was 1  $\mu\text{m}$  and the spindle speed was 530 RPM for all operations.

### 2.5.5 Step 5: Tube

The tube establishes the connection between the primary and secondary mirror. It sets the axial spacing as well as aligns the two optical axes. Each end includes a radial interference fit surface and a flat axial seating surface as seen in Figure 2-29. For the tube, the radial interference surface was designed as a shallow arc (constant radius) so it would mate with the 1° taper on the primary and secondary as line contact around the periphery of the fiducial. Tool radius compensation was done by simply adding the radius of the tool to the arc radius in the motion program. The tube was attached to a flat plate (previously turned on the DTM to prepare the tube-mounting surface) and the plate was vacuumed to the chuck as shown in Figure 2-30. The squareness error discussed in Section 2.5.1.1 would have caused the plate to have a similar cone shape but this would not affect the tube and is discussed in Section 2.5.7. The plate was attached to the tube (axial seating surface) using the 3 #4-40 threaded holes that will be used to attach the primary and the secondary to the tube. The 0.1 mm tool was used to machine the IDs, end faces, and OD references. The process was as follows:

1. Surface the plate.
2. Mount tube and machine a flat on the rough exposed surface.
3. Invert Tube.
4. Machine all fiducial surfaces simultaneously on primary end.
5. Machine centering reference on tube OD.
6. Machine a feature to distinguish the primary end.

7. Invert tube.
8. Center tube with OD reference.
9. Measure plate to tube end distance.
10. Machine all fiducial surfaces simultaneously on secondary end.

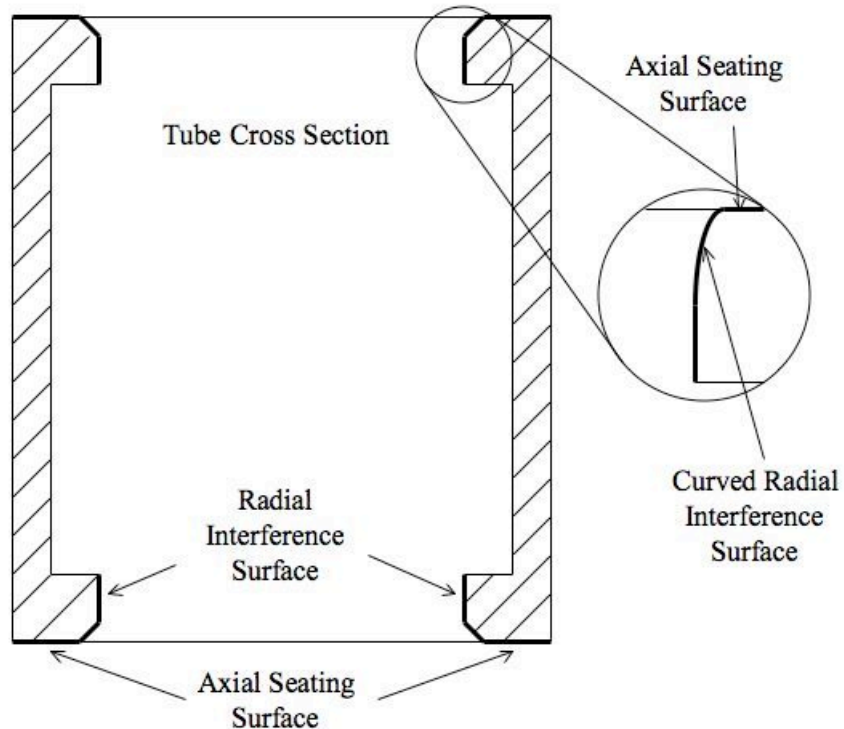


**Figure 2-29:** Tube cross section showing radial seating surfaces and axial seating surfaces.



**Figure 2-30:** Machining the tube with DTM.

To measure the tube length before machining the secondary fiducial, a Federal Gage LVDT indicator with involute tip was used to touch the surfaces and the laser interferometer output was used for length measurement. The resolution of the interferometers is 2.5 nm and the resolution of the Federal Gage, at its highest setting, is 100 nm between scale graduations. The LVDT indicator was attached to the X-axis table with a magnetic base and the Z-axis was jogged until the Federal Gage was in contact with the plate, where it was set to zero and the Z-axis interferometer coordinate was recorded. The Z-axis was jogged away and the X-axis was jogged a small distance to move the Federal Gage such that it would contact the tube end when appropriately positioned in Z. The Z-axis was then moved with closed loop commands until the reading on the Federal Gage returned to zero (within 500 nm). The Z-axis offset was compared to the previously recorded value and the tube length, as mounted, was calculated from the difference. The desired tube length (134.4 mm) was subtracted from

the measured length to find the amount of material left to remove. Measurement of the tube after machining found that it was machined 8  $\mu\text{m}$  short and is discussed further in Section 2.5.7.

### ***2.5.6 Step 6: Spacer***

The spacer sets the distance between the back surface of the primary and the camera body. It is connected to the primary with three machine screws and thin spacers that act as a semi-kinematic mount. As a reference surface for both the camera and primary, the thickness of this plate provides the most versatile adjustment for focus. Initially, spacer thickness was to be machined with a fly-cutter mounted to the DTM spindle. However, measurement of the rough machined spacer and optical assembly dictated that this step was not needed.

### ***2.5.7 Machining Results, Discussion and Suggestions for the Future***

Primary optical form error showed both rotationally symmetric and NRS errors. At the center of the issue is the low aspect ratio of 1:6 (thickness to diameter) [28], which made it susceptible to vacuum chuck induced distortions through elastic deformation. The symmetric errors were caused by a combination of the incorrect axes squareness as discussed in Section 2.5.2 - 2.5.3 and the incorrectly programmed tool radius as discussed in Section 2.5.3. The two combined errors added to a total PV error of more than 1  $\mu\text{m}$  [28]. NRS errors were observed during machining of the back face and on the optical

surface (hyperbolic roughing with small radius tool). Primary fiducial surfaces also exhibit form errors of similar magnitude and shape as the optical surface.

Measurement of the secondary revealed an optical surface with a form error of about 200 nm (NRS and RS) and a fiducial mounting ring with a form error of about 25  $\mu\text{m}$ . The 1:3 aspect ratio of the optical surface itself was high enough to prevent vacuum induced distortions. The predicted change in apex height when vacuumed (20  $\mu\text{m}$ ) due to the gap found between the fiducial ring and the optical back was successfully compensated as the apex to fiducial step error was measured at 3  $\mu\text{m}$ . The correlation of the distortions on the fiducial step surface with the three arms indicates that future support structures need be stiffer to reduced vacuum distortions. The squareness errors that had such a large effect on the primary were negligible in the secondary. This was because the optical surface aspect ratio was higher and the squareness error of about 200 nm over the secondary diameter would not be realized in the optical surface because of its higher thickness. The relationship between the outer ring the optical surface would have only been affected by about 700 nm, a distance not resolvable by the CMM measurements.

The actual surface finish of each optical component was on the order of 5 nm RMS. This was a much larger value than the theoretical values, which were 0.57 nm RMS for the primary and 0.19 nm RMS for the secondary. In the past, RMS roughness machined in pure copper was about 2 nm RMS. Chapter 4 of this thesis deals with surface finish and machine vibration; it also discusses the importance of tool sharpness.

During operation of the Federal Gage over several months following fabrication of the tube, it was found that the gage might not repeat its position relative to the workpiece when the tip lost contact with the measurement surface. This is the most likely source of the 8  $\mu\text{m}$  machining error. Future cutting operations perform workpiece touch-offs to set machining lengths which utilize the ASG-2500 high-resolution laser interferometers and high precision slides.

The roundness of the tube ID was 25  $\mu\text{m}$  and the end flatness was 3  $\mu\text{m}$ . Between machining operations the tube was unbolted and remounted to the machining plate. Before unbolting, a portion of the OD was diamond turned and measured to less than 1  $\mu\text{m}$  runout. However, upon remounting the runout was approximately 25  $\mu\text{m}$ . The runout was caused by distortions introduced by mounting the tube to a plate with a low aspect ratio (easily distorted by vacuum forces) and using large screw torques to hold the tube to the plate (40 lbs clamping force per screw). Because the tube had a high aspect ratio (the width was less than the length), mounting distortions seen in the runout did not have a large effect on the end exposed for machining. Future designs should use a plate with a step in the back to reduce the area exposed to vacuum pressure so distortions from vacuum forces are reduced and should calculate the minimum screw torque need to adequately seat the workpiece to the vacuum plate.

Cutting a sphere with a radius best-fit to the hyperbolic mirror before final machining would allow for easy form error measurements with the Zygo GPI and would reveal the rotationally symmetric and NRS errors. To correct the rough machined distortions, a

tool servo could have been programmed to cut an inverse error shape before final machining operations began. Another possible method for large diameter workpieces would involve cutting a notch into the chucking surface such that diameter contacting the vacuum chuck is much smaller. This smaller diameter would effectively change the aspect ratio such that the workpiece is less susceptible to vacuum induced distortions. The form errors found in the primary set the direction for the next chapter of this work; form error capability of the DTM.

## 2.6 CONCLUSIONS

The methods used to create the hyperbolic optical surfaces and the fiducial surfaces were effective. Two tools were simultaneously used to machine the two surface types and each tool was adequately centered with respect to the X, Y and Z-axes. The tool nose radius compensation technique and motion path programming techniques were effective. Procedures were developed to machine whole components in a single part chucking so optical surface and fiducial alignment distances were preserved. The primary mirror contained axisymmetric errors because it was easily distorted by vacuum chuck forces and the DTM error shapes were not compensated. It also contained non-rotationally symmetric (NRS) errors from rough machining that were not removed by diamond turning because of these vacuum chuck distortions. The low aspect ratio (thickness to diameter) of the primary is the reason that it distorts so readily. In future operations, the NRS errors could be removed with use of tool servo. The secondary back was not flat,

but it was adequately corrected during diamond turning. The tube has a length error of 8  $\mu\text{m}$  that was associated with the measurement technique used during final machining.

### **3 FORM ERROR OF ASG 2500 DIAMOND TURNING MACHINE**

#### **3.1 INTRODUCTION**

The measurements of the surfaces created for the two-mirror design showed significant non-rotational symmetric form errors in addition to rotationally symmetric form errors that indicated problems with the setup of the ASG-2500 diamond turning machine. The vacuum chuck flatness and axes squareness were two parameters that influenced the shape of the primary mirror. Over the past 15 years, a number of experiments have been performed to study the errors in this machine as discussed in Section 1.3. What follows is a summery of a significant portion of those results and experiments that verify the machine capability. The goal was to determine the capability of the ASG-2500 DTM to fabricate flat and spherical surfaces by measuring peak-to-valley (PV) form error. The end goal was to make a surface equal to or less than  $\lambda/4$  (0.25 wavelengths HeNe  $\sim 150$  nm) as prescribed by the Rayleigh criterion [31]. Thermal expansion of work pieces due to handling contact was studied along with spindle expansion due to transient heating effects of startup.

After two-mirror fabrication was completed, the host PC was upgraded to an Intel® Celeron® (a x86 class processor and instruction set) operating at 2 GHz. Although a potential significant upgrade, the coprocessor board for machine control and input/output devices discussed in Section 2.5 remained. The upgrade was transparent for the discussions in this and subsequent chapters.

## 3.2 DTM ERROR BUDGET

An error budget was completed on the ASG 2500 DTM in 1991 [3]. To create high quality optical surfaces, repeatable errors in the machine must be compensated. Such errors are introduced through the environment, machine geometry, and thermal expansion during spindle startup.

### 3.2.1 *Environment*

The labs at the PEC are designed to provide an environment conducive to high precision machining. Temperature stability is critical for dimensional stability and the actual temperature in each laboratory room is  $20 \pm 0.05$  °C [4]. The laser interferometer system used on the ASG is open to the ambient air so it is sensitive to temperature changes as well as humidity, barometric pressure and carbon dioxide content. The floor of each lab is a concrete slab that is resting on a specially designed vibration isolation device. It is made from a rubber material that provides the desired stiffness and high internal damping. The intent of the rubber isolation is to set the first natural frequency of the floor (50-60 Hz for the lab used in this thesis) below the first natural frequencies of the lab equipment. Frequencies higher than the lab floor resonance are attenuated. As discussed in section 4.3.1 through 4.3.1.3 the ASG-2500 z-slide with spindle mounted has a natural frequency just above the lab floor.

### *3.2.2 Machine Geometry: Slide Straightness and Automatic Compensation*

Each axis has 5 constrained degrees of freedom: straightness in the vertical and lateral direction plus the angular motions of roll, pitch and yaw. The geometry of the ASG-2500 is designed to reduce Abbe offsets by placing the sensors as close to the axis motion as possible and reduce error motions by using a T-lathe configuration with high precision hydrostatic slide ways. Figure 3-1 shows a three dimensional layout of the ASG-2500 slide geometry labeled with respective degrees of freedom. The interferometer cubes for both axes are at the nominal tool height, which is coplanar with the spindle centerline in the vertical direction. The Z-slide interferometer in the X-direction is as close to the spindle centerline as possible (the spindle housing is about 5 inches in diameter) and it is positioned directly behind the oil guard on the Z-slide (about 3 inches from the chuck face). The X-slide interferometer is placed behind the oil guard in a Z-direction location where the tool is commonly located. Because of the geometric layout, the errors can be reduced to three motions: X-axis straightness, Z-axis straightness, and Z-axis yaw [5]. X-axis straightness contains lateral (Z-direction) and vertical (Y-direction) straightness plus roll, pitch and yaw. Z-axis straightness represents the same error motions except Z-axis yaw error, which is discussed in Section 3.3. Straightness measurements were recorded using a Zerodur straight edge supported by a custom fixture [5]. The fixture allowed use of the ‘reversal’ technique such that form errors in the straightedge can be canceled out of the reported slide errors [6].

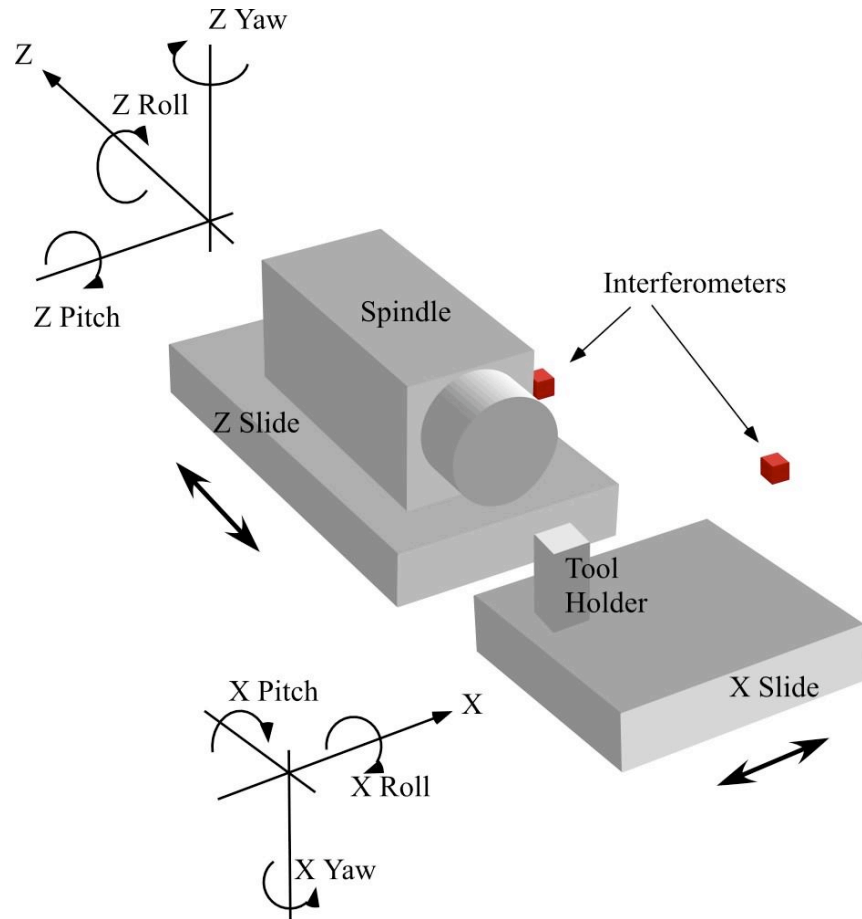


**Figure 3-1:** Geometrical layout of the ASG-2500 slides with directions labeled. Z interferometer is next to the spindle and X interferometer is right of tool holder; for clarity, the interferometer mounting plates and oil guards are not shown.

Squareness of the X-axis and Z-axis is realized through the relationship between the spindle centerline and the X-slide because the spindle is mounted to the Z-slide with the axis of rotation approximately collinear with the Z-axis. Previous work indicated that it was very difficult to perfectly align the spindle with the X-axis physically, so a squareness variable was added to the yaw correction scheme as discussed in Section 3.3 [3].

Error shapes for each axis error were repeatable with a  $\pm 3\sigma$  variation of approximately 20 nm. The X-axis shows a peak to valley (PV) error of 200 nm over its entire 250 mm travel [4] with features that indicate the pitch (5 mm) of the ball screw drive system [7]. The Z-axis shows a PV error of 60 nm over its 150 mm travel [5]. Error maps were created from these measurements for the ASG controller in the form of lookup tables. Figure 3-2 shows both the uncorrected (dashed) and the corrected (solid) straightness error motions for the X-axis in the Z direction (Figure 3-2a) and the Z-axis in the X direction (Figure 3-2b) over the full ranges of travel. Straightness using the look up tables for automatic error compensation is 40 nm peak-to-valley for both axes.

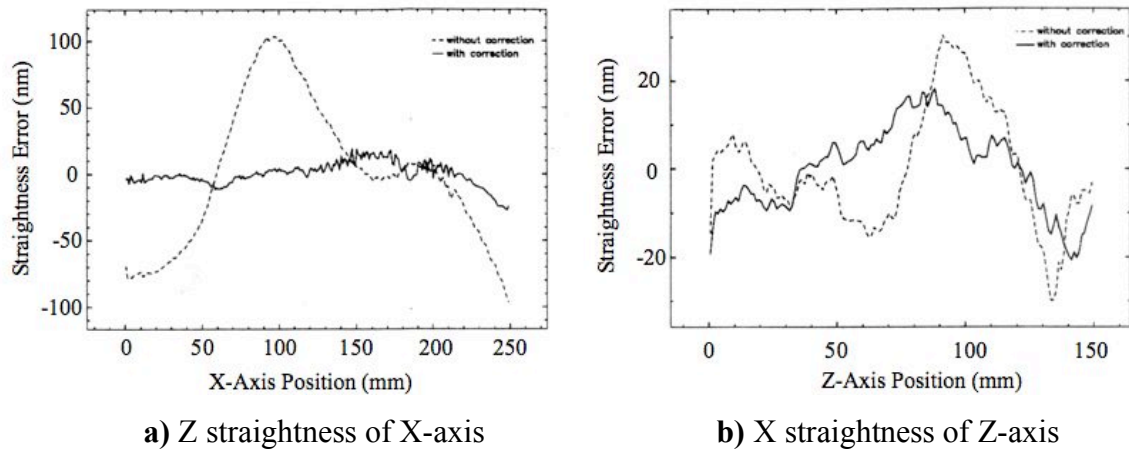


**Figure 3-2:** X and Z-axis straightness (note scale difference) with (solid line) and without (dashed line) compensation from the orthogonal slide. [4]

The automatic straightness error compensation was activated for all experiments reported in Section 3.3 and 3.4 but was not on for the optical fabrication of the primary and

secondary mirrors. This could be done because the routine written for automatic error correction had an option to employ the straightness compensation without activating the yaw and squareness compensation called “no yaw” as seen later in Table 3-1.

### *3.2.3 Thermal Growth of Spindle*

Heating effects caused the spindle of the ASG 2500 to grow in length (Z-direction) when started from a standstill at room temperature [7]. Several long-term tests determined the time required to achieve steady state operation and transient effects caused by the stopping and restarting of the spindle. Transient effects were modeled around typical start-up/shut-down operations such as the shut-down time required to measure a part, perform tool changes and complete setup routines. Results of the longterm tests indicated that at 1000 rpm the spindle takes 8 to 12 hours to reach a steady state growth of 1500 nm. Transient cycling tests revealed that once the spindle is stopped and restarted to 1000 rpm, it requires a re-stabilization time equal to the time it was shutdown. The re-stabilization time was minimized by only stopping the spindle long enough to remove the part, vacuum a silicon disk to the chuck (the air bearing spindle collects oil and dust if the chuck is not vacuumed sealed) and restart the spindle. Also, for workpiece mounting the spindle was stopped only long enough to vacuum it to the chuck and center it with respect to the spindle.

### 3.3 DIAMOND TURNED FLATS

A series of experiments were conducted to measure the capability of the DTM to machine a flat surface as shown in Figure 3-3. The tool is programmed to move through a rectangular path. The cutting leg of the rectangle is started beyond the OD of the part and moves to the center. A stream of oil, directed at the tool and spraying from the OD towards the center of the part was used to remove chips. Spindle rotation was 500 rpm counter-clockwise. The diamond tool used had approximate radius of 5.45 mm and the cross-feed rate was set at 5 mm/min. A 10 to 15  $\mu\text{m}$  depth of cut (DOC) roughing pass was performed followed by a finishing pass of 2  $\mu\text{m}$  DOC.

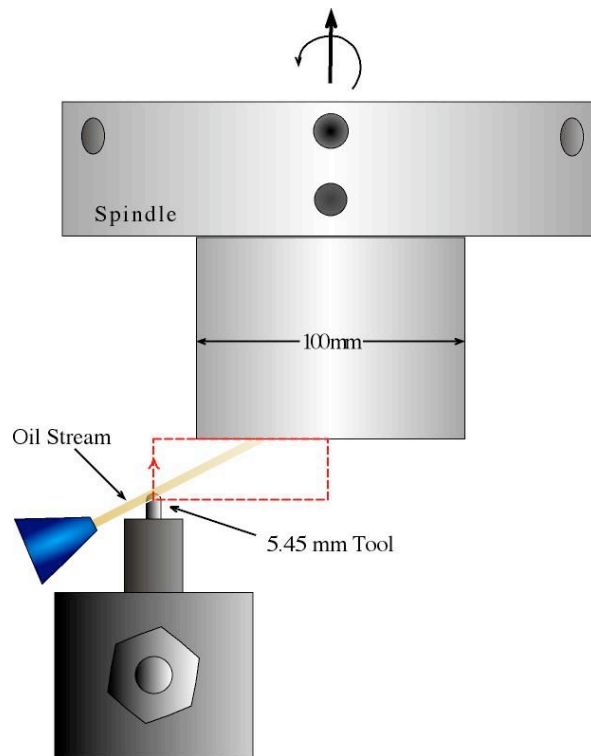


**Figure 3-3:** Tool path and oil spray for diamond turned flats experiment. To scale.

The flats were machined from a 6061-T6 aluminum alloy cylindrical workpiece with a diameter of 100 mm and a thickness of 75 mm. The aspect ratio (thickness/diameter) of this workpiece is 0.75, which is much higher than the primary mirror blank discussed earlier. This should reduce the distortion in the finished surface as a result of a non-flat vacuum chuck or workpiece-chucking surface.

### *3.3.1 Yaw Error, Squareness of Spindle to X-axis and Automatic Compensation*

The change in the yaw of the Z-axis as it moves combined with the squareness between the spindle centerline (spindle centerline is approximately parallel to Z-axis) and the X-axis have a significant effect on surface form error [3]. Measurements revealed that the axis yaws nearly linearly and the magnitude is +1.6 arcsec (clockwise looking down on the spindle as viewed from the ceiling) over its full 150 mm length. The yaw measurement was repeatable for the Z-axis. Figure 3-4 shows how both the slide and spindle yaw as they travel over the 150 mm range of travel when the spindle centerline is assumed square (yaw = 0) at Z = 0. Because yaw error is repeatable, it can be compensated in real time according to the expression:

$$Z_{comp} = (X_{pos} - X_0)(\delta_{slope} Z_{pos} + Slope_0) \quad (3-1)$$

where  $(X_{pos} - X_0)$  is the X distance from the spindle rotation axis,  $\delta_{slope}$  is the linear change in slope along the Z-axis (1.6 arcsec./150 mm) and the intercept is  $Slope_0$  (yaw magnitude or axes squareness at  $Z = 0$ ) [3]. The intercept may vary, as the spindle can be unbolted and its angular orientation changed. For this reason, measurements and test cuts were performed to find this intercept (squareness).

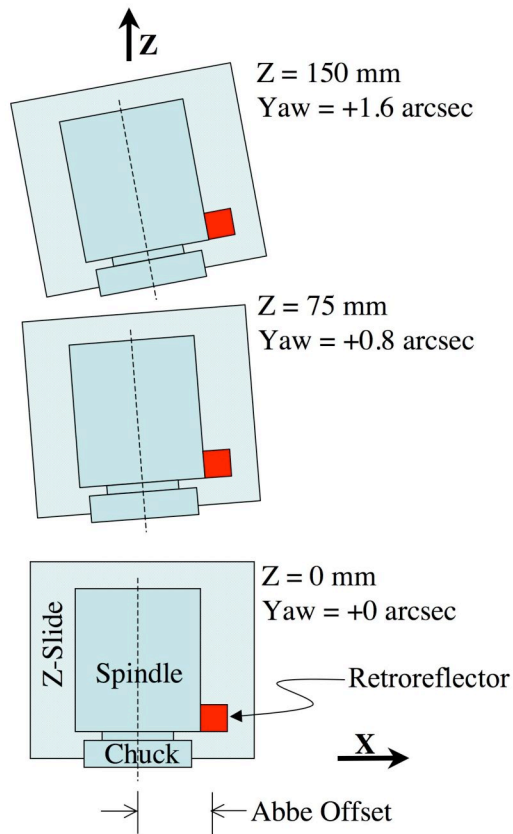


**Figure 3-4:** Z-axis yaw over full 150 mm range is 1.6 arcsec.

The position measuring system on the Z-axis ( $Z_{pos}$ ) has an Abbe offset ( $X_{pos} - X_0$ ) from the location of the centerline of the spindle to the laser retroreflector. The effect of the

Abbe offset is negligible when performing an operation where the Z-axis is held constant; however, any operation where the Z-axis moves will be affected. Miller [3] measured the Abbe offset and modified the linear yaw and squareness compensation equation to account for its effect in 1991. In the present work, several test pieces were cut to verify the error compensation program and to identify the squareness (yaw intercept) for the machine in 2006.

### *3.3.2 Optical Flat Test Results*

The surface profiles were measured with a Zygo GPI XPHR form measuring interferometer and evaluated with MetroPro software. For consistency, the MetroPro automatic aperture edge-trimming feature was used. This is intended to eliminate any interferometric artifacts at the part edge and was set at the default of 95%. Figure 3-5 shows the GPI with an interferometric image and MetroPro running from a PC.



**Figure 3-5:** Zygo GPI HPXR form measuring interferometer with MetroPro software.

The results of 16 machining tests used to find the yaw error compensation values are shown in Table 3-1. Explanation of each experiment follows this brief summary of the table columns. *Z-axis* coordinate is the absolute position of the Z-slide during the cut and also serves as the Z intercept to set the squareness for automatic yaw compensation. *PV surface* is the total peak-to-valley measurement over the full aperture of the specimen. This includes any non-rotationally symmetric features. *PV Trace* is a single trace at an arbitrary angle that passes through the center and across the entire diameter of the work piece. The differences between the *PV Trace* and *PV Surface* represent the non-rotationally symmetric (NRS) form errors seen during optical flat fabrication. They range from 70 nm to 25 nm. Some authors [9] have suggested that large nose radius

tools, like the 5.45 mm radius tool used for this experiment, cause greater NRS errors than smaller tools (< 0.75 mm).

**Table 3-1:** Results of 6061 T-6 Aluminum machining test to produce flat specimens.

\*For Tests 15 & 16, the automatic mask was set to 5% ID and still used 95% OD.

| Test | Z-axis<br>(mm) | PV<br>Surface<br>(nm) | PV<br>Trace<br>(nm) | Manual<br>Compensation<br>(nm) | Automatic<br>Compensation<br>(arcs, z mm) | Mean<br>(nm) | St. Dev<br>(nm) |
|------|----------------|-----------------------|---------------------|--------------------------------|---|--------------|-----------------|
| 1    | 1.2            | 244                   | 174                 | 600                            | no yaw                                    | 213          | 23.9            |
| 2    | 1.2            | 216                   | 144                 | 600                            | no yaw                                    |              |                 |
| 3    | 1.2            | 202                   | 166                 | 600                            | no yaw                                    |              |                 |
| 4    | 1.2            | 188                   | 125                 | 600                            | no yaw                                    |              |                 |
|      |                |                       |                     |                                |   |              |                 |
| 5    | 1.2            | 250                   | 185                 | -                              | 1.03 1.2                                  | 228          | 49              |
| 6    | 1.2            | 164                   | 132                 | -                              | 1.03 1.2                                  |              |                 |
| 7    | 1.2            | 222                   | 196                 |                                | 1.03 1.2                                  |              |                 |
| 8    | 1.2            | 279                   | 236                 |                                | 1.03 1.2                                  |              |                 |
|      |                |                       |                     |                                |   |              |                 |
| 9    | 1.2            | 290                   | 237                 | -                              | 0.7 1.2                                   | 275          | 32              |
| 10   | 1.2            | 300                   | -                   | -                              | 0.7 1.2                                   |              |                 |
| 11   | 1.2            | 290                   | -                   | -                              | 0.7 1.2                                   |              |                 |
| 12   | 1.2            | 220                   | 168                 | -                              | 0.7 1.2                                   |              |                 |
|      |                |                       |                     |                                |   |              |                 |
| 13   | 20             | 227                   | 184                 | -                              | 0.7 1.2                                   | 199          | 31              |
| 14   | 20             | 206                   | 183                 | -                              | 0.7 1.2                                   |              |                 |
| 15*  | 20             | 219                   | 161                 | -                              | 0.7 1.2                                   |              |                 |
| 16*  | 20             | 147                   | 98                  | -                              | 0.7 1.2                                   |              |                 |
|      |                |                       |                     |                                |   |              |                 |
| 17   | 24             | 184                   | 97                  | -                              | 1.7 0                                     | 174          | 11              |
| 18   | 127.9          | 173                   | 107                 | -                              | 1.7 0                                     |              |                 |
| 19   | 1.25           | 157                   | 105                 | -                              | 1.7 0                                     |              |                 |
| 20   | 74.8           | 184                   | 112                 | -                              | 1.7 0                                     |              |                 |

An example of the measurement of a 6061-T6 aluminum flat is shown in Figure 3-6. The top down view of the entire part showing the machined shape is at the left. The surface is close to flat but the center is higher than the edges. The PV is 227 nm or approximately  $\lambda/3$ . The trace along the line in the top view is shown at the right. The profile of this trace is a more obvious measurement and the PV of this trace is 160 nm or  $\lambda/4$ . For Tests 1-4 in Table 3-1, the motion of axis was manually corrected (the same amount for each test). By repeating the same compensation for each test, the variation between machining passes machine was observed to have a standard deviation of 24 nm. Starting at Test 5, the automatic compensation routine was activated and the linear intercept values put in the controller are in last column. Like the manual compensation tests, the same automatic compensation values were tested several times. Summary of the tests in Table 3-1 are discussed next.

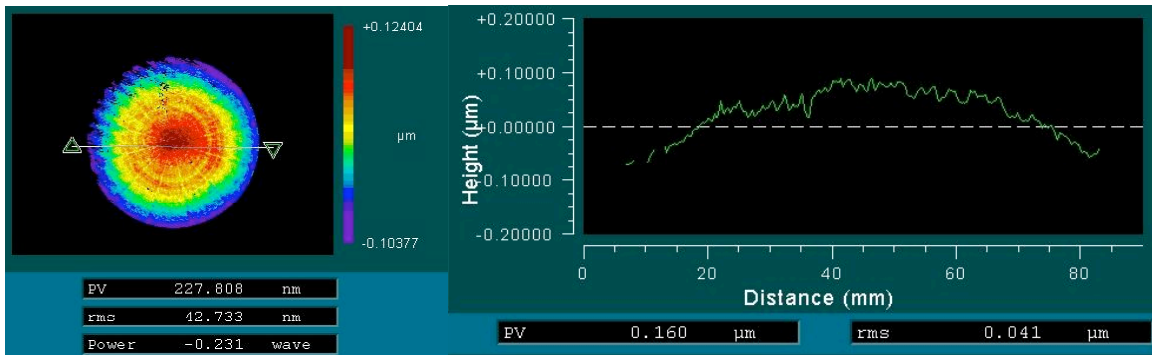


**Figure 3-6:** Example trace (#13 from Table 3-1) of 6061 T-6 flat machined on the DTM with yaw correction of 0.7 arc-seconds.

### 3.3.3 *Table 3-1, Tests 1-4: Manual Compensation*

Z-axis yaw and axes squareness lead to a cone shaped feature in the flat that may be concave or convex. Manual modification of the part program was used to remove cone shape caused by the z-axis yaw by programming a tool path that was the inverse of the measured shape. Rather than hold position, the Z-axis was programmed to move a small distance as the X-axis transverse the tool across the face of the part.

Experiments have shown that the slides are capable of sustaining very low velocity motions with deviation from the commanded position of less 20 nm. A plot of a 16  $\mu\text{m/sec}$  move of the X-axis is found in Figure 3-7. The results of Tests 1-4 indicated that the Z-axis yaw at  $Z = 1.2 \text{ mm}$  was 10  $\mu\text{rad}$  (2 arcsec.) or 600 nm at a radius of 60 mm. The uncorrected shape was a convex cone. The corrected shape was also convex with *PV traces* of approximately 160 nm as seen in Figure 3-8.

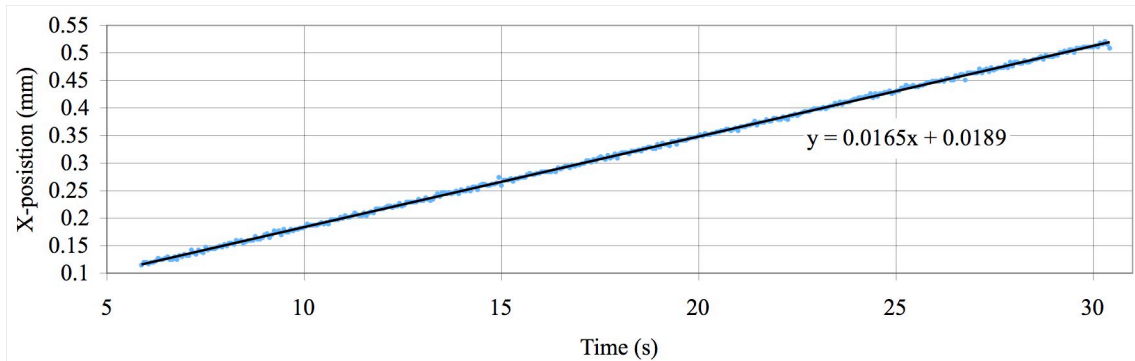


**Figure 3-7:** Slow velocity x-axis move. Linear curve fit slope = 0.0165 mm/s.

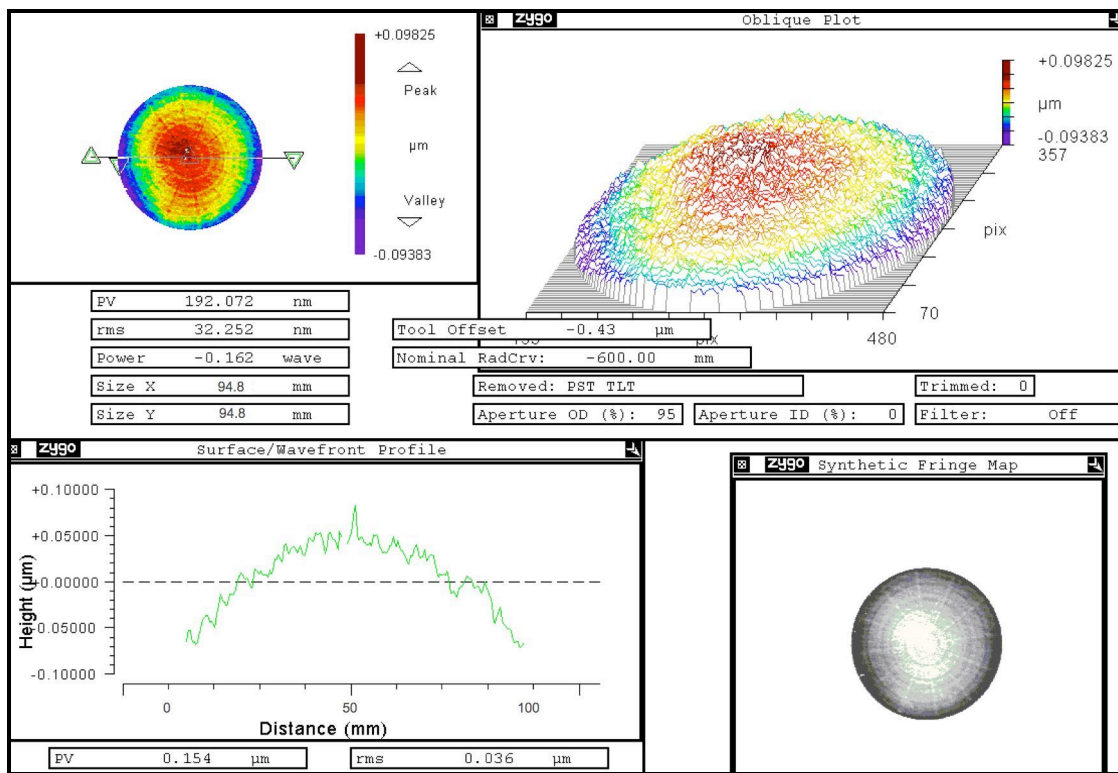


**Figure 3-8:** Final manually corrected squareness error showing convex shape.

### **3.3.4 Table 3-1, Tests 5-16: Automatic Compensation**

Based on the results of the manual compensation tests, the ASG 2500 automatic compensation routine was re-implemented to correct for Z-axis yaw and axes squareness. Again, the results are in Table 3-1. The intercept (axes squareness) for the yaw compensation routine was calculated from the results of the manual compensation experiments. The first estimate for squareness was yaw = 1.03 arcsec at Z = 1.2 mm. Tests 5-8 were conducted and the shape of the cone changed from convex (during manual compensation) to concave. The squareness was then changed to yaw = 0.7 arcsec at z = 1.2 mm for Tests 9-12, which resulted in the same convex shape seen in the manual compensation tests.

To prove the robustness of automatic yaw compensation the tool was moved such that Z = 20 mm for Tests 13-16. The compensation expression is the same as was used in Tests 9-12 (Table 3-1) which were machined at Z = 1.2 mm. The results at Z = 20 mm have error magnitudes like the tests at Z = 1.2 mm and were similarly convex.

### **3.3.5 Squareness Setting Revisited by Comparison with a Larger Diameter Flat**

As part of a fiducial alignment and mirror-mounting test, a 160 mm diameter, 25 mm thick 6061-T6 mirror was fabricated [22]. This experiment was performed a few months after the flat tests were completed and the spindle remained undisturbed from the orientation used during the flat tests. This flat was similar to the primary mirror of the

two-mirror telescope discussed from Section 2.5.3 in dimension and material. The back of the mirror had a step cut into the outer diameter such that only 100 mm of diameter was in contact with the vacuum chuck. This increased the aspect ratio of the loaded section from 1:6 found in the primary to 1:3. This step reduced the potential for distortion generated by vacuum chucking forces. The vacuum chuck was surfaced and it was found to have a figure error of approximately 400 nm of PV with a convex cone shape. The modeled deflection of the optical surface of this mirror from the measured chuck shape was less than 40 nm [22]. The first machining pass revealed a shape similar to Figure 3-6 but had PV of more than 400 nm. By comparing the motion paths of the program used to cut this mirror and the motion program used to cut the optical flats in Section 3.3.4 - 3.3.5, it was found that the OD of both programs started at approximately the same X, Z-coordinate of (220, 24). The flats machined earlier in this section stopped at X = 170 while the larger mirror cut here continued to X = 140. A comparison of the shapes and error magnitudes with relative DTM coordinates is in Figure 3-9.

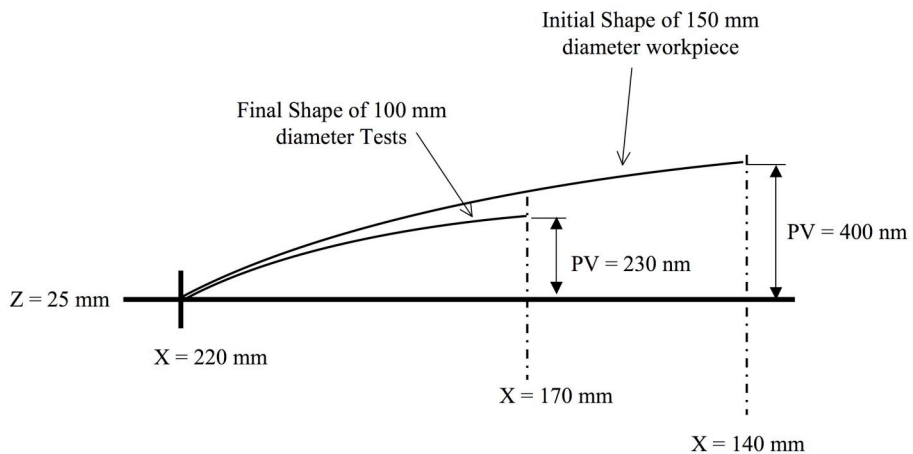


**Figure 3-9:** Comparison of 6061 workpiece and the final shape of the flat tests.

After comparison, it was decided that the ASG-2500 yaw compensation routine be adjusted because this figure error could be attributed to an squareness error between the axes. The similar shape of the parts indicated that the correction routine was repeating the results of Tests 5-16 in Table 3-1, however the PV of the 6061 workpiece was too large. 400 nm of slope for 80 mm of aperture diameter translated to an additional squareness error of 1.0 arcsec so the intercept was changed from yaw = 0.7 arcs at z = 1.2 mm to yaw = 1.7 arcsec at z = 0 mm. The small change in Z coordinate is insignificant when compared to 1.6 arcsec of yaw over the entire 150 mm range of the Z-axis (yaw = 0.01 arcs over 1.2 mm). The final surface was concave (convex before) in shape with a the same slight curvature, but the PV was reduced to 170 nm and is seen in Figure 3-10.

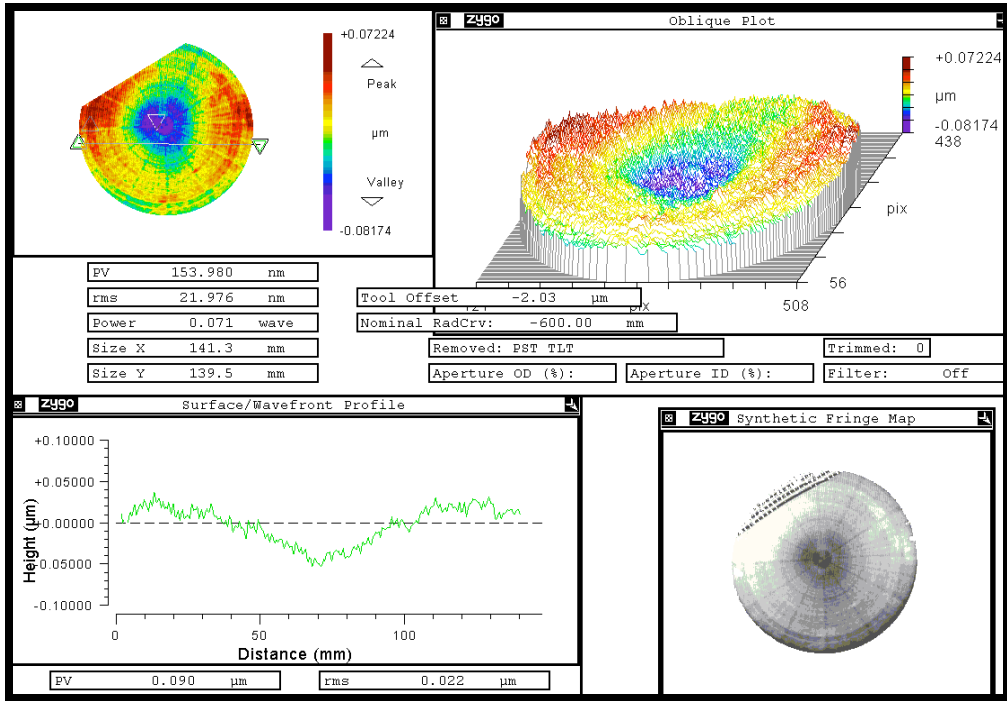


**Figure 3-10:** 6061-T6 workpiece with 150 mm optical surface diameter. Upper left corner trimmed out because it was not machined during this pass.

### 3.3.6 Table 3-1, Tests 17-20: Final Yaw and Squareness Setting

After the final yaw setting was implemented for the fiducial experiment in Section 3.3.5, the reflective flat was cut again as indicated in Table 3-1 as Test 17. A spindle speed of 500 rpm was used, but the process differed in that the tool radius was 0.5 mm (5.45 mm before) and feed-rate was 3.2 mm/min for a cut duration of 16 minutes. The initial pass did not clean up, necessitating a second finish pass at 2  $\mu\text{m}$  depth. Z-axis position was 23.689 mm. The spindle had been running for more than 24 hours. The error level, as shown in Table 3 as  $\text{PV} = 180 \text{ nm}$  or  $\lambda/3.5$ , was smaller than with the previous tests.

Similar to Figure 3-10, the form was lower at the center than at the edge. The RMS form error was 21.5 nm or  $\lambda/30$  and the GPI measurement can be seen in Figure 3-11.

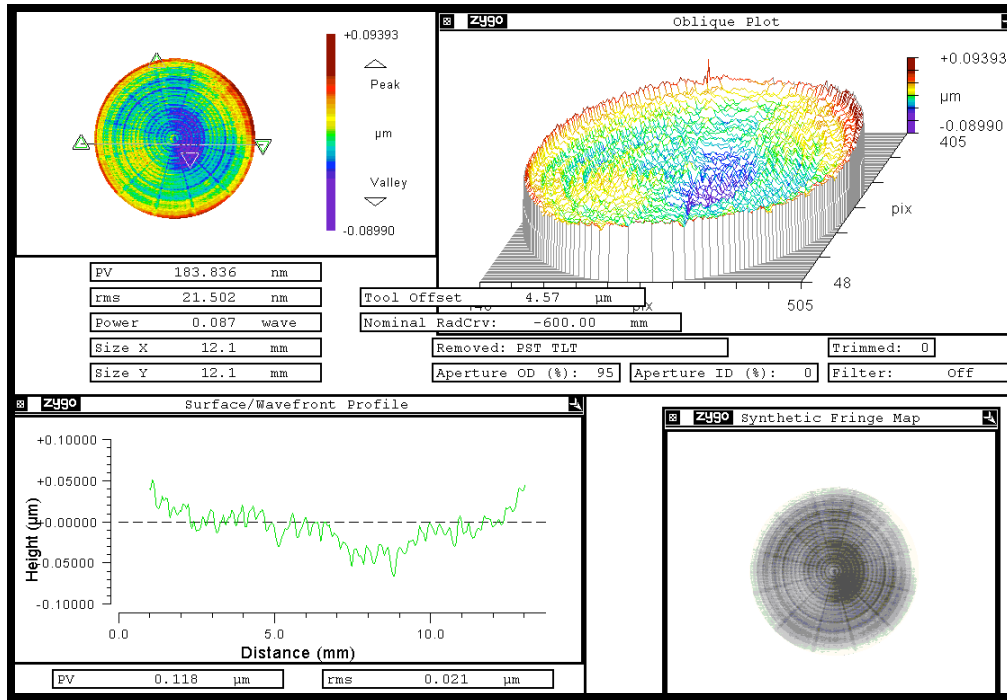


**Figure 3-11:** Final flat measurement from GPI with final squareness correction. PV error of 183 nm or 0.29  $\lambda$ .

Tests 18, 19 and 20 in Table 3-1 were also cut using the final yaw and squareness setting to verify that automatic compensation is effective for the entire Z-axis travel (150 mm). They were cut at Z-locations of 127.9 mm, 1.25 mm, and 74.8 mm respectively using identical machining conditions. They all had similar error levels ( $\text{PV} < 180 \text{ nm}$ ) and shapes as Test 17.

### 3.4 DIAMOND TURNED SPHERE

After the flat experiments were conducted, a sphere was machined to test the form error of the ASG when both axes are in motion. The programmed path was set to have a trajectory similar to the flat program, where the cutting leg started beyond the OD of the part and moved to the center. A stream of oil (Mobilmet Omicron®), directed at the tool and spraying from the center of the part towards the OD, was used to lubricate the cut and remove chips. Spindle rotation was 500 rpm counter-clockwise. The diamond tool used had an approximate radius of 0.5 mm and the feed rate was 3.2 mm/min. A finish pass with a 2  $\mu\text{m}$  cutting depth was used.

The sphere was 6061-T6 aluminum alloy. Like the flats in Section 3.3, the workpiece diameter was 100.4 mm and the thickness was 75 mm, which provided the same aspect ratio and resistance to distortions in the optical surface introduced by a non-flat vacuum chuck. The programmed radius of the convex sphere was 275 mm. Using an aperture diameter of 100.4 mm, the spherical sag was 4.7 mm and the f/# was 2.74 (for a finite conjugate). During the machining pass, the ASG-2500 Z-axis moved almost 5 mm and the X-axis moved 52 mm.

The Zygo GPI form measuring laser interferometer was fitted with a length measuring interferometer for evaluation of the sphere. This setup allowed precise measurement of translating stage travel on the Zygo GPI so the sphere radius could be measured. Figure 3-12 shows the GPI stage with the retroreflector attached, the interferometer mounted to the base and the HP laser source with white lines to indicate the beam path. The “cat’s

“cat’s eye” technique [26] was used to set the zero position of the translating stage by aligning the apex of the workpiece with the focus of the GPI reference element. A shape resembling a “cat’s eye” is seen on the interferometric image when the optical focus is aligned to the apex of the sphere. The analytical measure used to find perfect apex-to-focus alignment is power (curvature or spherical radius) of the interferogram. The focus point was found by translating the stage until the power is near zero (the interferogram has little curvature) and an example is seen in Figure 3-13.

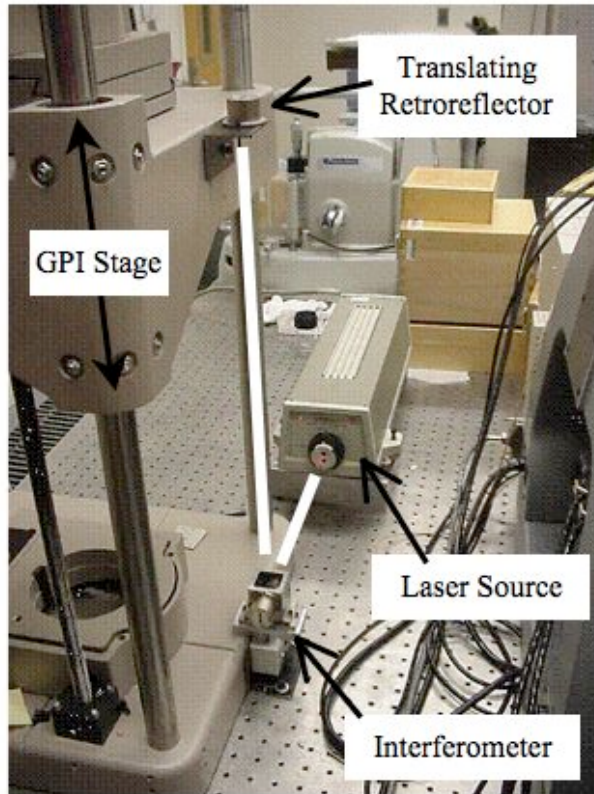


**Figure 3-12:** Zygo GPI Form Measuring Laser Interferometer Stage fitted with a Length Measuring Interferometer.

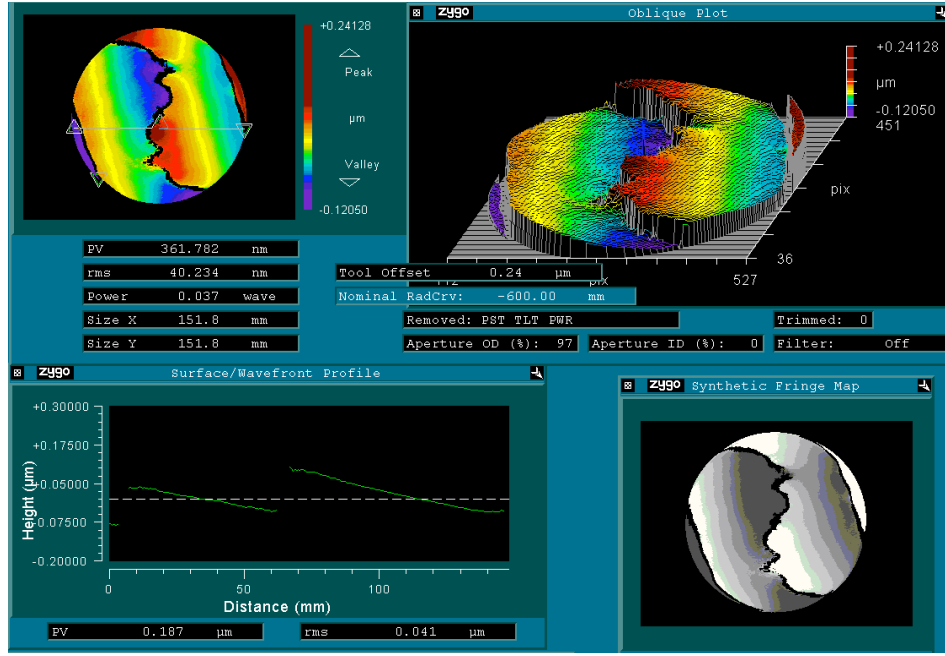


**Figure 3-13:** Interferogram seen when the GPI focus is aligned with the apex of the sphere using the “Cat’s Eye” technique. Power is almost zero ( $0.037 \lambda = 23 \text{ nm}$  radius). Horizontal and vertical scales should be ignored because this measurement is an interferogram of a spot (apex of the sphere).

The average of three measurements of the final workpiece showed that the form error, with power (or spherical radius error) removed, was  $PV = 156 \text{ nm}$  or  $\lambda/4$ . The measured spherical radius errors or the distances from the reference element focus where power was equal to zero were 1, -2, and -5  $\mu\text{m}$ . This variation shows that the measurement of the translating stage has, at best, a precision of 6  $\mu\text{m}$ . Figure 3-14 shows the measurement from the GPI with power removed.

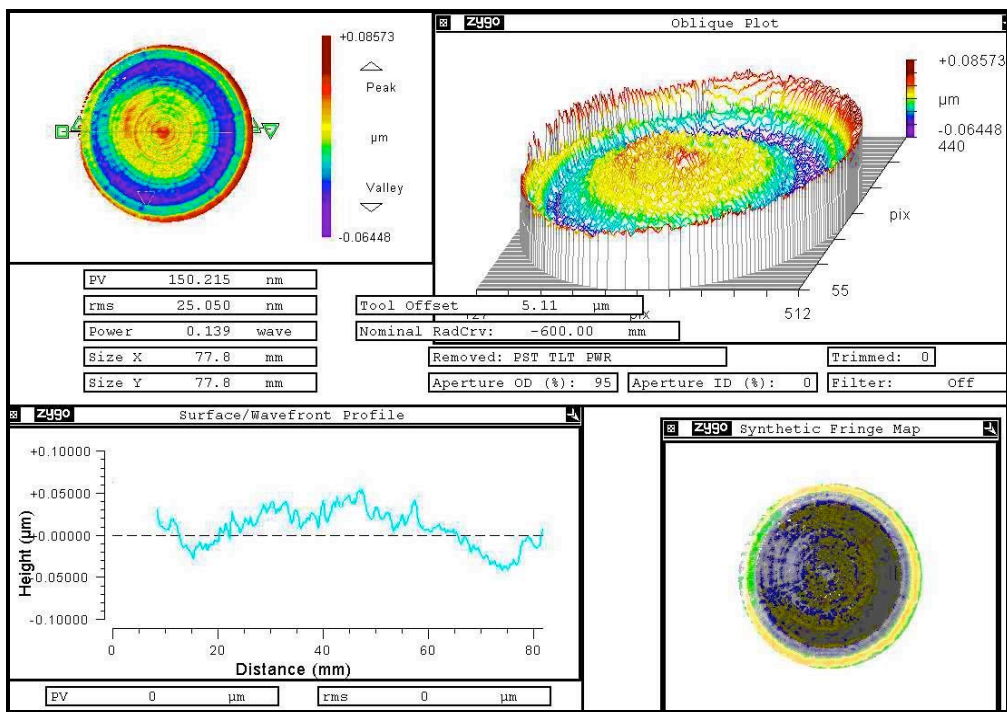


**Figure 3-14:** Sphere measurement with power removed. PV error was 150 nm or  $\lambda/4$ .

### 3.5 CONCLUSIONS

A number of diamond turned 100 mm diameter flats were machined on the ASG- 2500. These surfaces have PV form fidelity below  $\lambda/3$  (211 nm) often falling below the  $\lambda/4$  (158 nm) threshold. All linear traces of the surface fall below  $\lambda/4$  and often fall below  $\lambda/5$  (127 nm). The NRS component seen in these flats is the difference between the form error and the trace error, which was measured between 30 and 80 nm. This places these surfaces slightly below and above the Rayleigh limit for optics that have diffraction-limited performance, which means they would be suitable for use in diamond turned optical systems designed for the visible spectrum. For imaging at the small wavelength

end of the visible spectrum (400 nm), the performance would be slightly less than diffraction limited as  $\lambda/4$  becomes 100 nm.

Automatic error correction is imperative for fabrication of high-fidelity mirrors. Squareness error between the spindle centerline and X-axis are the dominating error in optical flat fabrication with the ASG-2500. The squareness error was found experimentally and it was corrected ASG-2500 automatic compensation routine. Lookup tables were verified to correct for the straightness errors of each axis.

The consistency in the results above was not achieved until thermal influences were observed. “Warm up” of the spindle must be complete before attempting to diamond turn an optical surface which is similar to results from Moorefield [7] discussed in Section 3.2.3. Also, the aspect ratio of the part gave it high sensitivity to temperature changes such that a 75 mm long part made from 6061-T6 aluminum alloy will expand 1770 nm/ $^{\circ}$ C. It is absolutely necessary to utilize thermally isolating gloves, have minimal contact with the work piece, confine it to a tightly controlled environment and constantly monitor lab temperature for changes.

Using the automatic error correction that yielded high-fidelity flats allowed the fabrication of a high-fidelity large-aperture sphere. The aperture diameter was 100 mm and the spherical radius was 275 mm. The form error measured in a trace across the sphere was  $\lambda/4$  (158 nm). The measured sphere radius error was less than 6  $\mu$ m, which

was observed as the repeatability of the length measuring laser interferometer mounted to the GPI translating stage.

## 4 SURFACE ROUGHNESS IN DIAMOND TURNING

### 4.1 INTRODUCTION

Theoretical RMS roughness using the parabolic approximation for a round tool edge is calculated with the equation:

$$RMS = \frac{f^2}{26.6R_t} \quad (4-1)$$

where feed rate is  $f$  ( $\mu\text{m}/\text{rev}$ ) and tool nose radius is  $R_t$  ( $\mu\text{m}$ ). The actual RMS surface roughness of the optical surfaces in the two-mirror telescope described in Section 2 was approximately 20x the theoretical RMS and there was little indication of tool nose radius or the specified cross-feed in either surface. With the small feed rate (2-4  $\mu\text{m}/\text{rev}$ ) and large nose radius tool (3.135 mm) discussed in Section 2, the theoretical RMS surface finish of the primary is 0.19 nm while the actual was 5 nm and the theoretical RMS of the secondary was 0.05 nm while the actual was 4 nm [1]. Research completed previously at the PEC showed better surface finishes were achievable with the same equipment used to fabricate the two-mirror telescope [12, 13]. It also showed that both the approximated parabolic and the true circular cusp height were most accurate at large feed rates where machine vibration magnitude was small compared to cusp height.

The objectives of this Section were to machine in a regime (larger feeds than used for telescope) where the first-order geometric model in Equation 4-1 accurately predicted

surface finish and, based on those results, to develop a surface finish model with machine vibration that predicts roughness at small feed rates (similar feeds used for telescope). Dithering of the tool in the cross-feed direction was also studied as a method to reduce diffraction effects caused by diamond turned grooves by randomizing the groove spacing without causing significant increases to surface roughness.

## 4.2 SURFACE FINISH EXPERIMENTS IN FIRST-ORDER REGIME WITH VARIATION OF SECOND-ORDER FACTORS

The research done at the PEC by Drescher [12] and Arcona [13] was used as a baseline for repeated experiments in the regime where the parabolic approximation accurately predicts roughness with first-order variables of cusp spacing and tool radius. Surface speed was tested to verify that it does not influence surface finish by cutting at different workpiece radii with the same cross-feed rate. To ensure that the parabolic approximation would predict finish, the initial tests were conducted at a relatively high feed rate and, to explore the lower limit of the prediction accuracy, feed rate for subsequent tests was incrementally decreased. Each test in this section incorporated several cut depths to examine the effects of depth of cut on roughness. A tool servo was used to quickly change these depths such that a large portion of the cutting window remained in the surface profile for a complete revolution.

Quick depth changes provided the ability to observe a large section of the tool edge as it advanced thought the work piece and its relationship to the previous passes. An example of the quick depth change is seen in Figure 4-1 where the lower set of grooves were cut 1

$\mu\text{m}$  deeper than the upper grooves. The cross feed direction in this profile is from left to right and is the same for all other surface profiles seen in this chapter. It shows a large portion of the cutting window, so interactions between the tool edge and the material that was removed could be examined. This is interesting because the leading edge of the tool has a much larger depth of cut than the trailing edge (the trailing edge is responsible for the residual grooves that determine surface roughness). Test measurements were then easily matched to theoretical tool paths for analysis of desired and undesired cross-feed features. In the event that the curvature of the cusps did not match the tool radius, the large section of the edge could have been used to verify the radius or align the cusps with a theoretical profile. Also, the large portion of the tool edge remaining provided the chance to observe the tool-workpiece interactions at larger cutting depths than normally seen in a surface finish measurement. Here, up-feed feature could be observed over a large cutting window.

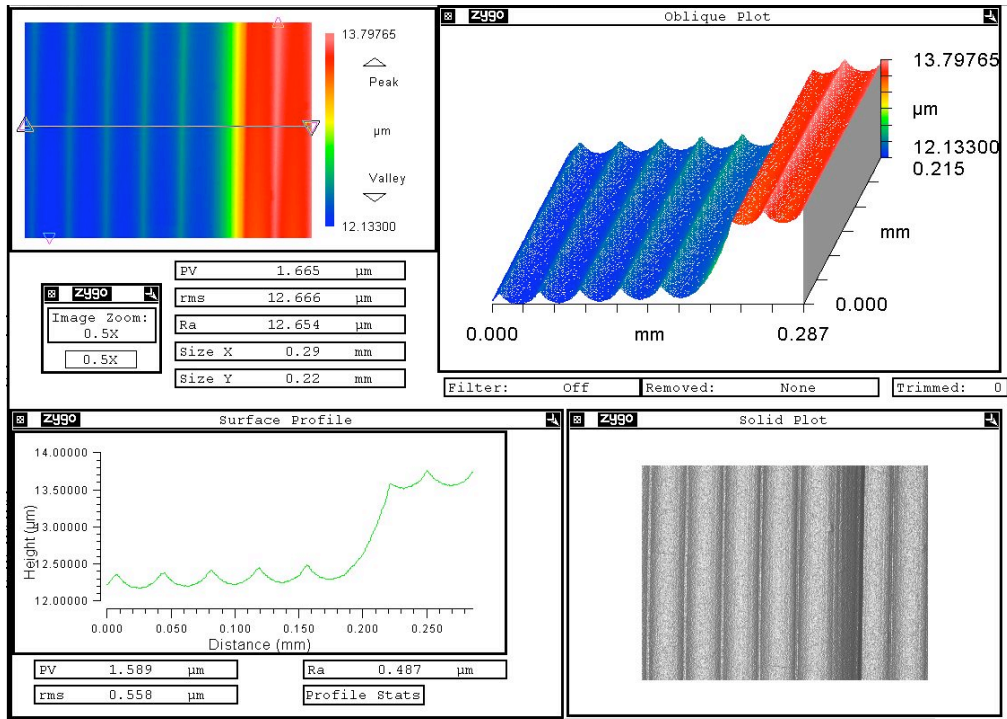


**Figure 4-1:** Transition from 2  $\mu\text{m}$  cutting depth to 1  $\mu\text{m}$  at 37.7  $\mu\text{m}/\text{rev}$  feed rate, and 1.1 m/s surface speed in electroplated copper with a 0.750 mm radius tool. Cross feed direction is from left to right in this and all other surface profiles in this Section.

#### 4.2.1 Surface Finish Variables

The geometry of a diamond tool has two main variables that influence surface roughness: nose radius and edge radius. The nose radius of a diamond tool leaves a circular cusp in the workpiece that has a width equal to the cross-feed. As the cross-feed is linearly reduced, cusp spacing becomes proportionally narrower; however, the RMS cusp height decreases by the square – see Equation 4-1. This is the basis for the first-order model discussed in Equation 2-2 where large tool radii and fine cross-feeds should produce a

surface contour with a very small PV roughness. For the tests in this section (Section 4.2), a nose radius of 750  $\mu\text{m}$  was used such that the cusps were easily identified in the surface profiles at both coarse and fine cross-feeds. For a given feed rate, a smaller nose radius tool will produce a rougher surface with larger cusp heights. The cusp features then will be visible for low slide velocities ( $\sim 2$  mm/min with a spindle speed of  $\sim 500$  rpm) like those used for the two-mirror telescope.

The edge radius of the diamond tool is a measure of its “sharpness.” As the edge wears, the radius becomes larger and the tool becomes “duller”. Others [13] have shown that cutting and thrust forces increase with edge wear, as does the minimum chip thickness as seen in Figure 4-2. Because the chip thickness cannot be zero, a certain amount of material is elastically deformed into the workpiece as the tool passes. Once the tool has left the area, the deformed material (also called spanzipfel) springs back leaving a ridge at the trailing edge where the cutting depth should theoretically be zero. The result is a portion of the residual cusp rises above the expected round cusp shape thereby increasing the surface roughness. The influence of a minimum chip was undesired in these tests so the 750  $\mu\text{m}$  tool used was sharpened in anticipation of this experiment to minimize the presence of material spring back (spanzipfel).

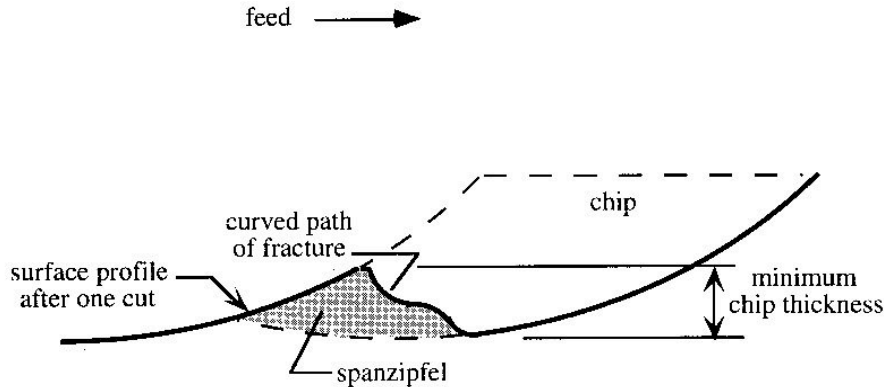


**Figure 4-2:** Second-order effect of minimum chip thickness caused by a worn tool with a large edge radius [13].

Electroplated copper made an ideal material choice for this experiment because of its high microhardness, small grain structure ( $\sim 10$  nm), lack of ductility and lack of second-phase particulates. The microhardness of electroplated copper has been shown near the pure copper limit [20]. As seen by the diamond tool, this material is homogenous. When using a tool with a sharp edge, surface profiles produced in this material have sharp cusp corners and smooth up-feed grooves.

Depth of cut directly affects both cutting and thrust forces by changing the area of the rake face that is removing material [13]. The area of the rake face used is enclosed by the uncut surface, the radius left by the previous pass, and the edge of the tool that is cutting as seen in Figure 4-3. Depth of cut was varied between sets of machining passes in this section with a tool servo. The servo quickly retracted the tool from the workpiece so a groove at the current (deeper) depth was left for almost an entire revolution of the

workpiece. The section of the tool edge that is higher than the cusps seen in Figure 4-3 could then be matched to the residual cusps or examined independently to check for other features.

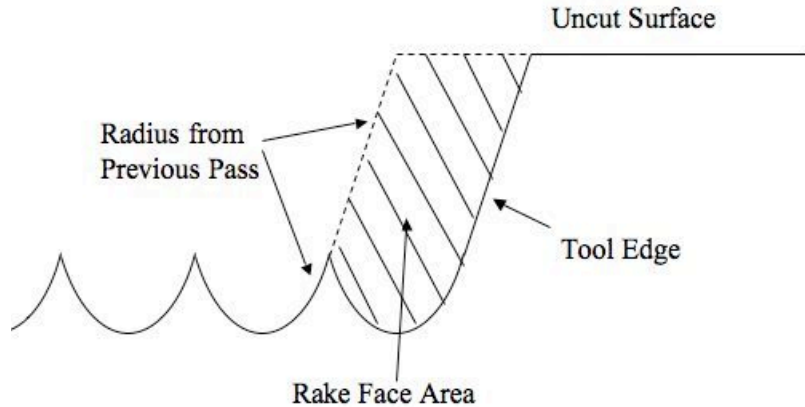


**Figure 4-3:** Rake face area enclosed by the previous pass, tool edge and uncut surface.

The ratio of length to height in this drawing was set to resemble Figure 4-1 at approximately 150:1.

In lathe-based rotational machining, the surface speed of the work piece relative to the tool changes linearly as the radius of the part changes. The changing surface speed dictates that material removal rate and cutting speed change linearly over the duration of a cut. Others have shown that the effect of surface speed is insignificant at the cutting velocities used in this experiment [12]. The tests were performed at several radii on the workpiece to verify these results.

Cross-feed rate of the diamond tool through the workpiece sets the cusp spacing and, combined with the tool nose radius, will determine the cusp height. The largest cross-feed was set so a coarse surface with relatively large cusps was produced. This coarse surface presented the opportunity to match large cusps to a theoretical tool edge and align them with the groove wall remaining after the depth of cut was quickly reduced with the FTS. Since the goal was to machine in a regime where the parabolic approximation can predict the roughness of a surface profile, the smallest cross-feed was set such that the profile exhibited regularly spaced cusps at that cross-feed.

#### *4.2.2 Experimental Setup and Part Planning*

A fast tool servo (FTS) was mounted to the ASG-2500 diamond turning machine (DTM) as seen in Figure 4-4 to facilitate instant depth of cut changes. The FTS axis of motion was orthogonal to both the spindle face and the experimental surface. The FTS was mounted on the micro-height adjuster for adjustability in the vertical (Y-axis) direction. This allows precise ( $< 1 \mu\text{m}$ ) positioning of the diamond tool relative to the spindle centerline. To cool and lubricate the material removal process, petroleum oil cutting fluid (Mobilmet Omicron®) was sprayed onto the tool. The cutting fluid was manually sprayed onto the tool (from directly above with a squirt bottle).

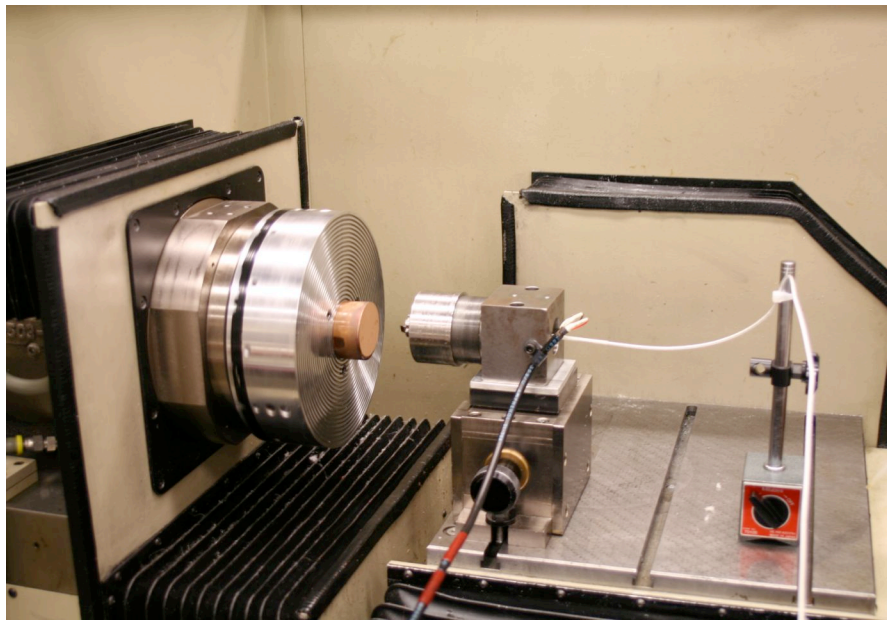


**Figure 4-4:** Diamond Turning Machine with FTS for instant depth of cut change

The servo was designed and built at the PEC and a great deal of research has been dedicated to measuring the dynamic response, developing closed loop control schemes, and finding novel applications of this auxiliary axis. It consists of a threaded housing that sets a preload on a tubular piezoelectric ceramic (Lead Zirconate Titanate or PZT) stack through annular flexures. A capacitance (cap) gage is situated inside the PZT stack and measures the position of the back face of the tool holder. Positive input voltages to the PZT result in a displacement of the tool holder toward the part, which is opposite the flexure force direction. The cap gage output provides position feedback for closed loop control of the tool position (depth of cut).

#### 4.2.2.1 Fast Tool Servo Setup

A 40 mm long PZT stack was used in the FTS that afforded a servo range of 40  $\mu\text{m}$ . A cap gage with a 20  $\mu\text{m}$  range provided position feedback for closed loop control of tool position to eliminate errors such as PZT hysteresis effects. The difference in range between the PZT and the cap gage was accounted for by mechanically setting the gage to null with the servo extended half of its range or 20  $\mu\text{m}$ . This practice keeps the PZT in the center of its mechanical and electrical range during closed loop operation.

The open loop position response of the FTS with the 40 mm PZT stack was measured. Because the PZT stacks have a crystal structure, tensile stresses would cause cracks. The flexure is thereby used to mechanically bias the stack such that it is always in compression. The need for compressive bias means the electrical input to the 40 mm stack ranges from 0 to 1000 volts for corresponding displacements of 0 to 40  $\mu\text{m}$ . The tests performed were limited to an amplifier input range 2.5 – 8.5 volts (amplifier voltage gain is 100x) because the cap gage range is only 20  $\mu\text{m}$  (5 V input = 500 V output = 20  $\mu\text{m}$  servo displacement = 0  $\mu\text{m}$  cap gage reading). The amplifier has an output channel that is divided by a factor of 100 to verify the command signal. For redundancy, a Federal Gage LVDT with involute tip was used to measure the step displacements of the FTS tool holder during setup.

The open loop position data was collected and a plot of the results are in Figure 4-5. Output voltage of the amplifier increased equally with input voltage. The cap gage data

was fitted with a linear regression and the slope of -4.004  $\mu\text{m}/\text{volt}$  corresponds with the expected displacement of 4  $\mu\text{m}/\text{volt}$  of amplifier input. The slope of the regression is negative because the capacitance gage measures the back of the tool holder and a positive motion of the tool is away from the cap gage. For plotting purposes, the sign of the slope was switched. Although the slope of the Federal Gage was smaller (calibration of the gage for this test was not critical), it verified tool holder motion, positive displacement direction and output of the capacitance gage. This test was performed moving in only one direction to avoid the hysteresis effects commonly found in a PZT. Repetition of this test produced the same result.

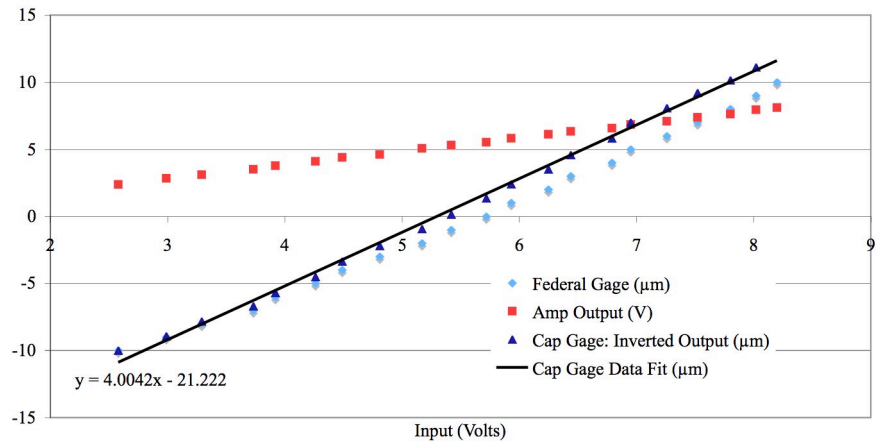


**Figure 4-5:** Open Loop Response of FTS with 40 mm PZT Stack

Because the FTS is position command with position feedback and has a mechanical and electrical bias, a closed loop controller with low proportional gain ( $K_P$ ) and high integral ( $K_I$ ) gain was used [21]. The high integral gain facilitates good command following and

position holding [21]. Since the servo axis moves in the direction that surface finish is most sensitive, position holding is critical [14].

DTM control was performed by the control system discussed in Section 2.5 while FTS control was through a dSPACE DSP card. The dSPACE was programmed with MATLAB and Simulink. Software by dSPACE called Control Desk was used as the controller interface. The gains in the controller were adjusted to provide stable closed loop response to a step command at 10  $\mu\text{m}$  ( $K_P = 0.1$ ,  $K_I = 2000$ ). A surface profile showing one of the commanded steps (1  $\mu\text{m}$ ) is in Figure 4-6. The measured length of the step is 75  $\mu\text{m}$  and with a spindle speed of 530 rpm at a circumference of 125 mm, the rise time is calculated as 5.3 milliseconds. This was more than adequate to make instant cutting depth changes because the transition length was less than 1/1000 of a revolution.

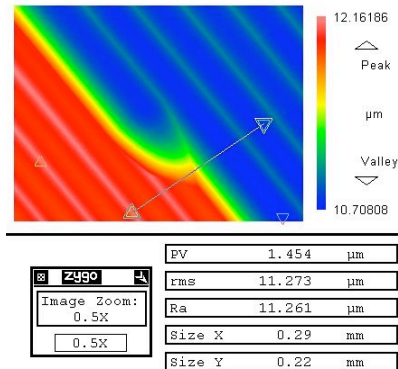


**Figure 4-6:** 1  $\mu\text{m}$  cutting depth change command at a circumference of 125mm. Rise time is 5.3 ms.

#### 4.2.2.2 Tool Path

The DTM plunged the tool into the part and then moved the tool across the face of the workpiece (perpendicular to the spindle face) at a constant velocity while the FTS instantly stepped the tool to a new, shallower cutting depth. The plunge depth was 10  $\mu\text{m}$  into the work piece at an outer radius and the tool was moved towards the spindle centerline to an inner radius. The FTS moved the tool to a shallower depth after 10 grooves (or 10 spindle revolutions) were cut at each depth. The step sizes were 5  $\mu\text{m}$ , 3  $\mu\text{m}$ , 1  $\mu\text{m}$  and 3  $\mu\text{m}$ . Combining the DTM plunge depth with the FTS step sizes yielded cutting depths of 10  $\mu\text{m}$ , 5  $\mu\text{m}$ , 2  $\mu\text{m}$ , and 1  $\mu\text{m}$ . The last 3  $\mu\text{m}$  step removed the tool from the work piece and held it 2  $\mu\text{m}$  above the original surface until the DTM fully retracted from the initial plunge depth. A continuous profile that displays each cutting depth and the original surface is seen in Figure 4-7.

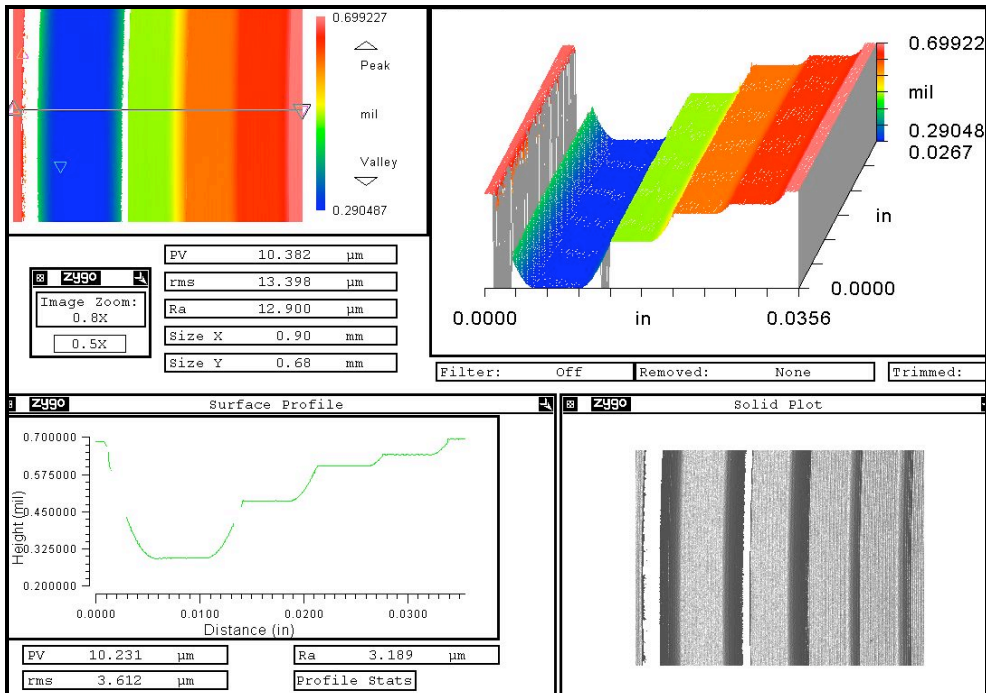


**Figure 4-7:** Example of tool path with instant depth of cut changes. The original surface is seen at far left and right of the profile. The deepest cut is on the left and was performed first. The cutting depths were 10  $\mu\text{m}$ , 5  $\mu\text{m}$ , 2  $\mu\text{m}$  and 1  $\mu\text{m}$ .

#### 4.2.2.3 Machining Plan

A total of seven continuous cutting passes were performed. Table 4-1 lists beginning workpiece radius, ending workpiece radius, cross-feed rate, theoretical and actual PV and RMS for each test. The spindle speed was 530 rpm. Tests 1, 2, and 3 had identical feed rates and spacing, but were performed at different radii on the work-piece to test the effects of surface speed, which varied by a factor of 10. The change in radius from Test 1 to 2 results in a 70% decrease in cutting speed and 1 to 3 results in a 90% decrease.

Because Test 3 is near the workpiece center (2 mm - 0.1 mm) the final revolution for this test is 90% slower than the first revolution. Tests 4-7 were each performed at gradually lowered feed rates and tested for any combined effect from cutting depth and feed rate. They were at intermediate radii on the same workpiece and had a spacing of 2 mm between the starting radii. The changes in feed rate between Tests 4 and 7 were determined by reductions in the theoretical PV roughness from the first three tests. Order of magnitude decreases in surface finish were initially desired but the final reductions were 1/2, 1/5, 1/10, and 1/50 to allow for intermediate roughnesses and to ensure that cusp features with spacing that matched the lowest feed rate were still identifiable for the slowest test (7).

**Table 4-1:** Layout of tests on copper workpiece.

| Test | Start Radius (mm) | End Radius (mm) | Feed Rate ( $\mu\text{m}/\text{rev}$ ) | Surf Vel (m/s) | PV Theory (nm) | PV Actual (nm) |         | RMS Theory (nm) | RMS Actual (nm) |         |
|------|-------------------|-----------------|--|----------------|----------------|----------------|---------|-----------------|-----------------|---------|
|      |                   |                 |  |                |                | Mean           | St. Dev |                 | Mean            | St. Dev |
| 1    | 20                | 18.1            | 37.7                                   | 1.1            | 231            | 289            | 12.8    | 69.1            | 73.0            | 3.55    |
| 2    | 6                 | 4.1             | 37.7                                   | 0.3            | 231            | 284            | 17.0    | 69.1            | 69.3            | 2.16    |
| 3    | 2                 | 0.1             | 37.7                                   | 0.1            | 231            | 267            | 20.4    | 69.1            | 69.5            | 3.00    |
| 4    | 17                | 15.67           | 26.7                                   | 0.9            | 115            | 145            | 14.6    | 34.5            | 38.3            | 1.71    |
| 5    | 15                | 14.07           | 16.86                                  | 0.8            | 46.2           | 79.0           | 3.92    | 13.8            | 17.3            | 0.50    |
| 6    | 13                | 12.26           | 11.9                                   | 0.7            | 23.1           | 59.7           | 7.89    | 6.9             | 13.0            | 1.83    |
| 7    | 11                | 10.53           | 5.33                                   | 0.6            | 4.6            | 37.0           | 1.41    | 1.4             | 7.25            | 0.50    |

#### 4.2.3 Surface Speed Effects

The results of Test 1, 2, and 3 were measured to assess the effect of cutting speed on surface finish. A Zygo NewView 5000 Scanning White Light Interferometer produced

3D profiles of the machined surface and was able to easily resolve the diamond tool grooves. A sample measurement of the surface for Test 1 at 5  $\mu\text{m}$  cut depth is seen in Figure 4-8. From this 3D data, a 2D trace was produced in the cross feed direction.

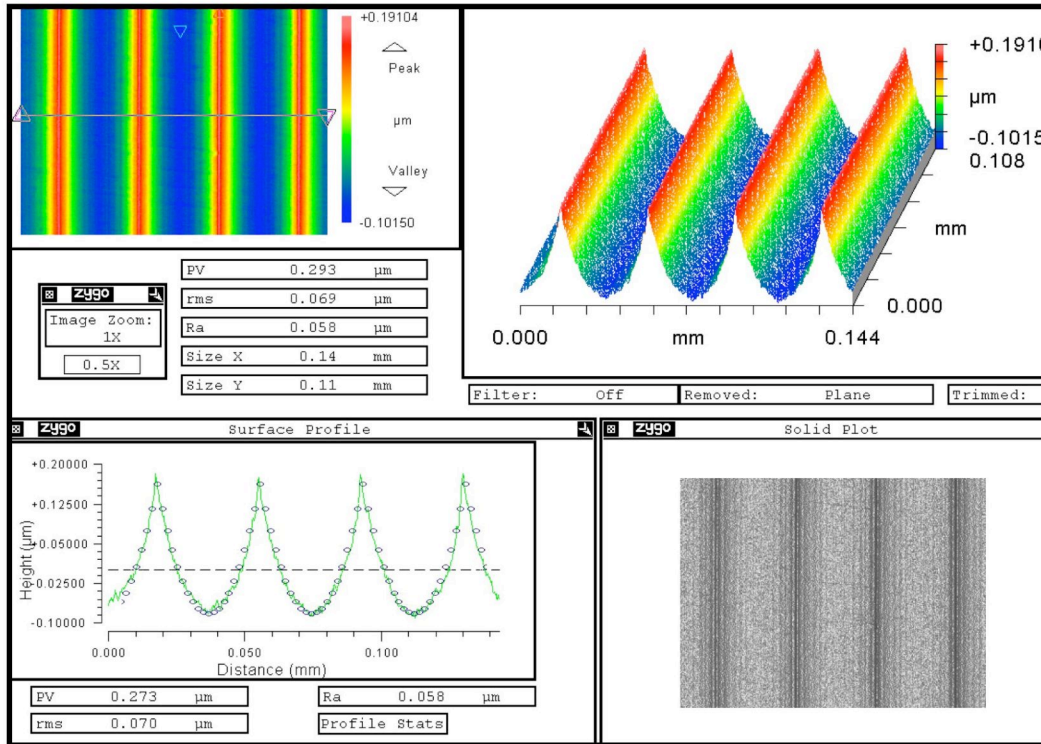


**Figure 4-8:** Sample New View Scan. Test 1 at 5  $\mu\text{m}$  DOC. Circles overlaid onto the surface profile represent the theoretical cusps.

Roughness measurements from Tests 1, 2 and 3 (all depths of cut included) were compiled into Figure 4-9 for evaluation of surface speed effects. Surface speeds of 0.1, 0.3 and 1.1 m/s at 530 RPM correspond to respective workpiece radii of 2, 6 and 20 mm. The PV and RMS roughness for each of the three surface speeds have similar means and

variation. For each surface speed, there were 4 cutting depths, thus 4 data points at each speed. The relationship between cutting depth and surface finish was examined with respect to surface speed but no trend was seen. The slowest speed has a couple of points with lower PV than the other two speeds, but by less than 20 nm. Both actual PV and RMS have higher means than the theoretical values and the increases appear consistent across the different speeds. This suggests that roughness is independent of surface speed for range typically seen in diamond turning operations, which is consistent with conclusions made in the previous research [12, 13].

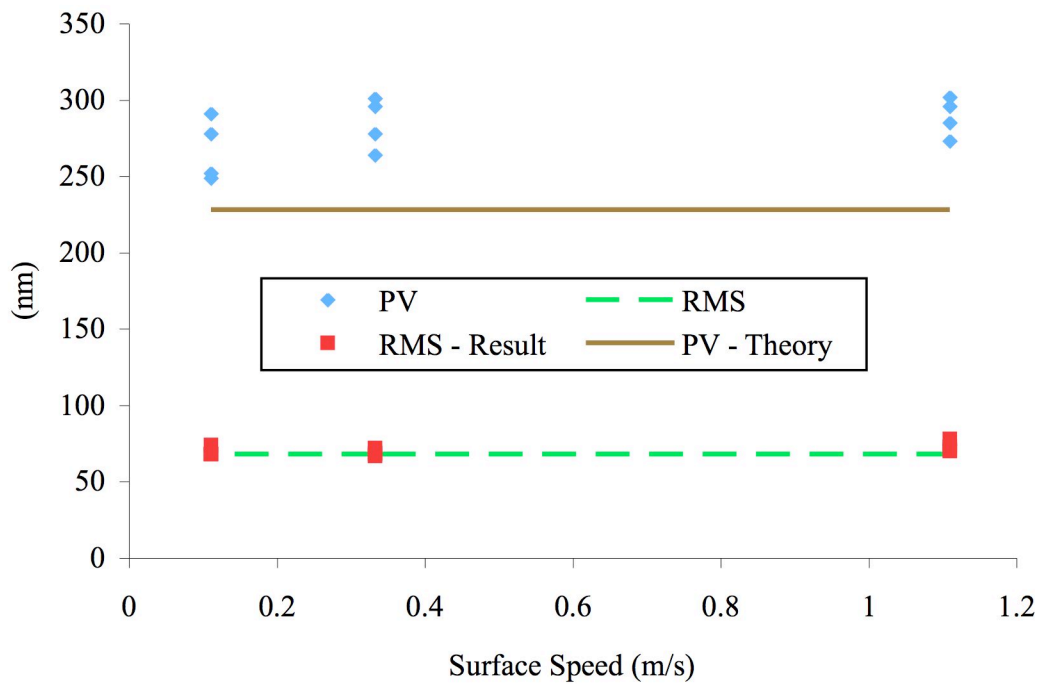


**Figure 4-9:** Actual and theoretical surface roughness vs. surface speed for Tests 1-3

(1.1, 0.3, 0.1 m/s, respectively).  $f = 37.7 \mu\text{m/rev}$ .

#### *4.2.4 Depth of Cut Effect*

Measurements of Tests 1, 2, and 3 show there is little in this experiment indicating that roughness is a function of cutting depth. Because Tests 1, 2, and 3 showed no trend when compared by surface speed (as calculated with workpiece radius and spindle speed), the data from these tests was grouped together for the depth of cut plot at 37.7  $\mu\text{m}/\text{rev}$  feed rate in Figure 4-10. For comparison, horizontal lines in the plot show the theoretical PV and RMS surface roughness. The data spread is fairly consistent for each cut depth and there is little variation from depth to depth. The spread in PV roughnesses is about 60 nm and, when grouping the data together, the mean is approximately 50 nm higher than theoretical PV. When comparing the PV and RMS theoretical values to the actual data, the actual data are equal to or higher (similar to the surface speed comparisons).

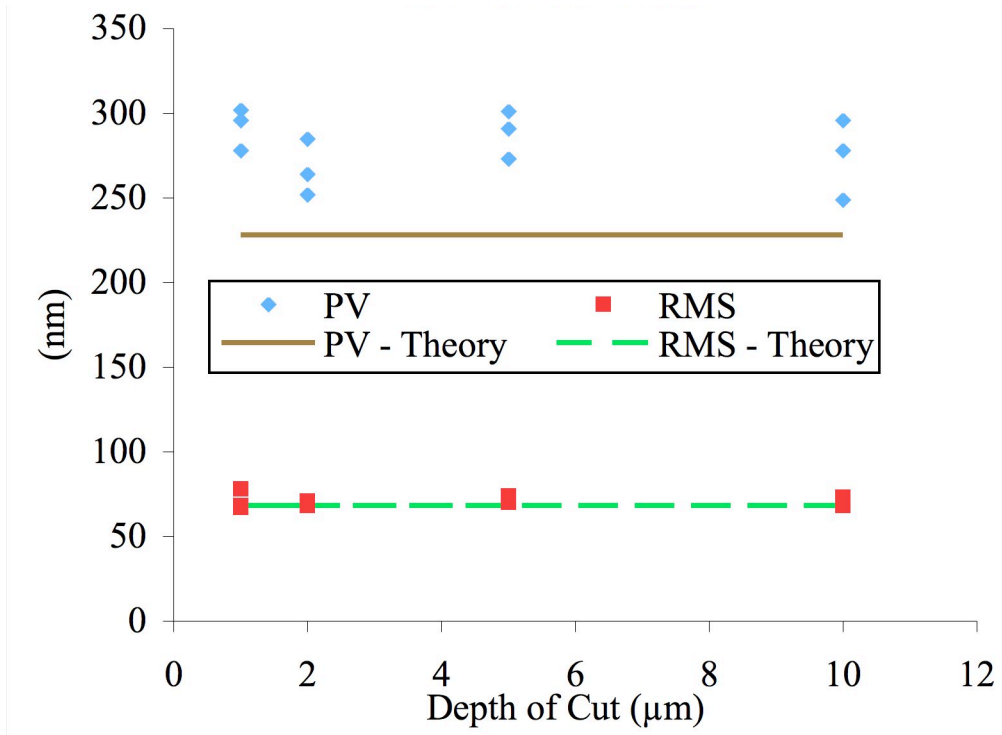


**Figure 4-10:** Actual and theoretical surface roughness vs. depth of cut for Tests 1-3.

Three points at each cutting depth from Tests 1-3.  $f = 37.7 \mu\text{m/rev}$ .

Tests 4-7 showed similar trends to Tests 1-3: a generally uniform PV and RMS when comparing different depth of cuts. The results are presented in Table 4-1. For each feed rate, the actual PV and RMS are consistently higher than the theoretical, although the difference is much less of a factor in the higher feed rate tests than in the lower. The results reveal that the actual PV is 30 nm to 50 nm larger than the theoretical for all feed rates. This suggests that another variable (second order effect such as machine vibration or tool sharpness) has an influence on PV and RMS roughness that is independent of feed rate.

#### 4.2.5 Cross-Feed Rate Effect

Measurements from all experiments in Table 4-1 were complied into a single data set to compare feed rate affects on surface roughness. Plots of this data with respect to cross-feed rate are found in Figure 4-11 for PV roughness and Figure 4-12 for RMS roughness. Each plot has a line to represent the theoretical value and a series of points at discrete cross-feeds that represent different cutting depths and workpiece radii for each data point.

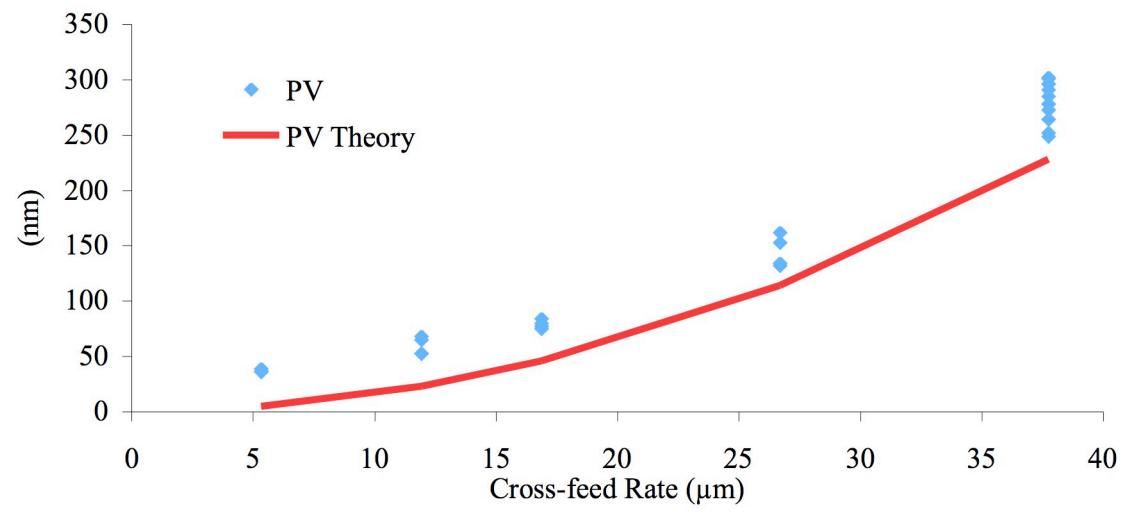


**Figure 4-11:** Actual and theoretical PV surface roughness vs. feed rate for Tests 1-7 in Table 4-1.

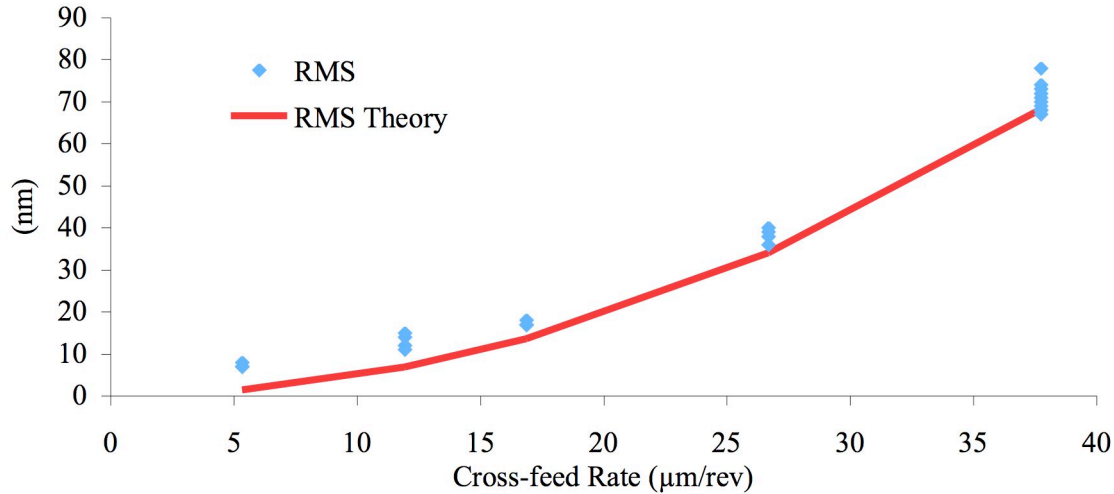


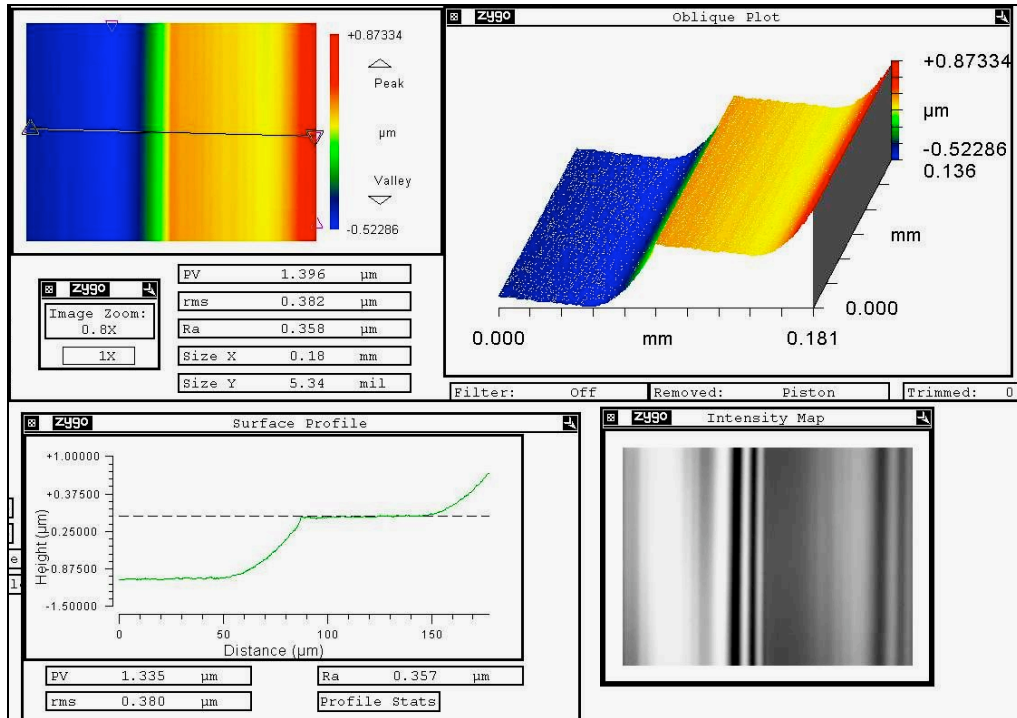
**Figure 4-12:** Actual and theoretical RMS surface roughness vs. feed rate for Tests 1-7 in Table 4-1.

The PV and RMS roughness data both demonstrate trends that follow the theoretical predictions. The mean of the PV roughness measurements in Figure 4-11 were consistently 30 to 50  $\mu\text{m}$  larger than theoretical value, again implying that this measurement is affected by an independent variable (such as machine vibration or tool sharpness) that remains constant with respect to feed rate. The RMS roughness appears consistently larger as well but only by 5 nm or so.

The largest cross-feed (37.7  $\mu\text{m}$ ) has three times the number of data points than the other cross-feeds. The mean of the 37.7  $\mu\text{m}$  cross feed appears higher by the same amount as the mean of the other cross-feeds. In the RMS results seen in Figure 4-12, the actual values approach the theoretical and one data point falls 1 nm (1%) below theoretical.

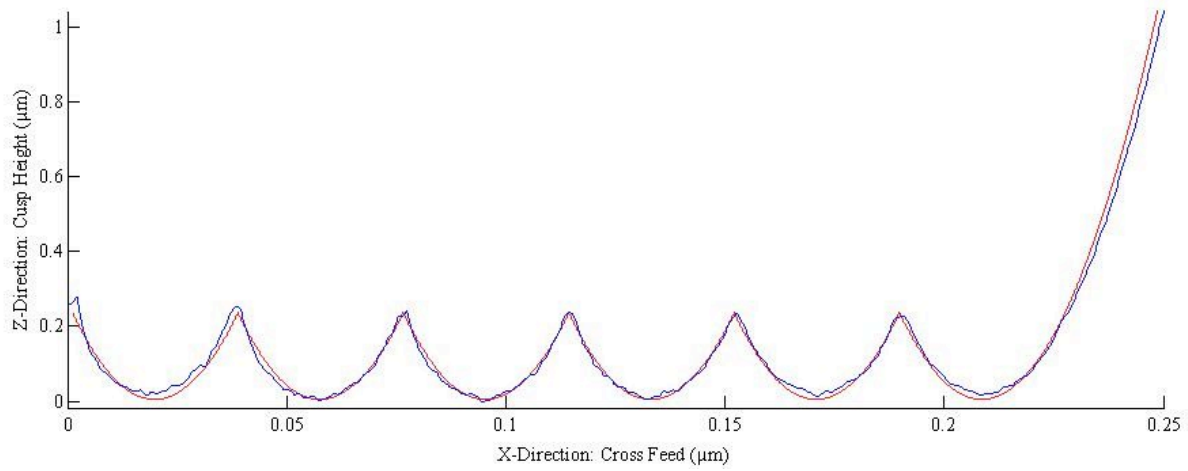
#### 4.2.6 Groove Comparison with Instant Depth of Cut Change

Figure 4-1 in Section 4.2 showed an example of an instant depth change while machining at a large feed rate ( $37.7 \mu\text{m/rev}$ ) and, for contrast, Figure 4-17 shows the same depth change ( $1 \mu\text{m}$ ) while machining at the lowest feed rate in the test ( $5.33 \mu\text{m/rev}$ ). At the low feed rate, the cusp features are barely discernable when compared to the  $1 \mu\text{m}$  cutting depth change, which is very different than Figure 4-1 where cusp features are readily distinguishable at the high feed rate ( $37.7 \mu\text{m/rev}$ ).



**Figure 4-13:**  $1 \mu\text{m}$  depth of Cut change for  $5.33 \mu\text{m/rev}$  feed rate.

The large radius left by the step change was compared to the remaining cusps. Figure 4-14 shows a surface profile of several cusps leading up to a cutting depth change and the theoretical tool shape at the prescribed feed rate. When comparing features at large cross feeds, it is difficult to discern secondary effects. Figure 4-15 shows a comparable plot at a feed rate of 5.33  $\mu\text{m}/\text{rev}$  where it is more difficult to match the theoretical cusp spacing and the step profile to the actual surface contour. At this small cross feed, the contribution to roughness has less to do with the parabolic approximation of the tool and more to do with secondary effects. These secondary effects (discussed next) are the cause of the increase to PV and RMS roughness as seen in the roughness measurements of Table 4-1.



**Figure 4-14:** Surface profile from a  $37.7 \mu\text{m}/\text{rev}$  feed rate (Test 1) showing several cusps with the last groove cut at that depth before the FTS stepped the tool up compared to the theoretical profile (smooth line).

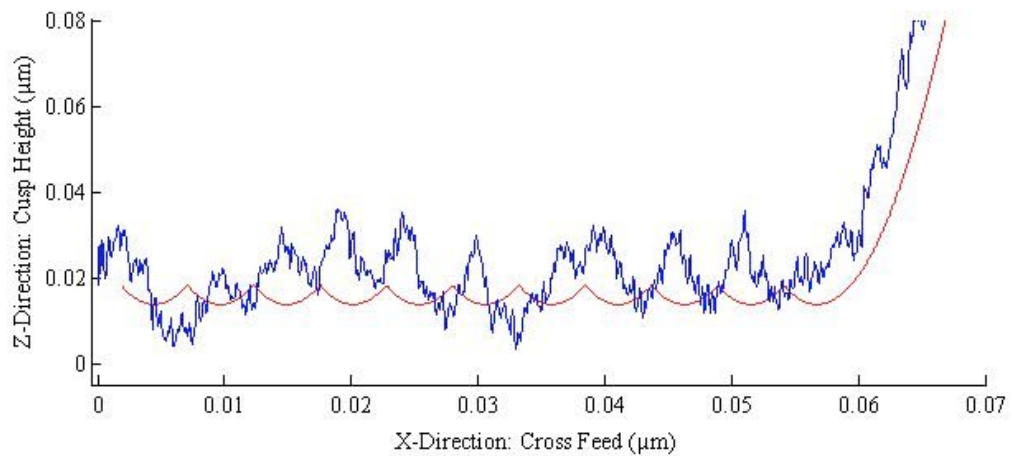


**Figure 4-15:** Surface profile from a  $5.33 \mu\text{m}/\text{rev}$  feed rate (Test 4D) showing several cusps and the last groove cut at that depth before the FTS stepped the tool up compared to the theoretical profile (smooth line). This graph has 10X the vertical magnification of Figure 4-14.

**Summary:** Two separate mechanisms caused larger surface roughness than the parabolic approximation (PV and RMS) of a round nose tool predicted. One was minimum chip thickness and the second is spindle vibration. The minimum chip thickness is a function of tool edge radius or sharpness. All tools have some edge radius after sharpening and, as they wear, this radius becomes larger. According to Arcona [13], even a freshly sharpened tool (<50 nm edge radius) will cause elastic deformation as the tool moves through the workpiece. The elastic rebound was approximately equal to the edge radius when cutting with a sharp tool round nose tool in electroplated copper. With elastic rebound present in the cutting conditions, some minimum chip thickness was seen in the surface profile. By placing a theoretical tool path against the trace, the uncut material was observed and can be seen as a small hump at the intersection of adjacent tool passes in Figure 4-16 (Test 1, 37.7  $\mu\text{m}/\text{rev}$ , 5  $\mu\text{m}$  depth of cut). Also, Figure 4-17 shows Test 6 (11.9  $\mu\text{m}/\text{rev}$ , 5  $\mu\text{m}$  depth of cut) where the minimum chip thickness causes the cusp height to appear much larger than expected with a round nose tool at that feed rate (predicted with the parabolic approximation). The minimum chip is best seen in the first two cusps (left side) where the theoretical profile is closely aligned to the leading edge of the theoretical tool, but is separated from the trailing edge of the theoretical tool (again, feed is from left to right). The illustration in Figure 4-2 demonstrates this elastic rebound of the minimum chip.

The second mechanism is asynchronous spindle vibration and is best observed in Figure 4-17 because of the smaller cusp heights than in Figure 4-16. Each pass occurs at slightly

different depth where the range of depths closely matches the previously reported vibration of the Z-axis and spindle on the ASG2500 where the full amplitude was 30 nm [12].

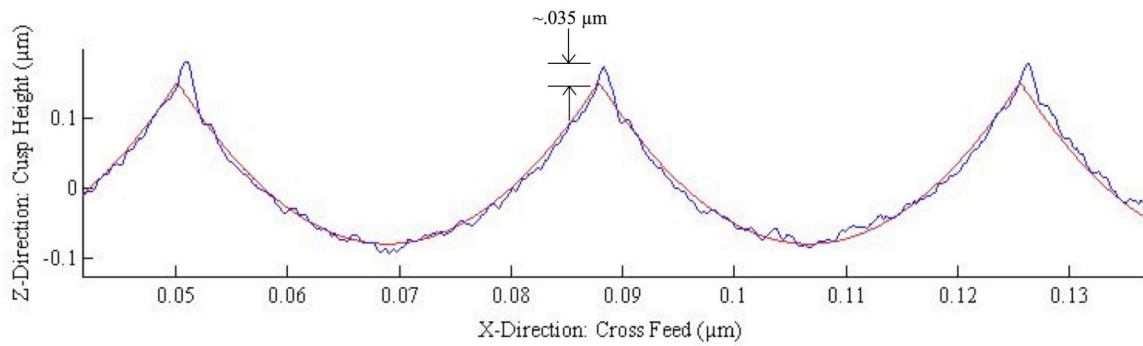


**Figure 4-16:** 37.7  $\mu\text{m}/\text{rev}$  feed rate (Test 1) zoomed to show only a few cusps and compared to theoretical (smooth line). Feed direction left to right.

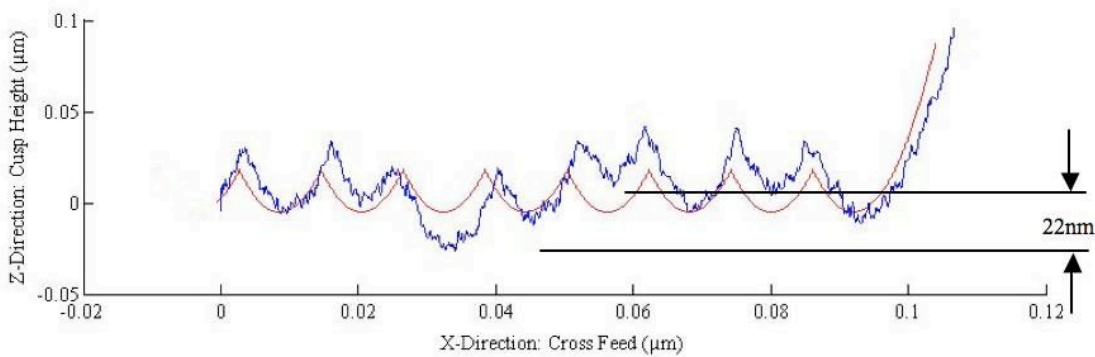


**Figure 4-17:** 11.9  $\mu\text{m}/\text{rev}$  feed rate (Test 4C) with cutting depth change compared to theoretical profile (smooth line). Asynchronous vibration caused valley-to-valley variation of 22 nm. Feed direction left to right.

#### 4.2.7 Features in the Cutting Direction

Features were found when examining the circumferential path of the cut in the last groove cut before the FTS retracted the tool to a new cutting depth. Figure 4-18 gives the orientation of the measurement in Figure 4-19, which shows the top edge of the last groove in Test 3 at 10  $\mu\text{m}$  cutting depth (37.7  $\mu\text{m}/\text{rev}$ , 2 mm starting workpiece radius). Because the next cutting depth was 5  $\mu\text{m}$ , the actual cutting depth when the tool passes through the measured portion of the groove was 5  $\mu\text{m}$ . This groove was the 10<sup>th</sup> pass at 37.7  $\mu\text{m}/\text{rev}$  and given the groove height of 5  $\mu\text{m}$  with a 750  $\mu\text{m}$  tool nose radius, the workpiece radius of the cusp bottom was 1.535 mm. At 530 rpm, the surface speed was 5100 mm/min or 0.085 m/s. The measurement shows features with a spacing of 1.5  $\mu\text{m}$ , which can be seen in *xPos* of the *Autocovariance Plot* menu in Figure 4-19.

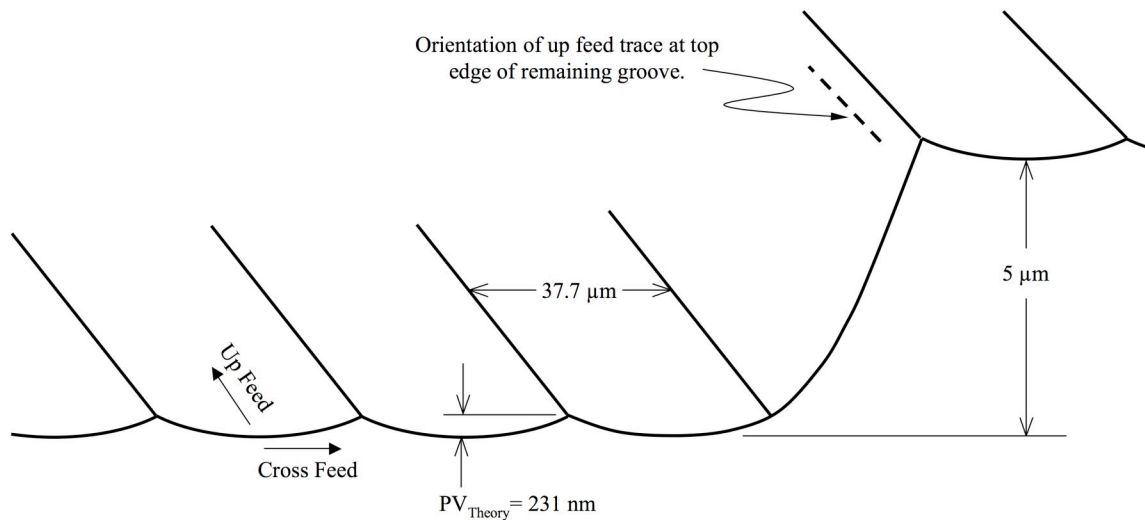


**Figure 4-18:** Orientation of up feed trace in Figure 4-19.

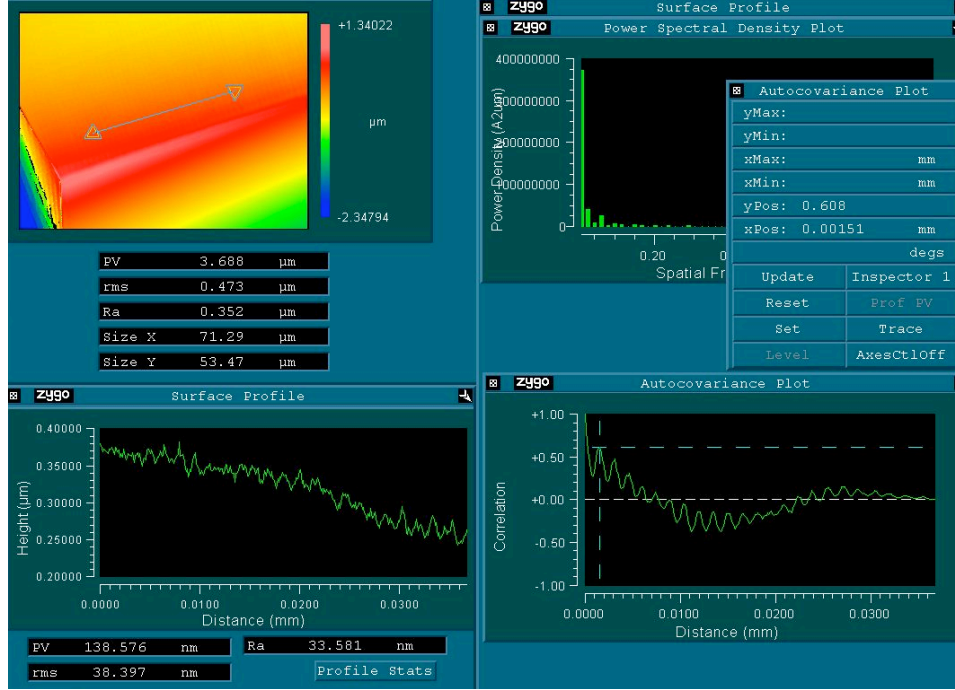


**Figure 4-19:** Trace measurement in the cutting direction (up-feed). Tool moved from the left of the trace to the right. Test 3:  $f = 37.7 \mu\text{m/rev}$ , cutting depth = 5  $\mu\text{m}$ , surface speed = 0.085 m/min. Feature spacing is 1.5  $\mu\text{m}$  as seen in *Autocovariance Plot* menu  $xPos$ .

Arcona concluded that these features are a byproduct of chip segmentation [13]. That research showed that the chip was sheared away from the workpiece by the tool edge and that the shearing mechanism resulted in segmented chip layers with regular spacing called ‘lamella.’ The chip segments sheared from the workpiece surface at a constant angle. The thickness of the lamella was dependant on cutting depth and the shear angle was affected by tool edge radius (sharpness). Arcona gave the following formula for calculating the spacing or thickness of the lamella:

$$t = -.215 + 0.265 * d \quad (4-2)$$

where  $d$  is the cutting depth. For a cutting depth of 5  $\mu\text{m}$ , the lamella thickness from Equation 4-2 is 1.11  $\mu\text{m}$ . Arcona also gave the following formula for spatial period of segmentation in the cutting direction:

$$x = \frac{t}{\sin\theta} \quad (4-3)$$

where  $t$  is the lamella thickness and  $\theta$  is the shear angle. For a sharp tool (edge radius < 0.050  $\mu\text{m}$ ) in electroplated copper the shear angle was 45°. With a lamella thickness of 1.11  $\mu\text{m}$  and a shear angle of 45°, Equation 4-3 yields a segmentation period of 1.57  $\mu\text{m}$ , which is close to the period observed here.

These features were observed at the larger workpiece radii with this cross-feed (37.7  $\mu\text{m}/\text{rev}$ ) but were much less defined. As discussed in Section 4.3.1.2, the frequency response of the Z-axis with spindle in the cutting direction is 64 Hz. At this workpiece radius (1.535 mm), a 64 Hz oscillation would have a spatial frequency in the up-feed direction of 225  $\mu\text{m}$ .

#### 4.2.8 Conclusions

Experiments were conducted to verify surface finish at large feed rates where the parabolic approximation would predict roughness. A tool servo was used to instantly change cutting depths, which prove useful in comparing the theoretical cross-feed profiles to the actual profiles and in examining up-feed features at large chip thicknesses.

Surface finish did not appear to be affected by changes in depth of cut or surface speed. While the experimental profile differed from the theoretical parabolic profile, the calculated RMS roughness from experimental data showed no trend that indicates depth of cut or feed rate influence surface finish.

The theoretical surface finish was close to the predicted values with minimum chip thickness (due to tool edge sharpness) and asynchronous spindle motion effects becoming dominant as cross-feed rate slowed. In all tests, the spacing of the tool passes matched the programmed cross-feed became small. Because asynchronous spindle motion and minimum chip thickness produced features that were independent of the variables tested in this experiment, their contribution was significant in the measured PV and RMS roughness. Tool edge quality is also extremely important to surface finish as the smallest nicks will cause many nanometers of defects in the residual cusp.

Chip segmentation features were observed in the up-feed direction at large chip thicknesses ( $>5 \mu\text{m}$ ) that matched those found by Arcona. The features were less defined at larger workpiece radii, indicating the chip formation mechanics with a round nose tool at large chip thickness change at higher surface speed.

### 4.3 MACHINE VIBRATION

Optical quality surface roughness in single-point diamond turning, as observed in the previous section, is primarily influenced by four factors: cross-feed geometry, material

properties, tool edge quality and machine vibration. As discussed in Section 4.2.2, lubrication for chip removal is essential to create low roughness surfaces. The first-order geometric model using the parabolic approximation gives the peak-to-valley (*PV*) surface roughness and is determined solely by the cross feed (*f*), and the tool radius (*R*) as shown in Equation 2-2. This approximation is often used as the sole determiner for choosing radius and feed rate even though for large radii and small feeds, the predicted finish is not achievable. This effect is observed in the experiments of Section 4.2.4 (more obvious at lower feed rates) where a homogenous material (small grain plated copper), a recently lapped tool with a high quality edge, and a small cross-feed produced a PV of more than 50 nm while theoretical was 23 nm (Test 6). Figure 4-21 shows a relatively large variation in cusp valley depth that partly caused an increase in surface roughness beyond theoretical and can be attributed to machine vibration. As discussed in Section 4.2.8, elastic rebound on trailing edge of the cusp due to minimum chip criterion also contributed to the surface roughness increase.

The impact of machine vibration on a diamond-turned surface is generally to degrade the surface finish. If the machine vibration could be modeled as sinusoidal oscillation in the normal direction, the RMS surface finish would increase by 0.707 times the amplitude of the vibration (RMS of sinusoid amplitude =  $0.707 * \text{amplitude}$ ). It would seem that the surface finish could never be improved beyond this value because vibration motions would be much larger than the cusp features created by a tool at a moderate to low cross-feed. There would then be little merit in slowing the feed rate or using a larger radius tool to reduce surface roughness. To test this assumption, a model was developed to

simulate the interaction between successive tool passes when the tool is vibrating relative to the workpiece surface. The model was designed to draw successive cusps left in the surface by cross feeds (in 2D and 3D) so surface roughness statistics could be calculated. Variables in the model were cross-feed rate, tool nose radius, frequency of sinusoidal machine vibration, and amplitude of machine vibration.

#### *4.3.1 Vibration Motion in Diamond Turning Machines*

The origin of machine vibration can be from a number of sources, although the axes hydrostatic way mechanism or the air bearing which supports the spindle are the most likely candidates because these interfaces are more compliant than the steel structures or granite base of a DTM. Drescher [8] addressed the surface finish capabilities of the ASG-2500 and the relationship between tooling forces, machine vibration, tool edge quality and surface finish. It was found that the motion between the tool and spindle was from the non-influencing coupling for ball screw attachment (~60 Hz for Z-axis, ~89 Hz for X-axis). The only way to eliminate this motion was to stop oil flow to the Z-slide so it rested on the machine base and disable the Z-axis controller. Only then was the predictive model for surface finish accurate for small feed rates.

The influence of small amplitude machine vibration (15 nm) on surface finish has been studied at Hitachi Ltd. [35]. The vibration in these experiments was parallel to the spindle axis and at frequencies lower than the spindle speed (<5.8 Hz). The model developed in that work predicted roughness through the phase difference between

machine vibration and spindle position. It examined the influence of “interference” between adjacent cross-feeds with a large radius tool and a straight tool. Experiments with fly-cut samples showed that surface finish can improve beyond the vibration amplitude and continues to improve with smaller cross-feeds.

Most optical workpieces are fabricated with the surface normal nearly parallel to the Z-axis (the maximum surface normal of the Primary Hyperbola from the spindle rotation axis was about 14°) and it has been shown that roughness is most sensitive to disturbances in this direction [17]. For the following discussions and examples, the ASG 2500 Z-slide will be used as the source of the vibration, though the technique can be applied to any source. This amplitude can vary slightly depending on spindle rpm and its balance. Changes to either of these can result in amplitude changes.

#### 4.3.1.1 Z-axis motion from the spiral groove at workpiece center

Characteristics of the Z-slide dynamic motion were determined by measuring the features diamond-turned near the center of a copper workpiece from Section 4.2. For those tests, the tool was centered with respect to the spindle centerline within 1  $\mu\text{m}$  using the Ogive techniques discussed in Section 2.3.2.1. At a spindle speed of 530 RPM (8.833 rev/s) vibration features at ~60 Hz would not be visible in the normal field of the view of the New View at the workpiece radii used in Section 4.2 as discussed in Section 4.2.7 because less than 1/100<sup>th</sup> of a revolution is captured. At the very center of the part, a spiral is created as the tool moves to the centerline of spindle rotation. Because the

distance from the spindle centerline is small, several complete revolutions are captured. The spiral created at the center of the workpiece is found in Figure 4-20. It was measured with the NewView white light interferometer and imported into MATLAB for analysis. A MATLAB script found in Appendix A (Section 6.1.5) was written to align a spiral trace to the data and perform interpolation along the trace. The number of interpolated points was calculated with the circumference ( $c$ ) at the largest trace radius of 22.4  $\mu\text{m}$  and equating it to the grid sample density found in the NewView data of 0.11  $\mu\text{m}/\text{sample}$  as:

$$\# \text{ of samples} = (c = 2\pi \times 22.4 = 140 \mu\text{m}) / 0.11 \mu\text{m}/\text{sample} = 1270 \quad (4-4)$$

A plot of the spiral fit to the tool path is in Figure 4-21 where the dark line represents the series of points taken to form the groove trace. The spindle speed for this cut was 530 rpm and with 1270 samples per revolution, the trace sample frequency is 11 kHz. The highest un-aliased frequency component, according to the Nyquist, is half the sample rate, or 5.5 kHz. The Z-axis vibration frequency was expect to be less than 100 Hz so the trace data has more than enough information. A plot of the interpolated tool height along the spiral trace is in Figure 4-22.

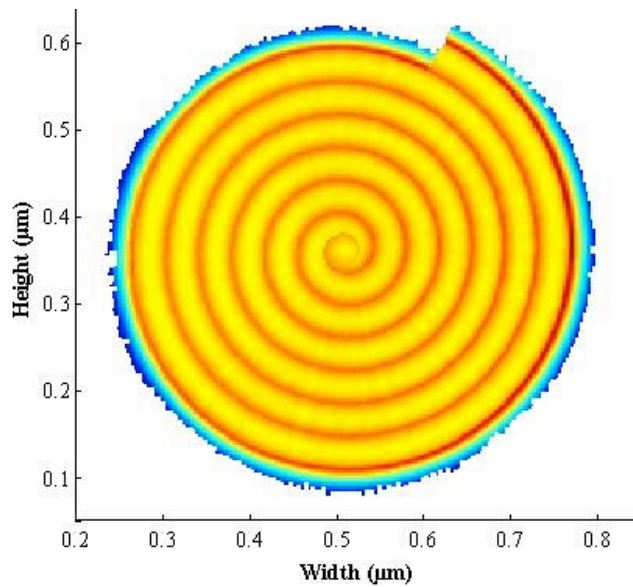


**Figure 4-20:** Diamond-turned cusps forming spiral found at center of workpiece after last tool centering adjustment.

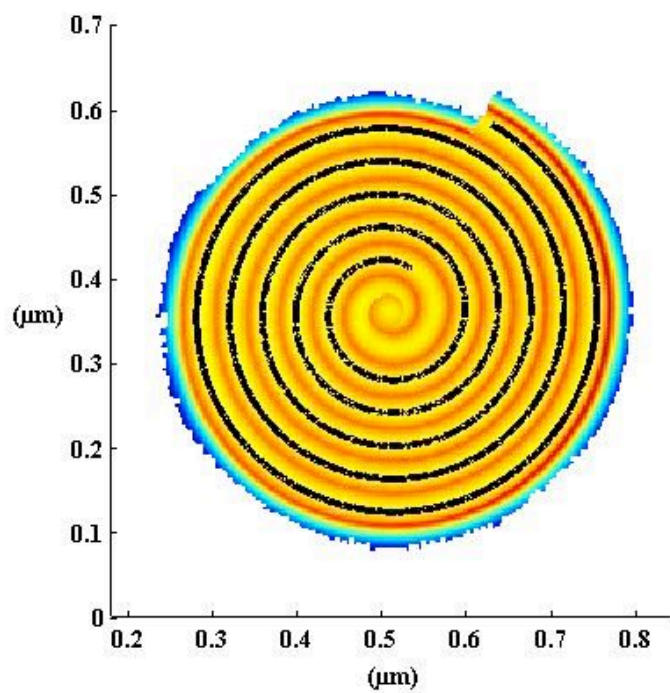


**Figure 4-21:** Center feature found in Figure 4-23 with a spiral trace aligned to the groove bottoms.

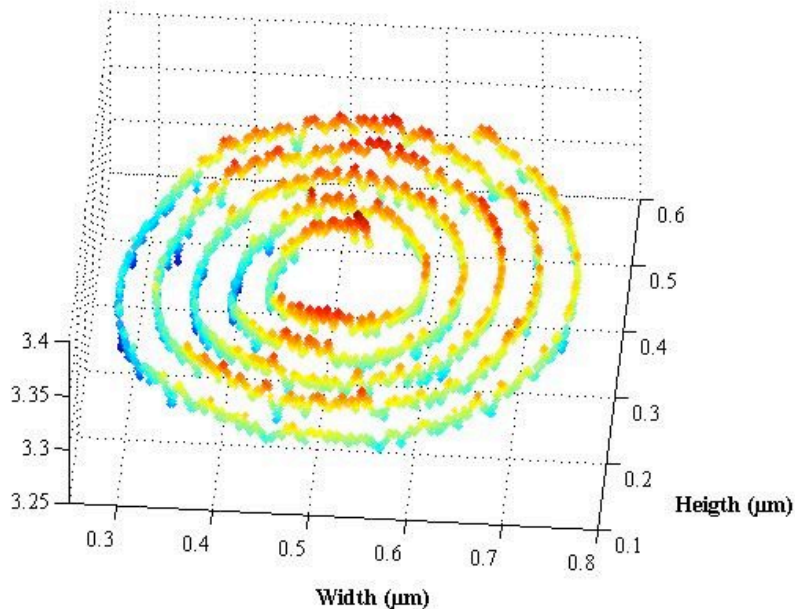


**Figure 4-22:** 3D plot of interpolated points from the spiral trace in Figure 4-24.

#### 4.3.1.2 Frequency response of spiral groove at workpiece center

The spiral trace was analyzed for frequency content and the result is found in Figure 4-23. The first four peaks represent 0.5, 1, 2, and 3 times the spindle speed (530 rpm = 8.833 Hz) or peak 1 = 4.42 Hz, 2 = 8.83 Hz, 3 = 17.7 Hz, and 4 = 26.5 Hz. These points represent synchronous motions of the Z-axis and are most likely a combination of form error, tilt in the measurement and anomalies from taking a Fourier transform of a data set that contains incomplete waves. Synchronous motions at low frequencies have no effect

on surface finish because the height of the tool for a given profile is the same from one revolution to the next. Features occurring at once per revolution (8.833 Hz) and twice per revolution (17.7 Hz) are largest because the synchronous motions of the spindle are largest. The first asynchronous frequency is the fifth peak at 63.6 Hz and is close to the first natural frequency of the Z-axis in the Z-direction. The mass of the Z-axis is constrained by a ball screw with a flexure-based support to decouple any rotary motion of the ball screw from influencing the motion of the slide. The support stiffness is 24 N/ $\mu$ m and the slide mass (with spindle) is 135 kg. The natural frequency is approximately 68 Hz.

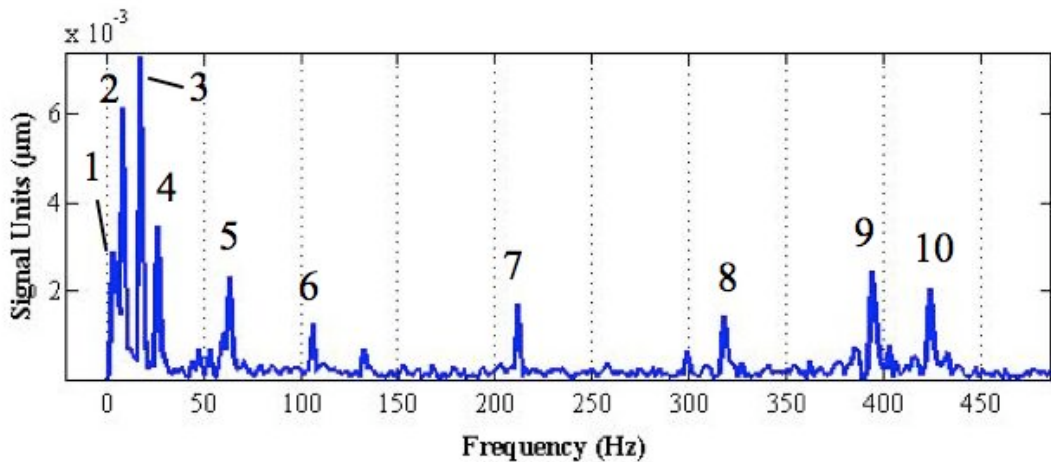


**Figure 4-23:** Frequency response of spiral profile seen in Figure 4-24.

An experiment was conducted using a capacitance gage to measure the closed loop response of the Z-axis when subjected to an impulse. A silicon wafer was vacuumed to the chuck and the cap gage clamped to a tool holder that was bolted to the X-axis. The cap gage was aligned perpendicular to the silicon wafer and the Z-axis was jogged

towards the cap gage with open loop commands to the cap gage null position (output = 0 volts). The voltage output of the cap gage was fed into an oscilloscope, which was configured to calculate the dominant frequency of the output signal. Closed loop control was initiated to hold the null position and to provide an experiment that duplicated normal cutting conditions. A rubber hammer was used to tap the Z-axis table in the Z-direction to create an impulse disturbance. The oscilloscope calculated the settling frequency as 64 Hz, which confirmed the frequency analysis performed on the center spiral.

The sixth, seventh, eighth, and tenth peak in the data represent 12, 24, 36, and 48 times the spindle speed or 106, 212, 318, and 424 Hz. The sixth is caused by ASG 2500 air-bearing spindle because it has twelve air pads and the seventh, eight, and tenth are harmonics of the marks caused by the 12 pads. The features caused by the pads have been measured and are less than 5 nm. The ninth peak at 394 Hz and the high frequency peaks from the spindle pads are insignificant in terms of machine vibration because the Z-axis will respond at its first mode of 64 Hz when excited [23].

#### 4.3.1.3 Vibration Amplitude from Workpiece

The amplitude of Z-axis vibration was found by analyzing the surface profiles from the experiments conducted in Section 4.2. Several sets of traces were examined and the maximum trough-to-trough separation of 22 nm from Figure 4-17 in Section 4.2.6 was set as the vibration magnitude. This traced showed significant separation while still

clearly demonstrating the expected number of cusps. At lower cross-feeds, the cusps were less obvious and it was difficult to discern the trough locations.

#### *4.3.2 Surface Finish Model with Vibration*

The variables used to model surface finish with machine vibration are cross-feed rate, tool nose radius and sinusoidal motion parameters of the ASG-2500 as discussed in Section 4.3.1. Like Section 4.2, the model assumes ideal cusps created by a round nose tool with perfect edge sharpness and homogenous materials that are appropriate for diamond turning. The model is independent of surface speed or depth of cut, as the results of Section 4.2 show. Also, the location of the simulated surface profile was at a large radius on the workpiece (all simulations used 20 mm) so the diamond turned grooves would be nearly straight for a 3D surface profile of conventional dimensions. At the large radius, the circumferential distance between points was assumed equal at every radius.

The surface profile was formed by 1) calculating a rectangular matrix of tool tip positions, 2) calculating the tool tip depth for each point in the center matrix, 3) solving the two dimensional surface profiles along radial lines from the spindle centerline (cross-feed direction) with equal angular spacing called meridians and 4) stacking the cross-feed traces in the up-feed direction to generate a three dimensional profile. The first step in the program was input of machining parameters: feed rate, spindle speed in RPM, tool nose radius in  $\mu\text{m}$ , machine vibration frequency in Hz, and machine vibration amplitude

in  $\mu\text{m}$ . Then the model parameters were input: the number of points and tool passes in the cross-feed profile. For the modeled data found in Section 4.3, the spindle speed was 500 RPM, the machine vibration frequency was 63.6 Hz (Section 4.3.1.2), the vibration amplitude was 11 nm (Section 4.3.1.3), the cross-feed trace had 201 data points and there were 20 tool passes. Careful selection of the spindle speed was needed to ensure that the generated surface profile didn't exhibit any aliased frequencies because profiles with aliased content had falsely large surface roughnesses (4-7x parabolic PV). The ratio of machine vibration frequency to spindle speed for the modeled data was 7.632. The ASG-2500 spindle speed varies over a range of about 5 RPM with no apparent trend when commanded to turn 500 RPM. The varying speed causes the vibration phase to change slightly from one revolution to the next, which will prevent any aliased vibration features from appearing in the surface roughness.

#### 4.3.2.1 Tool Tip X and Z Position

The tool tip locations were calculated from the input variables. The spacing of the tool tip in the cross feed direction was set by multiplying the number of passes by the cross-feed rate. The spacing of the tool tip in the up-feed direction was set by dividing the length of the cross-feed profile by the number of data points for the cross-feed profiles; this was done to make data point density equal for up-feed and cross-feed. With the tool tip spacing known, tool center vectors were calculated for the X and  $\Theta$ -directions. Figure 4-24 shows a workpiece with the axis of rotation and has a section view illustrating the X and  $\Theta$ -center vectors used to calculate tool tip locations.  $\Theta$ -direction was used, rather

than Y-direction, to preserve the idea that the cross-feed profiles were modeled along a meridian representing a discrete angle with respect to workpiece centerline. While X-direction centers were set by the feed rate,  $\Theta$ -direction centers were found by a small angle approximation ( $\Theta = \text{arc length} / \text{workpiece radius}$ ) of the up-feed length.

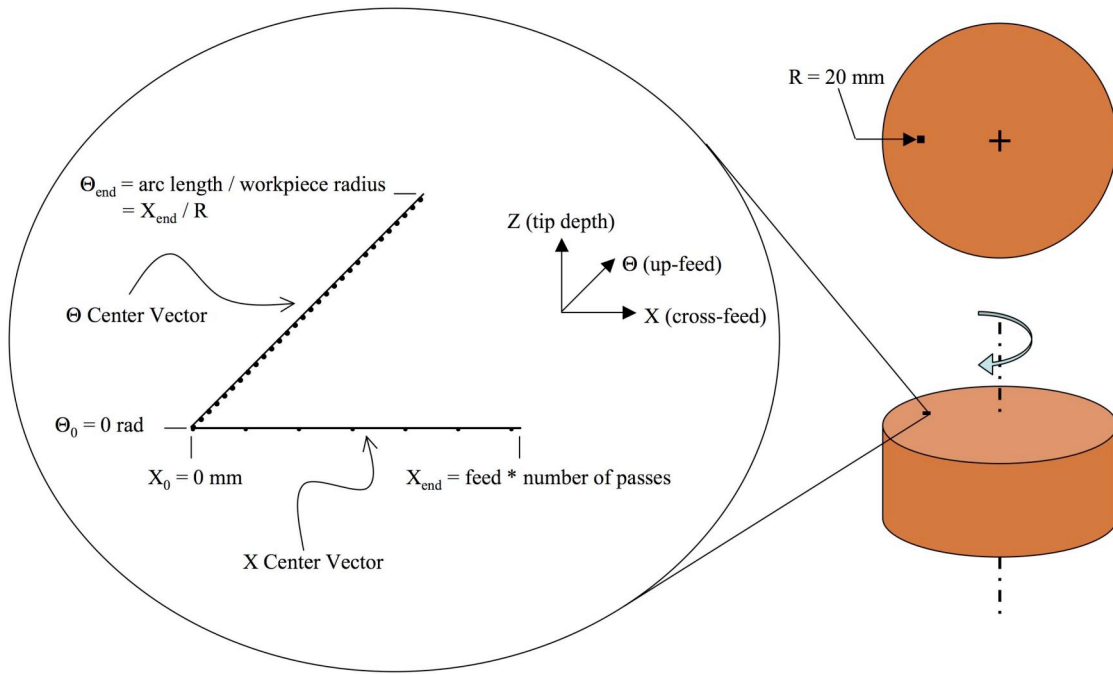


**Figure 4-24:** X and  $\Theta$  vectors of tool center showing model coordinate system with relationship to workpiece and rotation centerline.

To take advantage of MATLAB vectorization routines in later calculations (loop elimination through calculation along vectors), the center vectors were expanded to matrices. The tool center vectors were input to the MATLAB function *meshgrid*, which produce X and  $\Theta$ -center matrices. The X-center matrix had rows that were copies of the X-center vector; the number of rows was equal to the number of points in the  $\Theta$ -center

vector. The  $\Theta$ -center matrix had columns that were copies of the  $\Theta$ -center vector; the number of columns was equal to the number of points in the X-center vector. Thus, both matrices were number of tool passes wide, by number of points tall.

The tool center matrices were input to Equation 4-5 to calculate the tool depth at each tool tip location. The result was a third matrix (same dimensions as the tool tip matrices) that contained the tool tip depths. The change in depth of cut around the periphery of the part with the vibration environment can be expressed as:

$$depth = A \cdot \sin\left(\frac{\omega x}{\Omega f}\right) \quad (4-5)$$

where  $A$  is the vibration amplitude,  $\omega$  is the vibration frequency of the tool,  $x$  is the radial position of the tool center and  $\Omega$  is the vibration frequency of the spindle. Because the tool center matrices were in the X and  $\Theta$ -directions and tool depth was only a function of the radial X-position, the  $\Theta$ -position was converted into a X-position increment by a small angle approximation ( $\Delta X = (\Theta/360^\circ) * \text{cross-feed}$ ) and summed with the X-position for input to Equation 4-5.

#### 4.3.2.2 Surface Profiles

The surface profiles were calculated in the cross-feed direction along meridians because the variation in height of adjacent tool passes caused each cusp to individually influence

the final profile as demonstrated in Figure 4-253zz. The shape of the cusps were calculated with the Cartesian formula of a circle:

$$(x - x_0)^2 + (z - z_0)^2 = R^2 \quad (4-6)$$

where  $x$  is the vector of evenly spaced x-positions,  $x_0$  is the vector of cross-feed tool centers taken from the X tool-center matrix,  $z$  is the vector of z-positions,  $z_0$  is the vector of tool tip depth taken from the matrix calculated with Equation 4-5, and  $R$  is the tool nose radius. A set of  $z$  values was calculated for all tool tip locations  $(x_0, z_0)$  for each  $x$  in the vector of x-positions. Only the minimum  $z$  for each  $x$  in the x-position vector was retained, thus producing the lowest point in the profile for each x-position. The final product was a pair of equal length x-position and z-position vectors, which describe a surface that only displays the residual cusps. Also, this gives a final surface profile with constant sample density in the x direction.

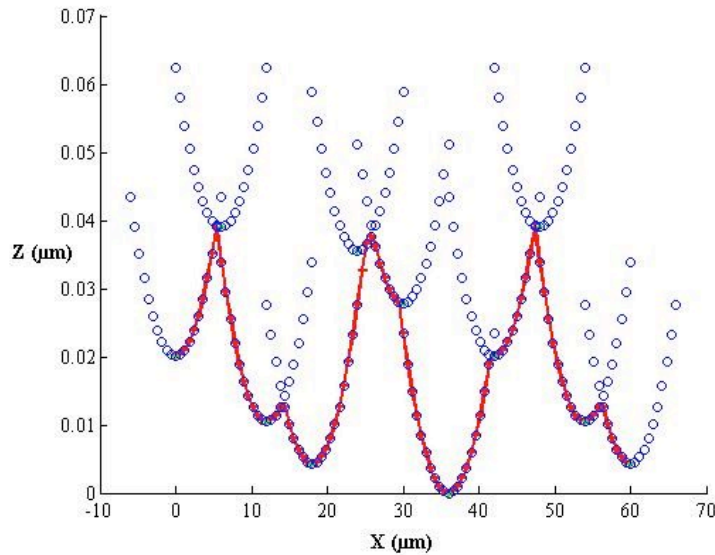


**Figure 4-25:** Certain points from multiple tool cups (circles), at varying depths due to vibration, produce a finished surface contour (line).

As shown in Figure 4-25 where complete tool edges from adjacent cusps have been generated (circles), the redundant points in the overlapping regions do not appear in the final surface contour (line). Individual cross-traces at different rotational positions of the spindle can then also be assembled into 3D profiles as shown in Figure 4-26. When creating the 3D profile, the number of traces stacked in the Y direction is equal to the number of points per trace in the X direction allowing a sample with a uniformly spaced grid of data points.

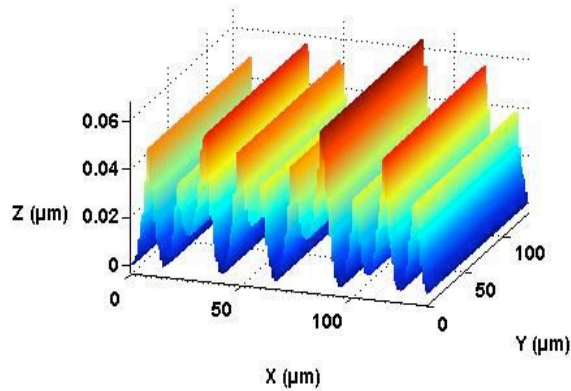


**Figure 4-26:** Consecutive surface contours in the cross-feed direction ( $X$ ) were stacked in the up-feed direction ( $Y$ ) into a 3-D surface.

#### 4.3.2.3 Fine Cross-feed Rates

It is at lower feed rates as illustrated in Figure 4-27 that the effects of tool vibration on a diamond-turned surface become interesting. The plot shows the surface profile for a small cross-feed rate while the crosshairs show the apex of tool for each pass. A number of passes are completely absent from the finished surface, leaving only the most extreme passes and, hence, a smoother surface than would be expected with machine vibration.

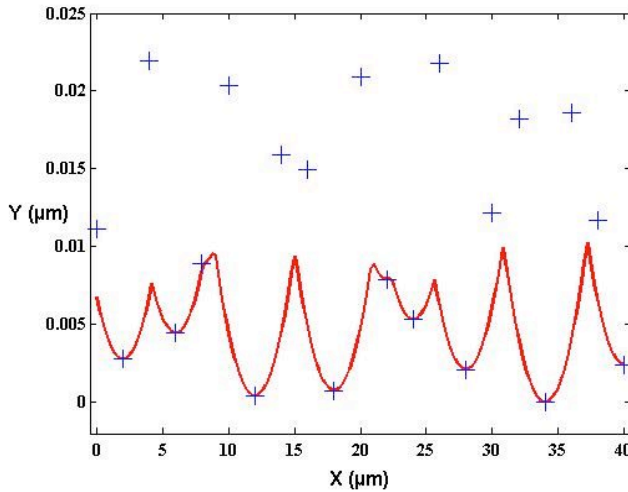


**Figure 4-27:** At fine cross-feed rates, some passes of the tool (+) are not represented in the finished surface. This produces a better finish than would be expected from the RMS of the vibration alone.

Figure 4-28 shows the relationship between the theoretical RMS finish as calculated with parabolic approximation and the RMS finish modeled with machine vibration. The figure indicates that as the theoretical RMS surface finish decreases, the effects of machine vibration on roughness are diminished. Reduction of the roughness data in Figure 4-28 was done by decreasing cross-feed rates while holding tool radius constant (480  $\mu\text{m}$ ). The feed rates were 1.13, 1.60, 3.58, 5.06, 11.3, and 16.0  $\mu\text{m}/\text{rev}$ . At the higher theoretical roughness of 20 nm (large cross feeds) the effect of vibration adds only a couple nanometers (10%) to the modeled roughness. As the theoretical RMS roughness decreases to 3 nm, the vibration influences double RMS, indicating a profile shape similar to Figure 4-25 where most pass are represented but the height difference between cusps is large. However, as the feed rate (and thus the theoretical surface finish) falls

below this point, many tool passes are absent from the final profile and the modeled RMS starts to decrease rapidly (as in Figure 4-27). The shape of the curve in Figure 4-28 is similar to the curve reported by Takasu [35].

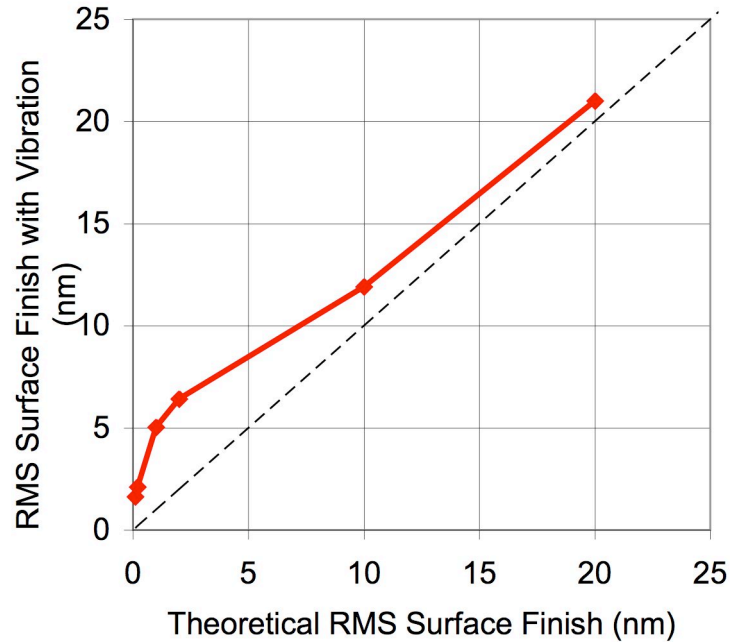


**Figure 4-28:** As theoretical surface finish decreases, the effects of machine vibration on surface finished are reduced. Vibration PV = 22 nm and RMS = 7.7 nm.

#### 4.3.3 Experimental Results and Discussion

An electroplated copper sample was machined with the same feed rates used in the model. The machining experiments were performed on an ASG-2500 DTM with a 500 rpm spindle speed and a 480  $\mu\text{m}$  radius, zero degree rake angle single-crystal diamond tool. Special care was taken when setting up this experiment such that the freshly

sharpened diamond had minimal cutting exposure before the test was run. The laboratory temperature was controlled to  $20 \pm 0.05^\circ\text{C}$ . Cutting fluid (Mobilmet Omicron®) was sprayed from a PEC custom-built system for lubrication and chip removal. The workpiece used was electroplated copper, like the sample cut in the first-order regime tests in Section 4.2. The tool moved across the part from OD to ID.

Seven 2 mm wide bands were machined on the 50 mm diameter sample with cross feeds of 1.13, 1.60, 3.58, 5.06, 11.3, 16.0, 35.8  $\mu\text{m}/\text{rev}$ . The surface was cleaned by spraying it with (in order) Mineral Spirits, Acetone, Methanol and an industrial-grade degreasing soap diluted with de-ionized water. Optical grade wipes were used to gently scrub (no direct pressure) the surface and it was rinsed with de-ionized water before another wipe was used to absorb the water standing on the surface. It was then measured on a Zygo NewView 5000 Scanning White-Light Interferometer (SWLI) using 50X & 100X magnification. The measurement area was 108  $\mu\text{m}$  tall by 144  $\mu\text{m}$  wide and 55  $\mu\text{m}$  tall by 72  $\mu\text{m}$  wide, respectively. Figures 4-29 and 4-30 show the typical profile measurement result. The effects of vibration on groove depth ( $\sim 7.5$  nm) are seen in the profile at this large feed rate. The depth varies with no repetitive cycle as the tool traverses the part. Note that the cusps are free of any repeated features and that they have smooth shapes. This indicates a sharp tool with small edge radius and high edge quality.

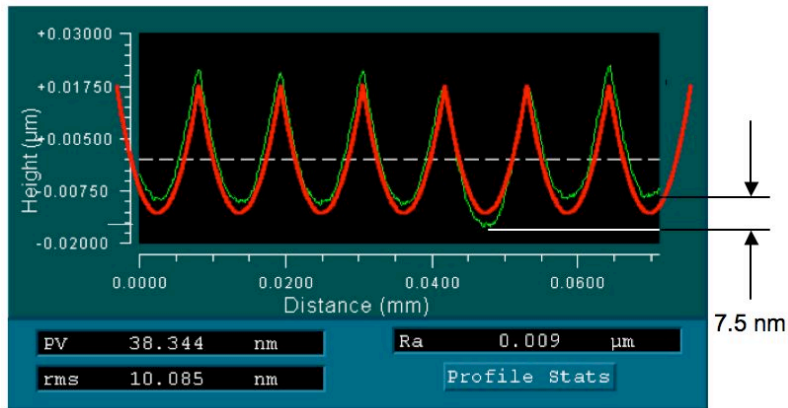


**Figure 4-29:** Typical surface profile measurement illustrating the depth change as a result of vibration with large feed rate of 11.3  $\mu\text{m}/\text{rev}$ . Theoretical PV = 33 and Theoretical RMS = 10 nm drawn with bold line.

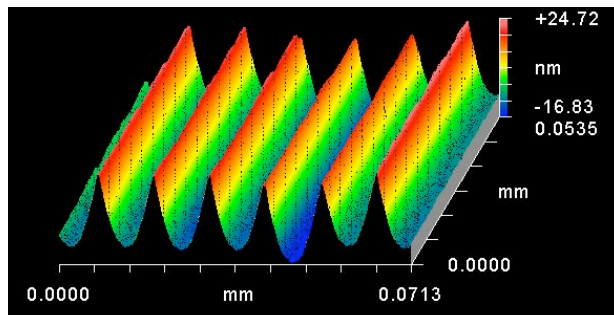


**Figure 4-30:** Typical measurements result in oblique plot form. This is the same surface shown in Figure 4-29.

The results for the series of simulations and experiments are in Figure 4-31, which shows the RMS of machine vibration (7.7 nm), the theoretical RMS roughness from the parabolic approximation (curved solid line), and the model predicted RMS roughness trend (dashed line). The theoretical RMS roughness is calculated from Equation 4-1

where  $f$  is the cross-feed rate in  $\mu\text{m}/\text{rev}$  and  $R$  is the tool radius (480  $\mu\text{m}$ ). For each feed rate, there are 5 data points from both the model and experiment (in both cases, found by moving circumferentially around the workpiece at constant radii). Clearly, the surface finish can be significantly better than RMS 7.7 nm limit of a simple sinusoidal vibration. The finish also continues to improve with finer feed rates where the RMS roughness deviates significantly from the theoretical parabolic approximation. The shape of the deviation is similar to the shape of the model in Figure 4-28. The mean of the measured RMS roughness for each feed rate follows the predicted shape and, while larger than theoretical RMS, is smaller than the modeled roughness for the feed rates larger than 2  $\mu\text{m}/\text{rev}$ . This would suggest that the simulated asynchronous sinusoidal vibration is slightly smaller than that described by Section 4.3.1.3. At feed rates lower than 2  $\mu\text{m}/\text{rev}$  the model more closely matches the experimental values but other effects like minimum chip thickness likely limit the RMS to about 2 nm. These effects are also the cause of the large spread seen in the data at the 3.08 and 5.06  $\mu\text{m}/\text{rev}$  feed rates.

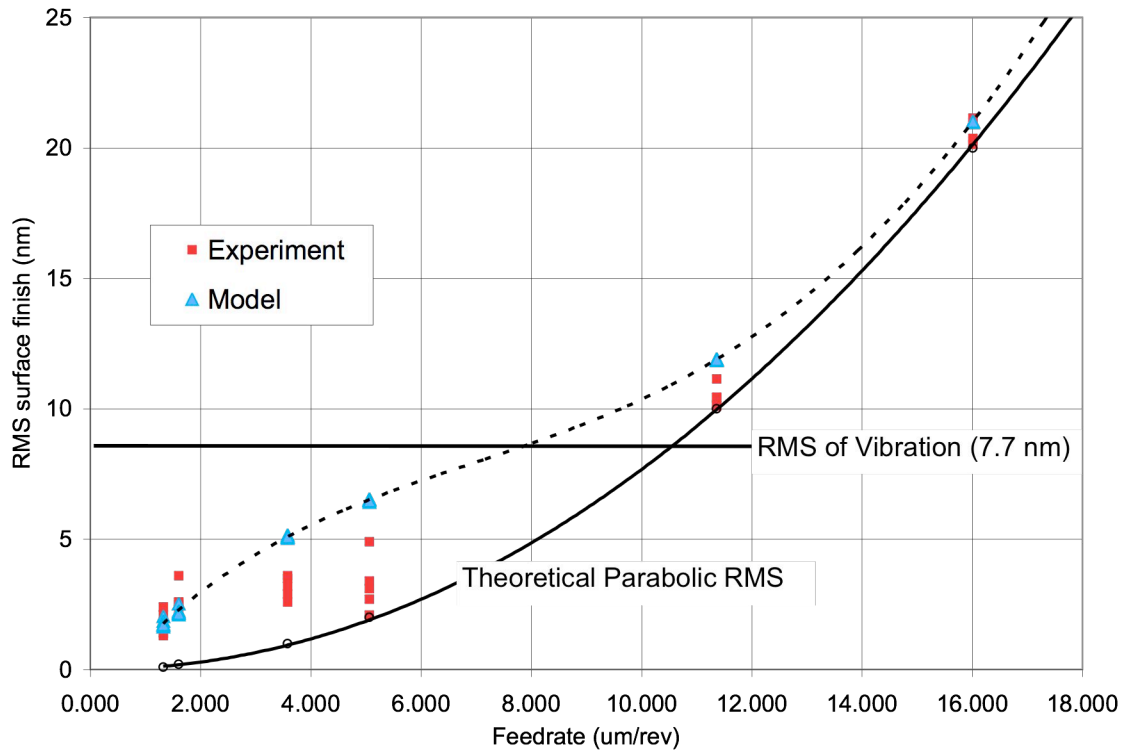
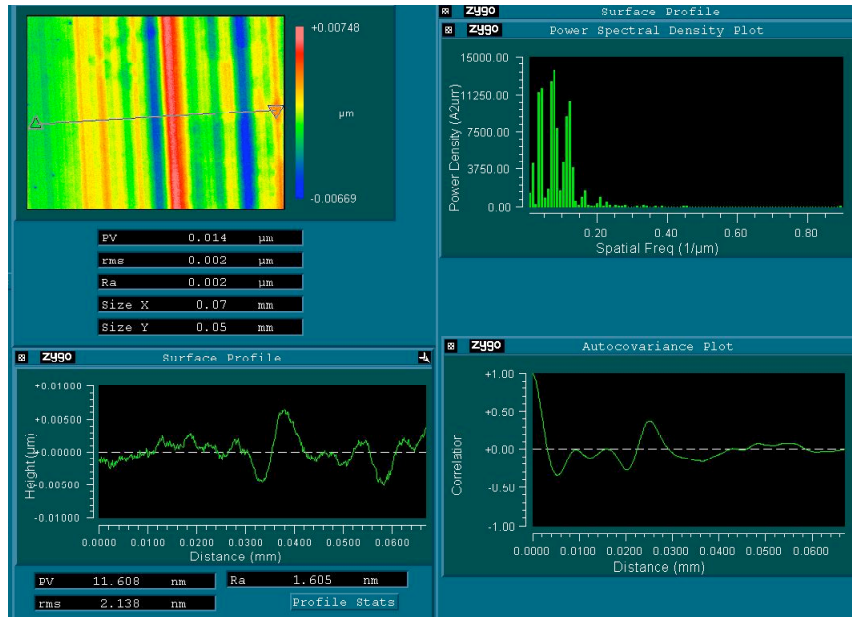


**Figure 4-31:** Results from experimental and model data with threshold of RMS Z-axis vibration, a curve to represent the theoretical parabolic RMS surface roughness and a dashed line to represent model prediction.

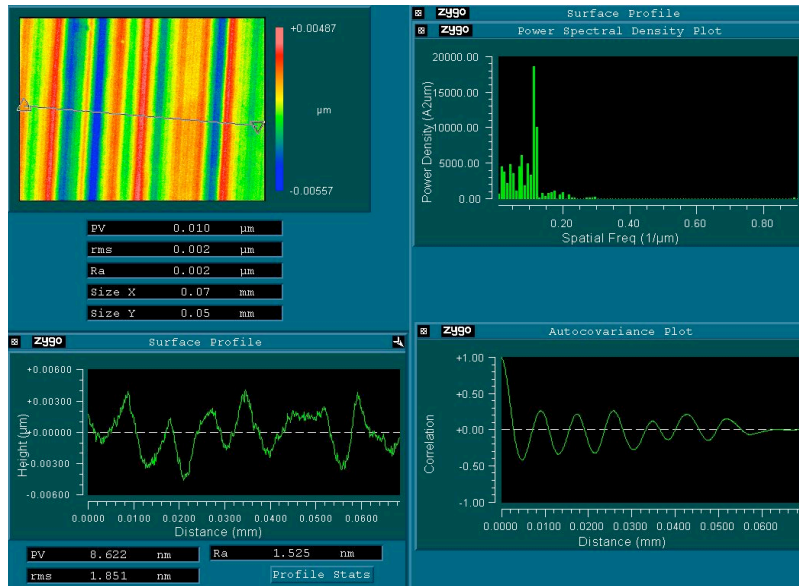
#### 4.3.3.1 Cross-Feed Spacing from Surface Profiles and Comparisons to Modeled Surface

Figures 4-32, 4-33, and 4-34 show measurements of the  $1.13 \mu\text{m}/\text{rev}$  cross-feed (tool radius =  $480 \mu\text{m}$ , spindle speed = 500 RPM, Theoretical PV = 0.3 nm) from the NewView MetroPro software. Each figure contains a 3D surface profile, cross-feed trace, autocovariance of the trace, and PSD (Power Spectral Density) of the trace. The PSD and autocovariance function are described later in Section 4.4.1 and are used here to

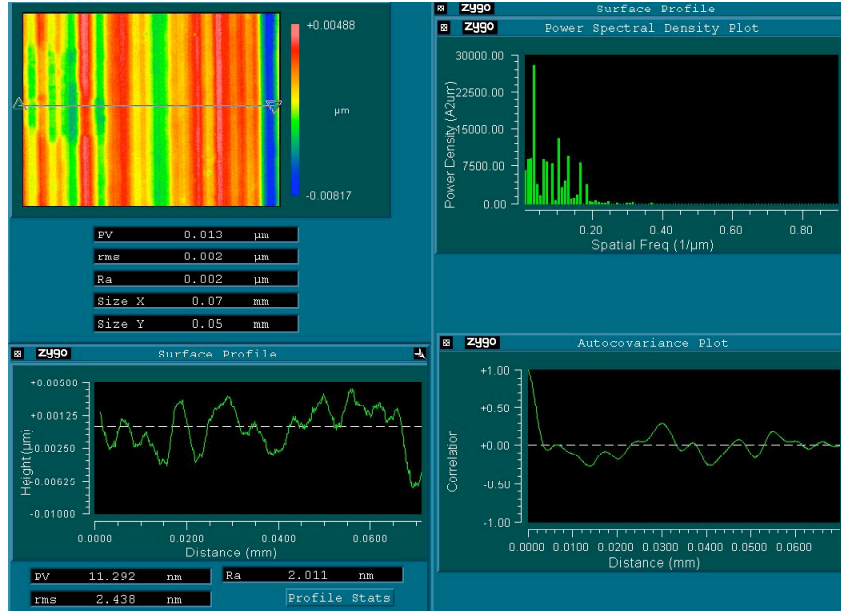
examine cross-feed cusp spacing. In these three plots and the following three (Figures 4-35 to 4-47) the PSD horizontal scale of *Spatial Frequency* was set from 0 to 0.9 1/ $\mu\text{m}$  for direct comparison. In each measurement of the 1.13  $\mu\text{m}/\text{rev}$  cross-feed, it appears that grooves from the tool nose radius are discernable in the 3D surface profile but the grooves do not correspond to the cross feed. The autocovariance indicates regularly spaced features in only one measurement (Figure 4-33) and the distance between the oscillatory peaks in that autocovariance for that case is about 9  $\mu\text{m}$  or 8x the cross-feed. The PSD shows no peak at the spatial frequency corresponding to the cross-feed ( $1/1.13 = 0.88$  1/ $\mu\text{m}$ ) in any of the measurements; only random content at much lower frequency (lower frequency corresponds to larger groove spacing). This supports the modeled results where low cross feeds only leave indication of a small percentage of the tool passes expected. The next largest feed rate of 1.60  $\mu\text{m}/\text{rev}$  had similar results with a slightly larger RMS roughness.



**Figure 4-32:** Measurement of 1.13  $\mu\text{m}/\text{rev}$  cross-feed with 3D profile, cross-feed trace, autocovariance of trace, and PSD of trace. Grooves are present, but there is little indication of cross-feed.



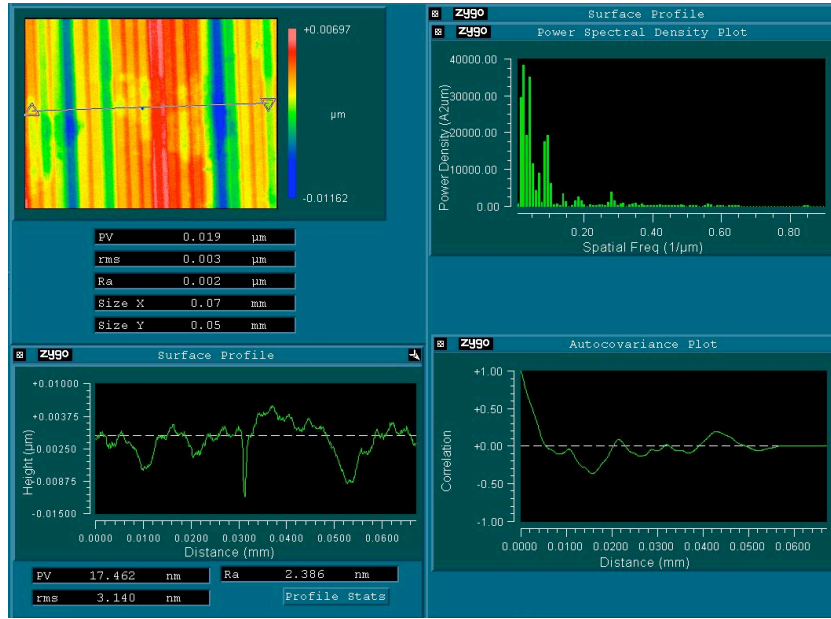
**Figure 4-33:** Measurement of 1.13  $\mu\text{m}/\text{rev}$  cross-feed with 3D profile, cross-feed trace, autocovariance of trace, and PSD of trace. Autocovariance shows recurrent features at 8x (9  $\mu\text{m}$ ) the feed rate.



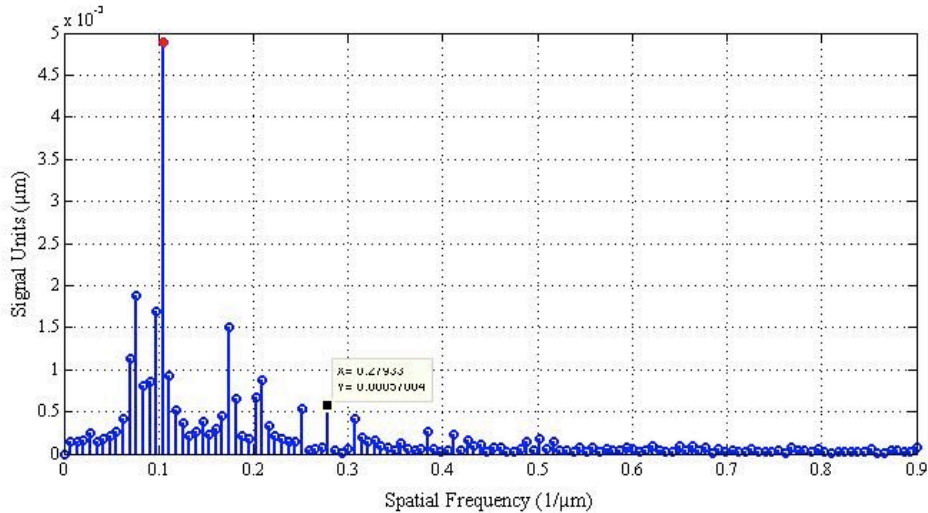
**Figure 4-34:** Measurement of 1.13  $\mu\text{m}/\text{rev}$  cross-feed with 3D profile, cross-feed trace, autocovariance of trace, and PSD of trace. Little indication of cross-feed is seen but larger spacing is shown.

Figure 4-35 shows a measurement of the third smallest feed rate of 3.58  $\mu\text{m}/\text{rev}$  with the same MetroPro layout as the 1.13  $\mu\text{m}/\text{rev}$  measurements above. The autocovariance plot for this feed rate indicates the cusp features have little regularity in spacing, like the 1.13  $\mu\text{m}/\text{rev}$  measurements. However, the MetroPro PSD does show significant frequency content at the specified feed rate ( $3.58 \mu\text{m}/\text{rev} = 0.27 \text{ } 1/\mu\text{m}$ ). The peak at the cross-feed is much smaller than the peaks at lower frequency (or larger spacing), which indicates that most tool passes at this feed rate are represented but that the large differences in groove height and width from machine vibration cause the profile to have significantly larger roughness than theoretical. This matches the prediction of the model discussed in Section 4.3.2.2. Figure 4-36 shows a PSD of the modeled surface finish with machine

vibration amplitude of 9 nm (Section 4.3.2.2) that exhibits a peak at 0.27 1/ $\mu$ m. When using vibration amplitude of 11 nm from Section 4.3.2 there was little indication of the cross-feed, however reduction of the amplitude to 9 nm as suggested in Section 4.3.3 provided a distinguishable peak at the cross-feed.



**Figure 4-35:** Measurement of 3.58  $\mu$ m/rev cross-feed with 3D profile, cross-feed trace, autocovariance of trace, and PSD of trace. PSD shows small peak at feed rate (3.58  $\mu$ m/rev = 0.27 1/ $\mu$ m)



**Figure 4-36:** PSD of modeled surface profile with  $3.58 \mu\text{m}/\text{rev}$ . Vibration amplitude reduced to 9 nm (from 11 nm) where a peak at  $0.27 1/\mu\text{m}$  was evident. This matches the PSD in Figure 4-35.

Figure 4-37 shows a measurement of the  $5.06 \mu\text{m}/\text{rev}$  feed rate with the same MetroPro layout as the four measurements above. The autocovariance plot indicates that the cusp features have highly regular spacing because oscillatory peaks have a consistent  $5 \mu\text{m}$  span. Also, the PSD has a large peak at the feed rate ( $5 \mu\text{m} = 0.20 1/\mu\text{m}$ ), which indicates that the effect on groove height and width from machine vibration was smaller at  $5 \mu\text{m}/\text{rev}$  than at the lower cross-feeds. Figure 4-38 shows a PSD of the modeled surface profile with vibration amplitude reduced from 11 nm (Section 4.3.2) to 9 nm like that used for the  $3.58 \mu\text{m}/\text{rev}$  modeled PSD in Figure 4-36. A peak at  $0.2 1/\mu\text{m}$  is easily distinguished. Figures 4-31 and 4-32 show the next feed rate of  $11.3 \mu\text{m}/\text{rev}$  where the height of the grooves has become much larger ( $\text{PV} = 39 \text{ nm}$ ) so the influences of machine vibration on roughness are minimized.

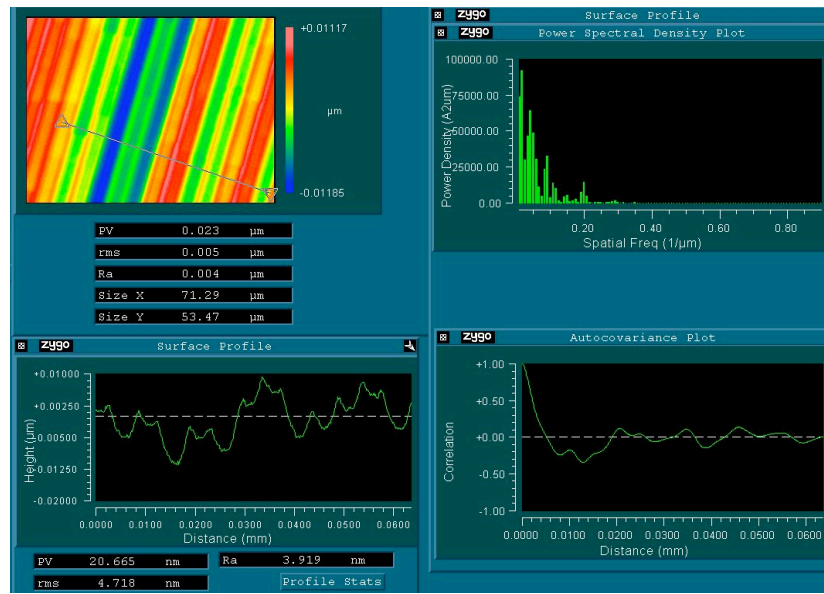


**Figure 4-37:** Measurement of  $5.06 \mu\text{m}/\text{rev}$  cross-feed with 3D profile, cross-feed trace, autocovariance of trace, and PSD of trace. PSD has a peak at the feed rate ( $5.06 \mu\text{m}/\text{rev} = 0.20 \text{ } 1/\mu\text{m}$ ).

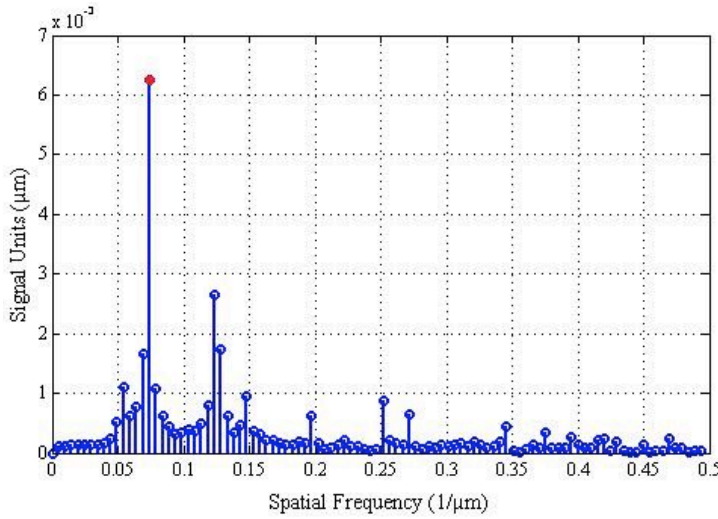


**Figure 4-38:** PSD of modeled surface profile with 5.06  $\mu\text{m}/\text{rev}$ . Vibration amplitude was reduced to 9 nm (was 11 nm) where a peak at 0.20  $1/\mu\text{m}$  was evident.

#### 4.3.3.2 Controller Tracking Error

Another contribution to a degraded surface finish is position errors due to the control of the axes. In the case of the ASG, tests of the custom, DSP-based, controller showed tracking errors of less than 10 nm Peak-to-Valley as seen in Section 2. While of some significance, the effects of this tracking error are at relatively low frequencies and mostly affect form errors. Controller tracking can improve surface finish only when the closed-loop bandwidth of the axes [32] and controller speed [9] have been increased. The ball screw drives on the ASG-2500 are the chief limiter of closed loop bandwidth and several feedback control algorithms have been attempted to improve the response [32]. Also, a “dead-band” of this mechanical actuation has been observed at approximately 20 nm [14]. As discussed earlier, the diamond turning machines most recently available for

purchase utilize DC brushless linear actuators (low torque ripple designs) to drive the axes. These systems have no backlash or mechanical linkage and, coupled with a high-speed controller, tracking errors at surface finish frequencies may be better corrected [9].

#### ***4.3.4 Conclusions***

Surface finish was better than the spindle vibration magnitude at small feed rates. Finer feed rates continue to reduce RMS roughness, even with the impact of machine vibration, to the point where material properties, tool edge quality and tool edge sharpness become dominant factors. In the particular case of the ASG-2500 DTM where machine vibration was measured as 7.7 nm RMS, a surface finish of less than 2 nm RMS was measured with a 0.5 mm tool, a cross-feed of 1.13  $\mu\text{m}$  and a spindle speed of 500 rpm in electroplated copper. Analysis of the experimental data showed that tool passes were missing from the final surface profile as predicted by the surface finish model with machine vibration. The factors described above dominate at this slow feed-rate and until these the impact of these factors is reduced, smaller feed rates add time to the machining effort with little gain. For optical systems fabricated from 6061-T6 aluminum alloy, use of a pure aluminum coating such as Alumiplate® on the optical surface will achieve a finish similar to that seen in the electroplated copper.

## 4.4 CROSS-FEED TOOL DITHERING TO REDUCE DIFFRACTION FROM DIAMOND TURNED CUSPS

The precisely controlled cross-feed rate of the tool in a diamond turning process can produce a surface that has periodic cusps (Section 4.3.3.1 at higher feed rates). These regularly spaced cusps act like a diffraction grating for light incident to the surface, which results in the reflected light exhibiting an interference pattern (also called a diffraction pattern). For an incident beam of a single wavelength, the scatter pattern consists of discrete points along a line that is parallel to the cross-feed. Also, the range of wavelengths found in white light are affected differently by the grating and will produce separate scatter patterns that cause the “rainbow” appearance of some diamond turned surfaces. While the shape of the scatter pattern is determined by cusp spacing, the intensity of the scattered light is determined by the surface roughness; larger roughness scatter more light. The surface roughness and diffraction effects from cusps traditionally limit diamond turned optics to infrared and near-infrared wavelengths [9] that are large in comparison to the shallow, narrow grooves in a diamond turned surface. This section explores dithering the tool in the cross-feed direction to reduce regularity of cusp spacing, thereby smoothing the inference pattern from intense, discrete points to a smooth, continuous line as discussed in later in Section 4.4.1.

### 4.4.1 *Principles of Optical Scattering from Diamond Turned Surfaces*

For discussions of scattering from diamond turned surfaces, the evenly spaced cusps of a diamond turned surface can be thought of as a summation of sinusoidal components

calculated through Fourier transformation of the surface profile [27]. Each sinusoid found in the Fourier transform will create a diffraction pattern as described by the sinusoidal grating diffraction equation [27]:

$$\sin\theta_n = \sin\theta_i + nf\lambda \quad (4-7)$$

where  $n$  is the diffraction order ( $n = \pm 1, \pm 2, \pm 3\dots$ ),  $\theta_n$  is the angle of each order with respect to the surface normal,  $\theta_i$  is the incident light angle with respect to the surface normal,  $f$  is the sinusoid spatial frequency (1/wavelength) of the surface, and  $\lambda$  is the wavelength of incident light. Figure 4-39 shows the positions of the diffracted modes relative to the surface normal. The incident light beam is reflected about the surface normal.

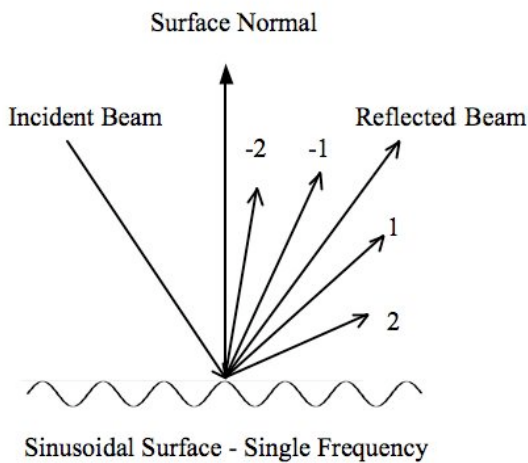


**Figure 4-39:** Diffraction pattern from a sinusoidal surface.

The diffraction patterns created by each sinusoid are then summed to form the diffraction pattern created by the surface. Fourier transform of a surface profile into discrete sinusoidal gratings is applicable for surfaces with less periodic features provided a Fourier transform of the profile yields valid frequency content. The sinusoidal grating diffraction equation (Equation 4-7) predicts that scatter angles for different orders will differ with the wavelength of the incident beam so white light, which contains all wavelengths between ultra-violet ( $\lambda = 390$  nm) and near-infrared ( $\lambda = 780$ ), will yield a different pattern for each wavelength prescribed. This is the diffraction effect that can separate white light into the colors of a rainbow. Table 4-2 gives examples of the diffraction angles found from four wavelengths spread over the white light spectrum with  $\theta_i = 0^\circ$  (parallel to surface normal) and  $f$ , the spatial frequency of features on the surface, of  $0.2 \text{ } \mu\text{m}^{-1}$  ( $5 \text{ } \mu\text{m}$  wavelength) for the first four diffraction modes. The relationship between light wavelength and scatter-mode angle is linear so, for a given angle of incidence, the difference in angular spacing between two wavelengths is proportional to the ratio of the two wavelengths. This can be seen in Table 4-2 where the first mode of  $\lambda = 780$  nm light is reflected at an angle ( $9^\circ$ ) equal to the second mode of  $\lambda = 390$  nm light ( $780:390 = 2:1$ ). For every mode of 780 nm light, there will be two modes of 390 nm light. As the surface spatial frequency increases, the angle of each diffraction order increases until they become larger than  $90^\circ$ , at which point they diffract into the sample and contribute to absorption. Also, the spot diameter of the incident beam must be several times larger than the spatial wavelength ( $1/f$ ) to create scatter patterns.

**Table 4-2:** Angles of diffraction for four diffraction orders and four wavelengths over visible (white light) spectrum. Incident beam is parallel with the surface normal ( $\theta_i = 0^\circ$ ) and the surface spatial frequency is 0.2 waves/ $\mu\text{m}$  (or 5  $\mu\text{m}$  sinusoid wavelength).

| Diffraction Order                  | 1   | 2  | 3  | 4  |
|------------------------------------|---|----|----|----|
| Light Wavelength ( $\mu\text{m}$ ) | Angle of Diffraction Order from Surface Normal ( $^\circ$ ) |    |    |    |
| 0.780                              | 9   | 18 | 28 | 39 |
| 0.6328                             | 7   | 15 | 22 | 30 |
| 0.500                              | 6   | 12 | 17 | 24 |
| 0.380                              | 4   | 9  | 14 | 18 |

The intensity of each diffracted order can be calculated with various power formulas that depend on the incident beam power, incident beam wavelength and amplitude of the sinusoidal grating. For normal incidence, low-angle scatter and a smooth surface ( $a/\lambda \ll I$ ), the power of each order is calculated with

$$P_n \approx \left[ J_n \left( \frac{2\pi a}{\lambda} \right) \right]^2 \quad (4-8)$$

where  $P_n$  is the power of each diffraction order,  $J_n$  are Bessel Functions of the first kind,  $a$  is sinusoid amplitude and  $\lambda$  is the incident beam wavelength. Conservation of energy is observed because the sum of squared Bessel functions over  $n$  from minus infinity to positive infinity is one. For high angle scatter and non-normal incidence, scatter intensity becomes dependant on polarization in addition to incident power, wavelength and sinusoid amplitude [27]. The equations that describe high angle, non-normal incidence

converge to a result equal to the equation for normal incidence and low angle scatter (Equation 4-8). Both methods of calculating scatter power depend on the grating equation (Equation 4-7) to determine the position of each scatter order and surface roughness to determine intensity. Section 4.4 examines optimization of the scatter pattern while keeping increases to surface roughness to a minimum.

Statistical tools commonly used for evaluation of precision surfaces with respect to frequency content and power are the Autocovariance Function and Power Spectral Density (PSD). Autocovariance of a surface profile is used for analysis of the regularly spaced features in a diamond turned surface because it gives a good indication of the agreement between similar surface features as discussed in the next section. The PSD function is useful to characterize a surface with multiple spatial frequencies as it calculates power for each spatial frequency; the underlying theories of this function are thoroughly discussed in the literature [16, 27].

A PSD plot of a surface is found through use of a Fast Fourier Transform (FFT). The relationship between the surface profile, autocovariance, and PSD is determined by various implementations of the FFT [16]. PSD can be calculated by squaring the FFT of the surface profile or by calculating the FFT of the autocovariance of a surface profile. Figure 4-40 shows the surface profile of an ideal diamond turned surface with perfect circular cusps, Figure 4-41 shows the autocovariance of that surface (oscillations indicated correlations in features along surface) and Figure 4-42 shows the PSD of that surface with respect to spatial frequency (inverse of wavelength) with peaks from

harmonics to right of  $0.2 \text{ } 1/\mu\text{m}$ . The cusp-to-cusp intersection of the  $5 \text{ } \mu\text{m}/\text{rev}$  feed rate differs greatly from a sinusoidal profile thus, higher frequency harmonics appear in the PSD that represent the sharp peaks at cusp intersections. These harmonics are effectively higher frequency sinusoids that cause modes of diffraction for all wavelengths in the white light spectrum. The lowest frequency in a Fourier transform of ideal cusps is the cross-feed rate and the higher frequency harmonics will produce diffraction modes along the same angles as the fundamental cross-feed. The value corresponding to a wavelength of zero (the DC component in frequency spectrum terminology) is at very low power because the mean of the cusp height was almost zero when the PSD was calculated.

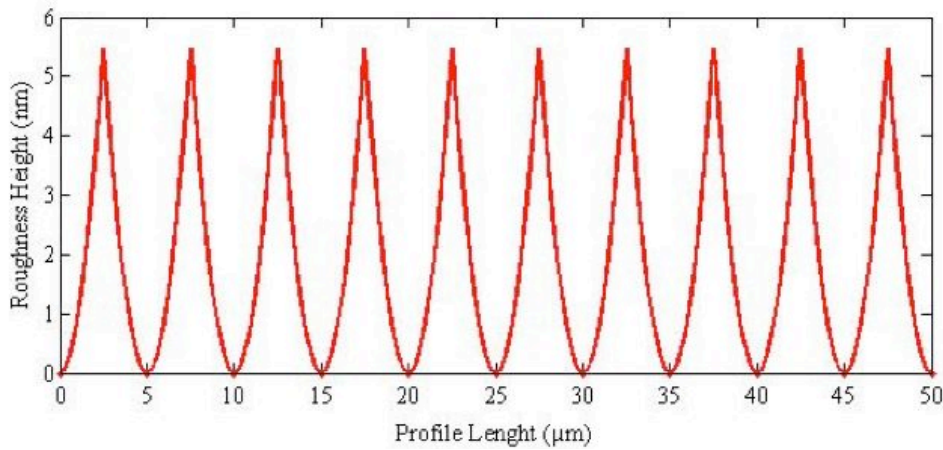


**Figure 4-40:** Surface profile of perfect diamond turned cusps.  $f = 5 \text{ } \mu\text{m}/\text{rev}$ ,  $R = 570 \mu\text{m}$ , PV = 5.4 nm and RMS = 1.6 nm.

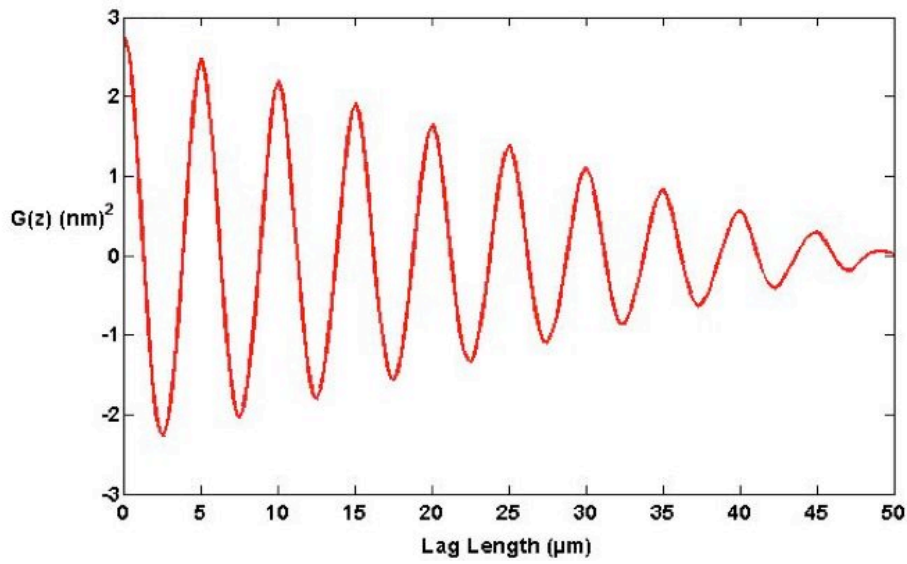


**Figure 4-41:** Autocovariance for surface in Figure 4-40.

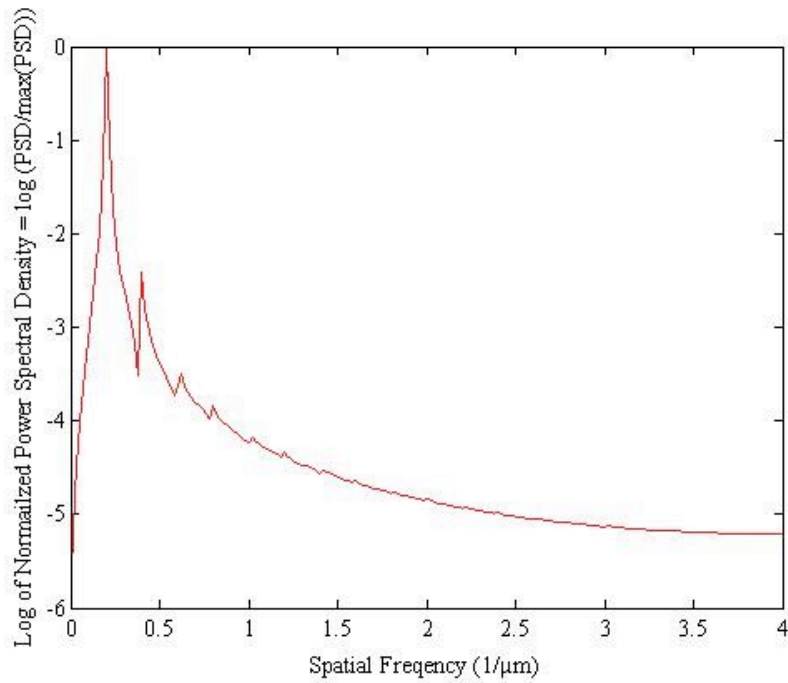


**Figure 4-42:** Log of PSD normalized for the maximum peak from autocovariance in 4-41. First peak is at 0.2 features/ $\mu\text{m}$  or 5  $\mu\text{m}/\text{feature}$ .

The scatter patterns formed by ideal diamond turned cusps and other surfaces are in Figure 4-43. Figure 4-43a shows the reflected beam from a perfect surface with no scatter and Figure 4-43b shows scatter from a perfect sinusoidal grating as predicted by Equation 4-7. For a surface with perfect diamond turned cusps, Figure 4-43c shows the scatter pattern from the Fourier transform of the cusps. There are discrete points in the pattern along the  $X_o$  axis that are created by the harmonics found from a Fourier transform of ideal cusps. As seen in the PSD plot, the powers of the harmonics decrease as spatial frequency increases. Figures 4-43d shows a scatter pattern from a surface with an arbitrary one-dimensional random frequency content (no pattern). The random frequency content could represent cusp-to-cusp variations caused by machine vibrations. Figure 4-43e shows an isotropic surface that contains all frequencies and demonstrates no pattern in any direction. This could represent a high quality ground and polished surface with an absence of periodicity from grinding wheel feed rate. Finally, Figure 4-43f shows the scatter pattern found on a real, diamond turned surface which is a combination of 4-43c, d and e.

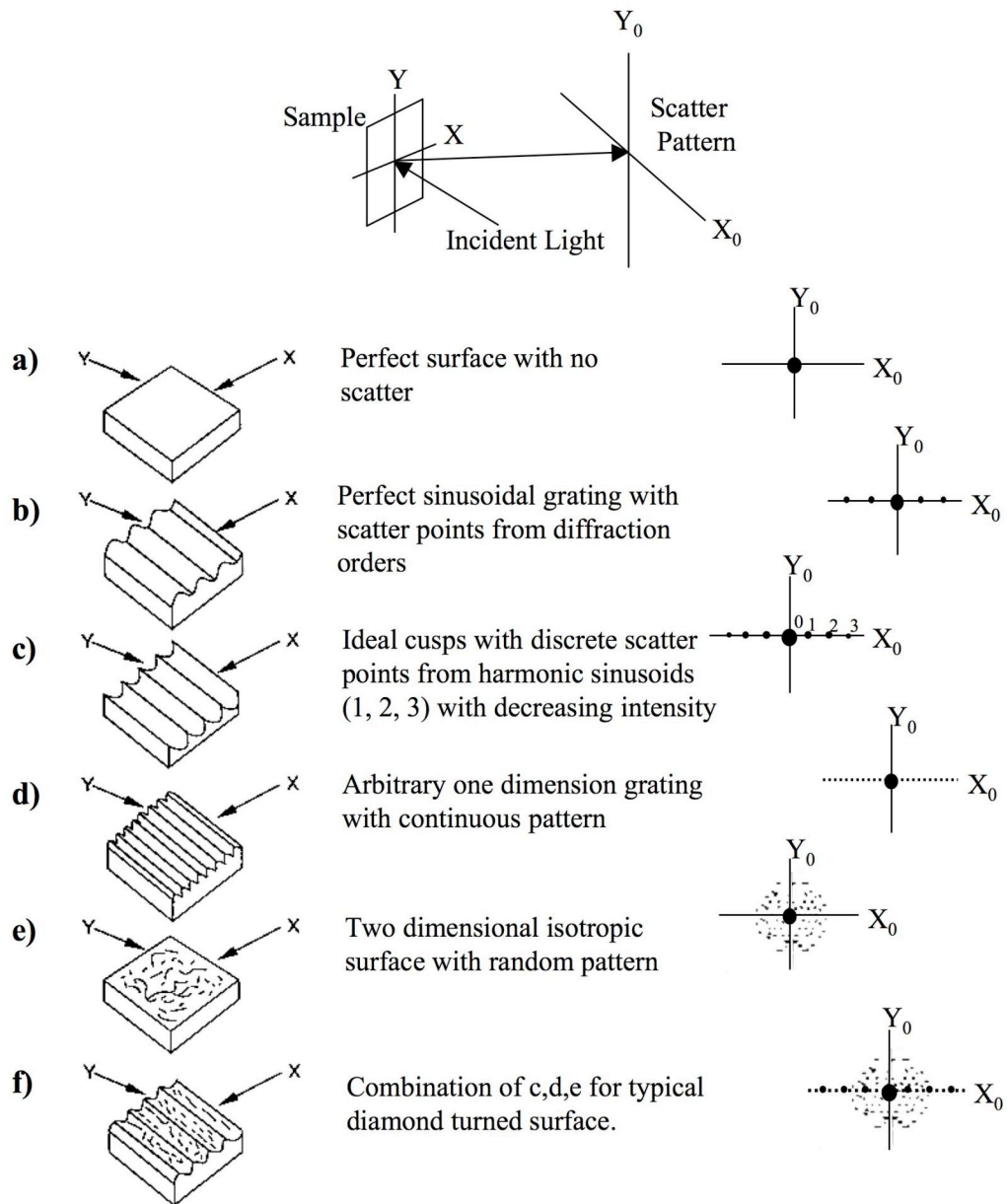


**Figure 4-43:** Scatter patterns for various surface profiles.

#### *4.4.2 Cross Feed Dither Model*

With the knowledge that a diamond turned surface has residual cusps left by a round-nose tool, a model was created to reduce the regularity of the cusp spacing by dithering the tool in the cross feed direction. Randomizing the cusp spacing would eliminate the discrete scatter points seen in the scatter pattern of Figure 4-43c and produce a continuous pattern of lower intensity seen in Figure 4-43d. For medium to high feed rates ( $3.65 \mu\text{m/rev}$  and  $11.5 \mu\text{m/rev}$ ) were the regular cusp spacing seen in Figure 4-43c is evident (Section 4.3.3.1), the spacing could be randomized into an arbitrary one-dimensional grating as seen in Figure 4-43d. For low feed rates ( $1.16 \mu\text{m/rev}$ ) where the cross feed is not evident, assuming the tool edge radius was sharp and the edge quality was perfect, the random one-dimensional contribution in Figure 4-43d was introduced by machine vibration and could be optimized by manipulating the cross feed spacing of the cusps.

The Z-axis vertical vibration model in Section 4.3.2 was expanded to accommodate varying the movement of the tool in the X-direction (cross feed). The spacing of each cross feed was moved from its evenly spaced X-coordinate in a positive or negative direction. Figure 4-44 shows the center of each cross feed with a crosshair and resultant surface trace without the effects of Z-axis vibration. While the height of each apex is at zero, the cross feed is no longer periodic and the residual cusps are no longer uniform heights and widths. The assumptions in this model were the same as with the vibration model: ideal cusps created with a sharp tool and a homogenous material compatible with

diamond turning. Figure 4-44 also demonstrates that any change from perfectly spaced cusps when using a round nose tool will increase the theoretical surface roughness; the theoretical PV without dither is 5.5 nm and RMS is 1.6 nm compared to the 10 nm PV and the 2.4 nm RMS from the model.

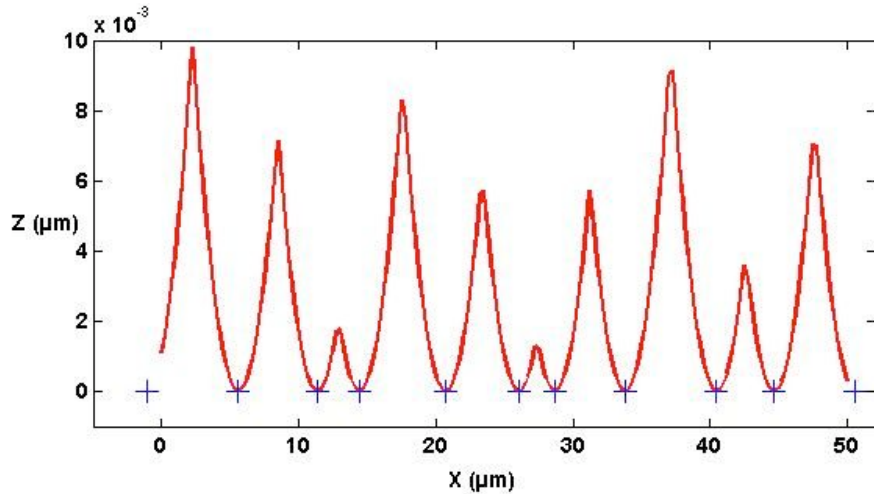


**Figure 4-44:** Example of dither concept (without machine vibration disturbing the cusps in the Z-direction) showing apex of tool (+) moved from regularly spaced intervals (cross-feed) and resultant contour of circular cusps. A 570  $\mu\text{m}$  nose radius tool was used with a 5  $\mu\text{m}/\text{rev}$  cross feed.  $PV = 10 \text{ nm}$  and  $RMS = 2.4 \text{ nm}$ .

Realizing that change from evenly spaced cusps increases roughness, the dithering amplitude must be selected so the cross-feed cusp spacing is only changed enough to randomize periodicity. A Gaussian distribution was selected for generating the cross-feed variations. Several standard deviations ( $\sigma$ ) and cross-feed rates were modeled.

Standard deviation was calculated using +/-  $3\sigma$  distributions with a spreads equal to half, once, and twice the cross feed rate. Because cross-feed dithering has a negative effect on surface finish, dithering rates were kept low enough that individual grooves show little variation in the up-feed direction for surface profile of typical length and width. A 3D profile with dithering and machine vibration is shown in Figure 4-45. Its appearance is very similar to a surface with vibration only as seen in Figure 4-26.

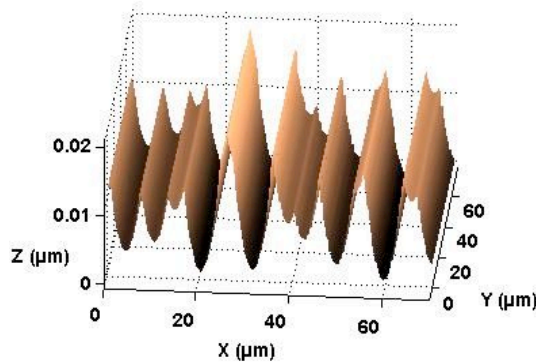


**Figure 4-45:** Sample 3D surface profile with cross feed dithering (motion along the X-axis) and Z-axis machine vibration.

#### 4.4.3 Analytical Model Analysis

To evaluate the spatial repetitiveness of the surface, the autocovariance function [16] was applied to each trace generated by the model (vibration was included with cross-feed dither profiles as discussed later in this section). It was selected because it is an excellent indicator of repeated features in the surface and an “enveloping” function can be used to evaluate amplitude decay seen in Figure 4-47. PSD was not used because secondary

surface finish effects introduce random peaks that dominate measurement, especially at lower feed rates. Also, the PSD of diamond turned cusps shows higher frequency harmonics due to cusp intersections, which obscures evaluation of cusp spacing that has been randomized.

As discussed in Section 4.3, when cutting at low feed rates (about  $f = 5 \mu\text{m}/\text{rev}$  and lower) Z-axis machine vibration results in several tool passes being absent from the surface profile. To make sure that the profiles modeled at low feed rates with cross-feed dithering and machine vibration contained adequate information for analysis, the number of tool passes was increased to 40 and the number of points in the profile was increased to 401. For conceptual illustration, examples in this section (4.4.3) with no cross-feed dither and no machine vibration only used 10 passes and 5  $\mu\text{m}/\text{rev}$  feed rate.

The autocovariance function ( $G(z)$ ) is the product of two copies of the same surface contour as one is shifted (lag length) relative to the other. The formula for autocovariance of a data set with discrete points is found in this equation:

$$G(l) = \frac{1}{N} \sum_{i=1}^{N-l} z_i \cdot z_{i+l} \quad l = 0, 1, 2, \dots, N-1 \quad (4-9)$$

where  $l$  is the integer corresponding to lag length,  $N$  is the total number of data points in the data set, and  $z$  is a point in the data set. It has units of height squared and the first point, where the lag length equals zero ( $G(0)$ ), is the square of RMS roughness. Lag increments are equal to the spacing between data points or samples. It is important that

the profile be quantized at a constant sample rate with no jitter. A highly positive value of  $G(z)$  at a certain lag length will indicate that the surface has correlating features for that length. Also, the mean of the surface contour must be zero for the first point in the Autocovariance ( $G(0)$ ) to equal the square of RMS roughness.

When a surface with ideal cusp spacing and uniform height seen in Figure 4-46 (repeat of Figure 4-44) is evaluated with the autocovariance function the evenly spaced cusps will alternate between positive (peak aligned to peak) and negative (peak aligned to trough) as seen in Figure 4-47 (repeat of Figure 4-41). For reference, a perfectly flat surface will result in a straight line along  $G(z) = 0$ . A random, isotropic surface with a Gaussian distribution, such as Figure 4-42e, starts at  $G(0) = \text{RMS}^2$ , decays immediately to  $G(z) = 0$ , and randomly oscillates about  $G(z) = 0$  through the remaining lag length. A single-point diamond turned surface cannot achieve this randomness because the tool will always leave up-feed features.

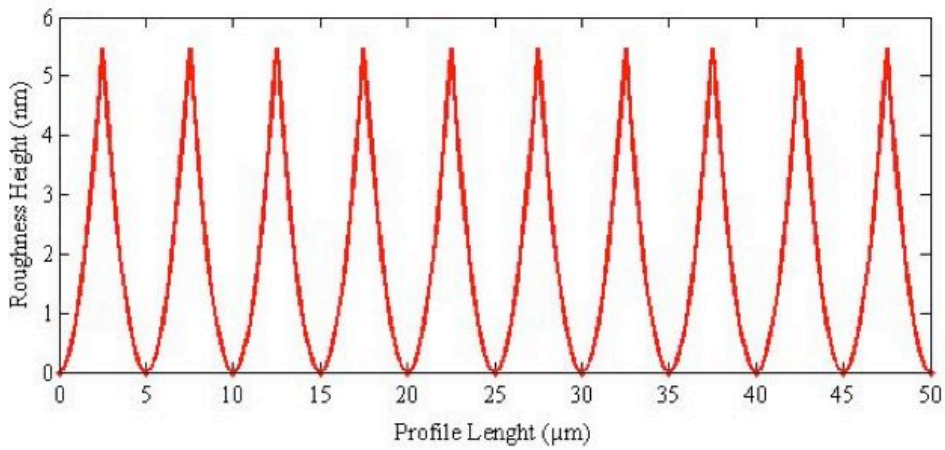


**Figure 4-46:** Surface Profile for autocovariance seen in Figure 4-47.  $f = 5 \mu\text{m/rev}$  and  $R = 570 \mu\text{m}$ .

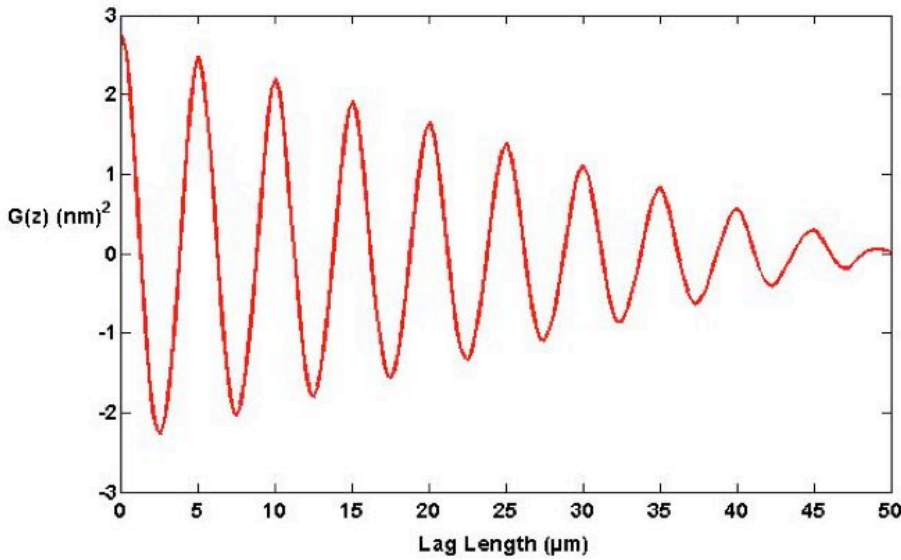


**Figure 4-47:** Autocovariance of theoretical profile in Figure 4-43 where  $f=5 \text{ } \mu\text{m/rev}$ ,  $R = 570 \text{ } \mu\text{m}$ ,  $PV=5.5 \text{ nm}$ ,  $RMS = 1.6 \text{ nm}$ ,  $G(0) = RMS^2 = 2.56 \text{ nm}^2$ .

The Hilbert ( $H(z)$ ) [17] transform enables computation of the instantaneous amplitude of an oscillating function for a surface with periodic features, which is useful to characterize the decreasing amplitude of the autocovariance seen in Figure 4-47. The Hilbert transform is often used to evaluate the exponential decay terms found in a sinusoidal decay. A common example of sinusoidal decay is the impulse response of an under-damped spring-mass-damper system. Table 4-3 gives Hilbert Transforms for common functions. Of particular interest is  $H(\sin(x)) = \cos(x)$ , which means the Hilbert function returns a  $90^\circ$  phase shift. The sum of squares of the two values will give the amplitude of the sinusoid.

**Table 4-3:** Hilbert Transforms [36].

| Function            | Hilbert Transform     |
|---------------------|-----------------------|
| $\sin(x)$           | $\cos(x)$             |
| $\cos(x)$           | $-\sin(x)$            |
| $\frac{\sin(x)}{x}$ | $\frac{\cos(x)-1}{x}$ |
| $\frac{1}{1+x^2}$   | $-\frac{x}{1+x^2}$    |

The decrease in amplitude of an autocovariance function with lag length provides a measure of the regularity (or irregularity) of the feature spacing in a surface profile. A quick decrease in amplitude indicates the surface has randomized features. A slow decrease in the autocovariance amplitude indicates a surface with many highly repetitive features that are evenly spaced.

For ideal diamond turned cusps, the decrease in autocovariance amplitude was best described by a negatively sloped line. The Hilbert transform of the autocovariance was normalized and fit with a linear regression:

$$H(z)_{normalized} = m * l + b \quad (4-10)$$

where  $b$  is the y-axis intercept,  $m$  is the line slope, and  $l$  is lag length. A Hilbert transform of the autocovariance function seen in Figure 4-47 is found in Figure 4-48 where the dotted line is the autocovariance, the solid line is the normalized Hilbert transform result

and the dashed line is the line fit. The slightly jagged path of the Hilbert transform indicates that the autocovariance of ideal diamond turned cusps does not perfectly match a sinusoidal decay. This is caused by sharp peaks at cusp-to-cusp intersections. Also, the small initial decline at the beginning of the Hilbert transform is caused by the first point of an autocovariance equaling the square of RMS surface finish ( $G(0) = \text{RMS}^2$ ) rather than zero, like that of a under-damped system.

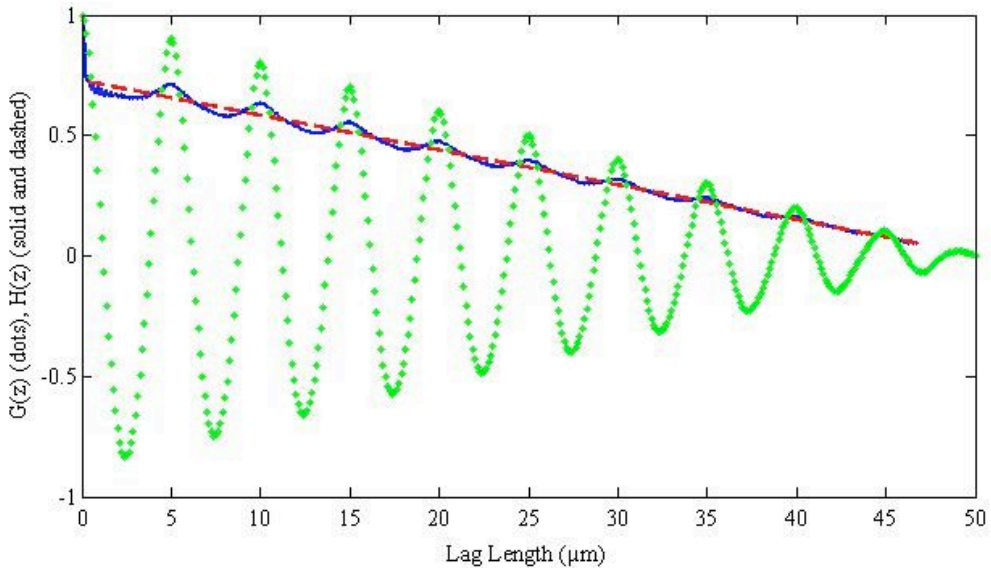


**Figure 4-48:** Autocovariance (dots), Hilbert transform (solid) and exponential decay fit (dashed) of Figure 4-47.

Surface profiles were modeled with the machine vibration discussed in Section 4.3 (Z-axis = 63.6 Hz & 11 nm amplitude). Varying levels of cross-feed dither ( $\pm 3\sigma = 0.5x$ , 1x and 2x cross-feed), were tested on low, medium and high feed rates (1.16, 3.65 and 11.55  $\mu\text{m}/\text{rev}$  respectively). The value of the y-axis intercept ( $b$ ) varied significantly as

the dither was for all feed rates. Also,  $b$  was found to best represent how quickly the autocovariance amplitude initially drops towards and oscillates about zero. Thus, smaller values of  $b$  indicated quick initial decays and improved surfaces that have lessened correlation of cusp spacing. The slope ( $m$ ) was largely similar for each cross feed. It became less negative (flatter) as dither amplitude increased, which supports the y-axis intercept being the best representation of initial autocovariance amplitude drop and less regular surface patterns. Figure 4-49a and 4-49b show examples of the fit for the 11.55  $\mu\text{m}/\text{rev}$  feed rate with no dither and 1x cross-feed dither, respectively.

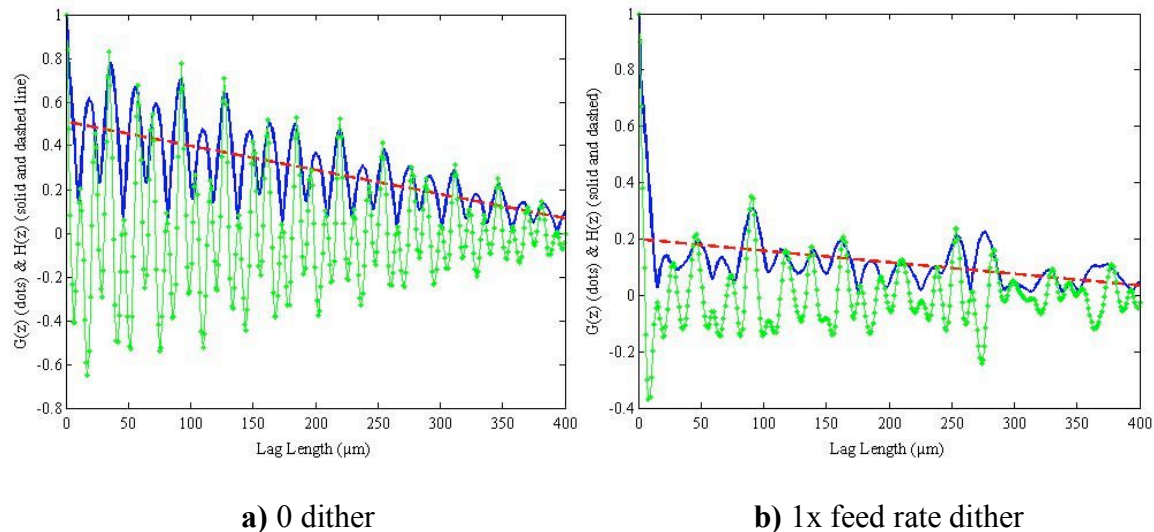


**Figure 4-49:** Dither examples for the 11.55  $\mu\text{m}/\text{rev}$  feed rate. Machine vibration is included (11 nm amplitude at 63.6 Hz).

The amplitude decreases (reduced cusp spacing regularity) discussed above must be evaluated while taking the RMS surface finish in consideration. Dithering can reduce

spatial periodicity but the resulting cross-feed variations can cause the RMS roughness to exceed optical surface quality.

#### *4.4.4 Predicted Machining Conditions*

By dithering the cross feed motion with a Gaussian distribution while modeling surface finish with influences of machine vibration, the periodicity of the tool cusps was reduced for small feed rates while causing only a small increase in RMS roughness. The y-axis intercept ( $b$ ) is shown with respect to the dither amplitude factor (\* feed rate) in Figure 4-50 for three feed rates. Lower values of  $b$  are surfaces that have less correlation of cusp spacing. The increase in RMS roughness for three feed rates is shown in Figure 4-51 for the same surface contours and dither amplitudes.

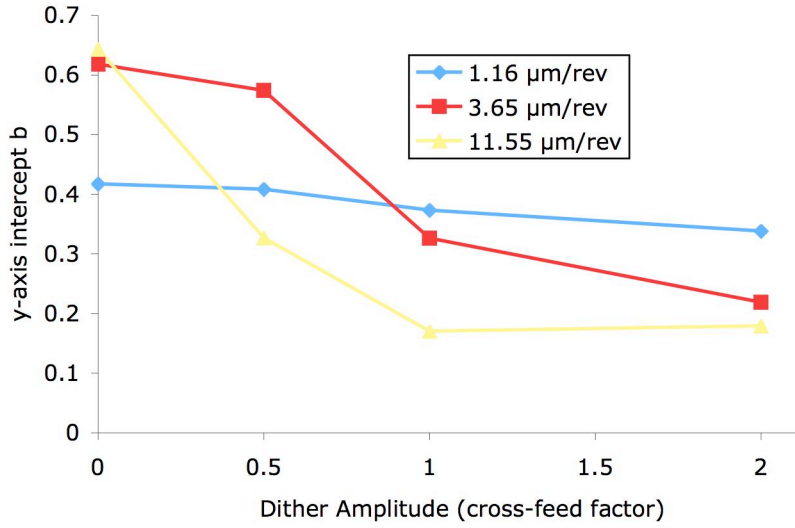


**Figure 4-50:** y-axis intercepts ( $b$ ) vs dither amplitude with machine vibration present.

Lower values of  $b$  indicate less surface agreement. Same modeled cutting conditions are shown below in Figure 4-51.

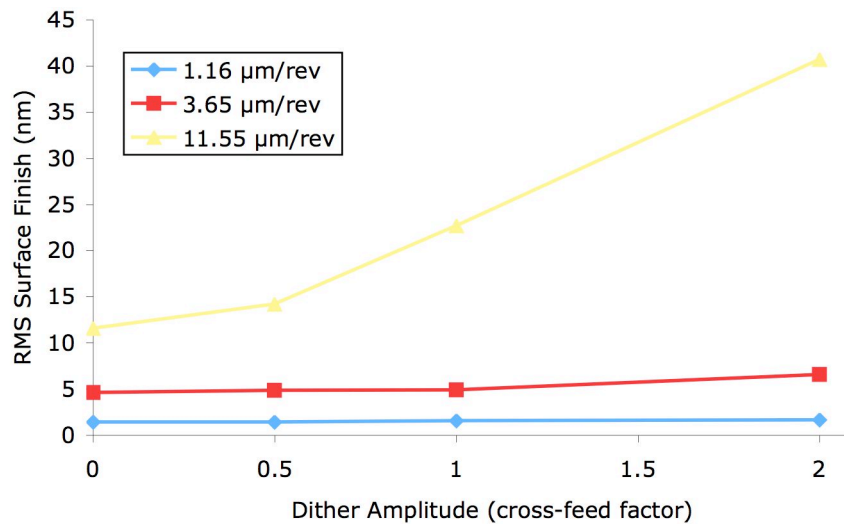


**Figure 4-51:** RMS Surface Finish vs Dither amplitude for three cross feed rates ( $\mu\text{m}/\text{rev}$ )

with machine vibration present. Same modeled cutting conditions used above in Figure 4-50.

The RMS roughnesses at smaller cross-feeds appear less influenced by the dithering; this is a result of the several tool passes not being represented in the final surface profile because of vibration. The larger cross-feeds show the largest reduction in cusp periodicity but have a sharp increase in RMS roughness. Also, the y-axis intercept  $b$  shows a minimum as dither amplitude is increased where the optimal is equal to one cross-feed. This is caused by large cross-feed excursions of the tool at the higher dither amplitude which leaves several large cusps in the profile. The repeated large cusps increase the spacing regularity.

#### *4.4.5 Scatter Measurements of a First Surface Mirror and Diamond Turned*

##### *Grooves without Cross Feed Dither*

To set the baseline for predicted machining conditions, scatter patterns images were taken from the electroplated copper sample cut for the machine vibration experiments. For an additional reference, the scatter pattern from first-surface glass mirror was measured. The RMS roughness of the mirrored glass, over a similar area as the roughness measurements of the machine vibration workpiece, was about 0.5 nm. A length measuring laser interferometer (the same unit was used to measure the sphere radius in Section 3.4) was used as the laser source along with three fold mirrors, two beam apertures and a optical rail; which is seen in Figure 4-52. Figure 4-53 shows an alternate view of two paper pinhole apertures. Because the laser was aligned to the GPI, the fold

mirrors were used to redirect the beam such that it ran parallel with the threaded holes in the optical table used to mount the optical rail. The vibration experiment workpiece had 7 adjacent 2 mm wide bands cut in the face with different feed rate used for each band so the beam size was reduced with a pinhole aperture in heavy paper. The pin used to make the final aperture was 1.05 mm in diameter so the beam was incident to a single feed rate while exposing a adequate number of grooves to diffract the beam into a scatter pattern. An intermediate aperture of slightly larger diameter was used to block light scattered from the fold mirrors and reduce the size of the beam incident on the final aperture.

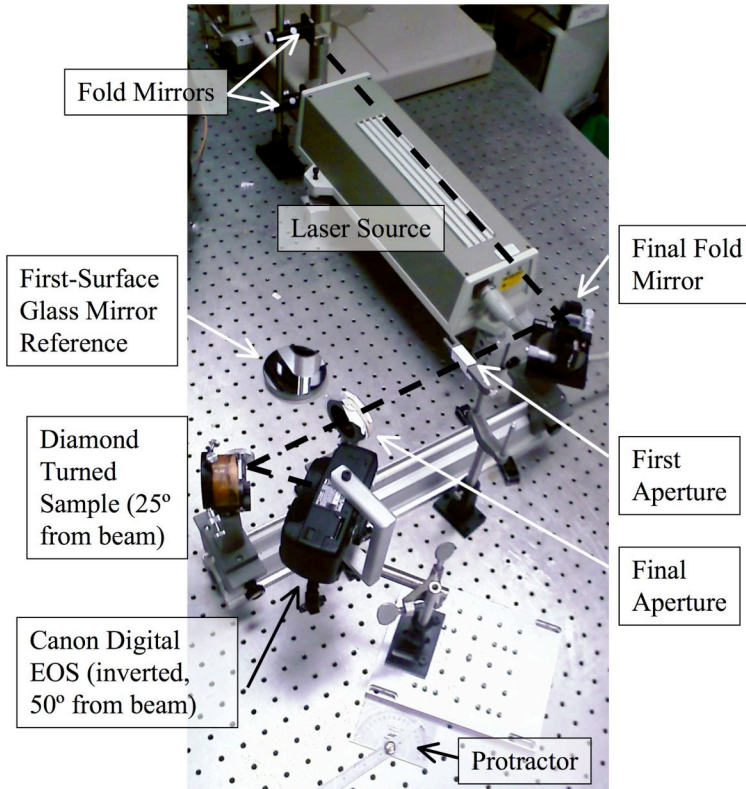


**Figure 4-52:** Scatter pattern measurement setup. Dashed line shows beam path. The mirrored glass reference is lying beside the optical setup. The final fold mirror, pinhole apertures and the diamond turned sample are mounted on the optical rail.

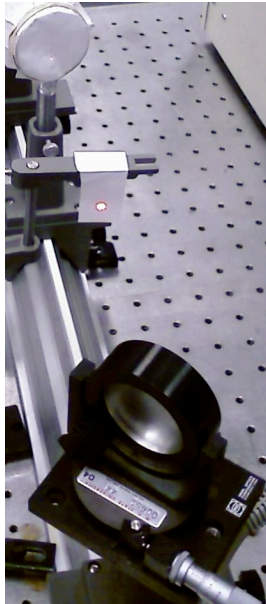


**Figure 4-53:** Alternate view of paper pinhole apertures. From foreground to background: final fold mirror, first aperture and final aperture. The large dot on the first aperture represents a beam diameter of about 4 mm.

The surface normal of the test mirror was set  $25^\circ$  from the incident beam so the detector body (Canon Digital EOS Rebel XT) would not obstruct the beam while keeping the detector close enough to capture the first few scatter modes. The detector (22.8 mm wide by 14.8 mm tall) was set normal to the reflected beam about 80 mm from the sample surface. This would allow modes below about  $8^\circ$  from the reflected beam to be captured. The angular positions were measured with a protractor ( $1^\circ$  graduations) relative to the optical table holes. To capture relatively low intensity scatter pattern, the detector shutter speed was set to 1/60 sec. with the detector sensitivity set at ISO 100. At this slower shutter speed, the reflected beam and higher intensity modes appear saturated.

To measure the different feed rates, both the sample and the detector were repositioned. The fixture holding the sample had a linear slide that would allow movement in the surface normal direction. Because the surface normal was 25° from the incident beam, translating the sample in the surface normal direction caused the incident beam to move across the surface of the sample. The height of the sample was set so the incident beam moved across the diameter from the sample centerline to the edge in the cross-feed direction. The detector was repositioned for each measurement to avoid blocking the incident beam and to center the reflected beam. The protractor was used to verify the reflected beam was normal to detector plane.

The scatter patterns from the mirrored glass and all seven cross-feeds are in Figure 4-54. The mirrored glass pattern in Figure 4-54a shows the best possible scatter pattern so the scatter contribution from the diamond turned surfaces added to that pattern. The pattern seen here is a result of using paper for the final aperture because the edge of the hole was not sharp; several metal foil apertures were attempted but the foil would tear when the hole was cut.. Figure 4-54b (35.8  $\mu\text{m}/\text{rev}$ ) shows one more scatter mode on the left than on the right because the detector width was too small to capture the 7<sup>th</sup> mode on both sides of the reflected beam. Also, the detector width was too small to simultaneously capture both sides of the 1<sup>st</sup> mode for 4-54f, (3.58  $\mu\text{m}/\text{rev}$ ) so the reflected beam was moved to the edge of the detector to capture one of the 1<sup>st</sup> modes. For the final two measurements in Figures 4-54g and 4-54h, no modes were detected so only the reflected beam is shown. The scatter modes to the right of the reflected beam have lower intensity than the modes to the left because the incident beam is not normal to the surface;

calculation of power with non-normal incidence is discussed in Section 4.4.1. This variation in intensity across a scatter pattern is inconsequential for pattern observation because the mode locations relative to the reflected beam are insensitive to non-normal incidence, which is also discussed in Section 4.4.1.

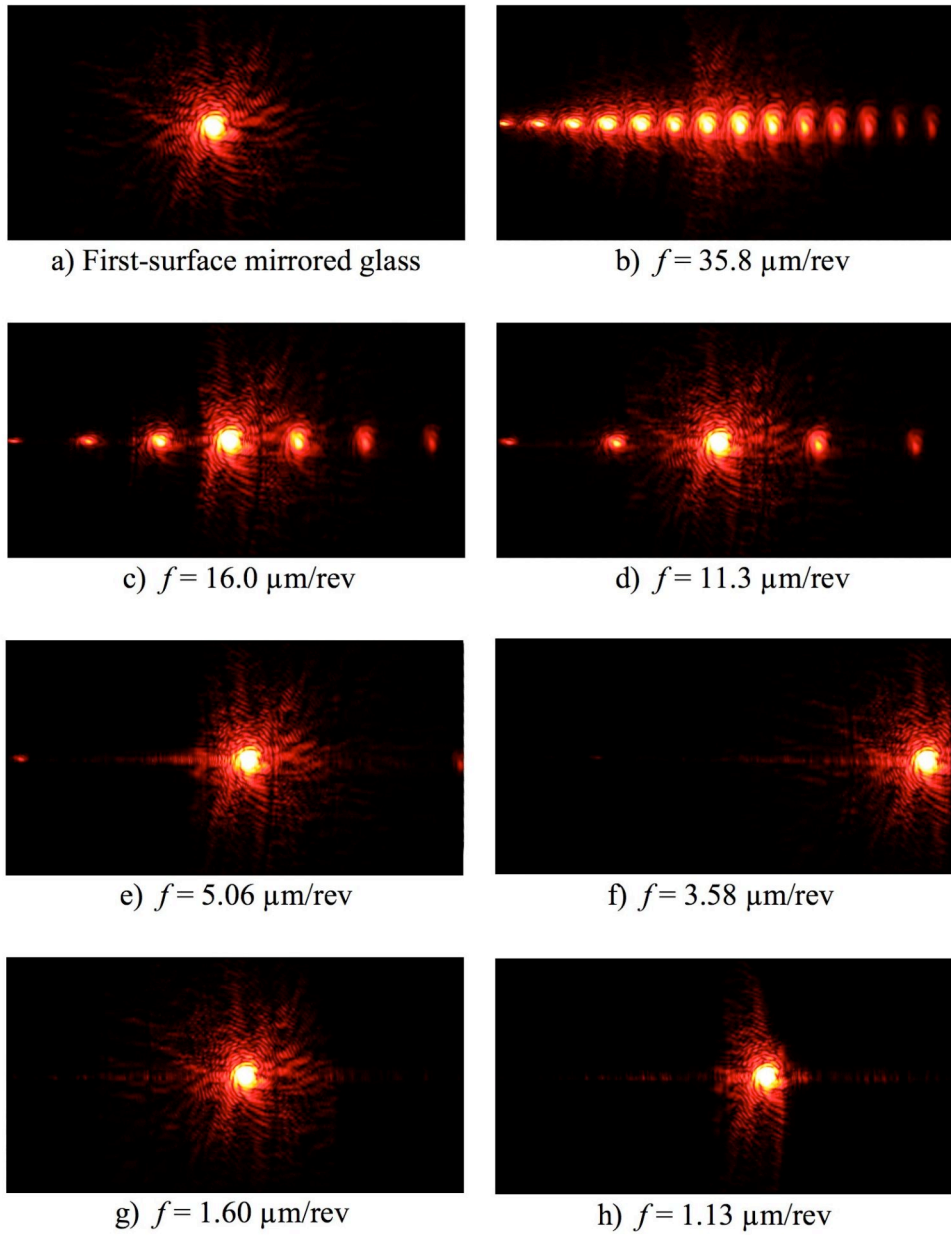


**Figure 4-54:** Diffraction patterns for mirrored glass and 7 feed rates diamond turned in electroplated copper. In Figure 4-54b, the detector width and position allowed room for one more mode to the left of center. In Figure 4-54f, the reflected beam is off center to observe the first mode that was outside the detector when centered.

**Table 4-4:** Expected Modes in the Scatter Images found in Figure 4-54.

| Cross Feed Rate ( $\mu\text{m}/\text{rev}$ ) | Figure | Number of Modes: Detector Centered on Reflected Beam (+/- 8°) |
|--|--------|---|
| 35.8   | 4-54b  | +/- 7   |
| 16.0   | 4-54c  | +/- 3   |
| 11.3   | 4-54d  | +/- 2   |
| 5.06   | 4-54e  | +/- 1   |
| 3.58   | 4-54f  | 0 (1 <sup>st</sup> mode: 10.2°)                               |
| 1.60   | 4-54g  | 0 (1 <sup>st</sup> mode: 23.3°)                               |
| 1.13   | 4-54h  | 0 (1 <sup>st</sup> mode: 34.1°)                               |

As predicted by the diffraction grating formula in Equation 4-4, the spacing of the scatter modes becomes larger as the spatial frequency increases (groove spacing decreases) in Figures 4-54b to 4-54f. Table 4-4 indicates that +/- 7 modes should be seen in Figure 4-54b while only 6 are seen on the right side. This is a result of detector placement: the camera body was interfering with the incident beam. Table 4-4 indicates that the 1<sup>st</sup> mode of Figure 4-54f (3.58  $\mu\text{m}/\text{rev}$ ) is 10.2° which supports the need to move the reflected beam off-center to capture this mode. Scatter modes representative of a surface with regularly spaced features were absent from the reflected beam in the 1.6  $\mu\text{m}/\text{rev}$  and 1.13  $\mu\text{m}/\text{rev}$  feeds seen in Figures 4-54g and 4-54h. The detector was reposition several times in an attempt to find the 1<sup>st</sup> mode but it was not found. All diamond turned scatter measurements show a faint line that is parallel with the cross-feed direction and extends from the reflected beam. This line matches the pattern for a random grating as discussed in Section 4.4.1 and seen in Figure 4-43d, which is the best possible result for a surface with up-feed features.

#### *4.4.6 Conclusions*

Through modeling and analysis, it was theorized that cross feed tool dithering can randomize the regularly spaced grooves formed in diamond turning that cause the surface to act like a diffraction grating. A surface with randomized cusp spacing would produce a diffraction pattern where the undesirable diffraction structure (Figure 4-42c) is absent and only a faint line that is parallel to the cross-feed direction would appear (Figure 4-42d). However, during scatter pattern measurement of the diamond turned surface cut for the machine vibration section, this effect was observed (Figures 4-53g, 4-53h) at low cross-feeds ( $f = 1.13, 1.6 \mu\text{m}/\text{rev}$ ) where not all tool passes are represented in the final surface (Figures 4-31, 4-32, 4-33). In effect, machine vibration causes surfaces with low cross-feeds, where optical quality surface roughness is achieved, to demonstrate randomized grating properties. Cross feed dither at these feed rates would only increase surface roughness.

Cross feed dithering at higher cross feeds could randomize the diamond turned cusp spacing, but the higher RMS roughness found at these feed rates would increase the magnitude of the random scatter along the cross feed direction, thus making them unsuitable for imaging systems.

## 5 CONCLUSIONS AND FUTURE WORK

### 5.1 FORM FIDELITY

The study of diamond turning for fabricating optical and fiducial surfaces is an important area of research related to the production of high-quality optical systems for civilian and military applications. Discussion of form fidelity included the generation of the hyperbolic mirrors for the Ritchey-Chrétien telescope as well as the general capability of the ASG diamond turning machine to generate optical quality surfaces.

#### *5.1.1 Hyperbolic Mirrors and Fiducial Features*

The steps needed to create the hyperbolic optical surfaces are described as well as the related fiducial surfaces that dictate the spacing of the mirrors.

- The optical and fiducial surfaces were cut with separate tools that were simultaneously aligned to the X, Y and Z-axes.
- Whole components were cut in a single part chucking so optical surface and fiducial alignment distances were preserved.
- The primary mirror contained axisymmetric from uncorrected DTM error shapes.
- The primary contained non-rotationally symmetric errors from rough machining that were not correct by diamond turning because of its high aspect ratio (diameter to thickness).

### *5.1.2 Flat and Spherical Surfaces*

A number of 100 mm diameter flats were diamond-turned on the ASG- 2500.

- All linear traces of the surface fall below  $\lambda/4$  and often fall below  $\lambda/5$  (127 nm).
- The NRS error of the flats was between 30 and 80 nm because the aspect ratio was high enough to resist vacuum chuck distortion forces.
- These surface meet the Rayleigh limit for optics that have diffraction-limited performance, and are suitable for optical systems.

Automatic error correction is imperative for fabrication of high-fidelity mirrors.

- Squareness error between axes was the dominating form error.
- The squareness error was found experimentally and it was corrected with an automatic compensation routine that was previously programmed into the motion controller.

The consistency in the results above was not achieved until thermal influences were observed.

- “Warm up” of the spindle must be completed prior to optical surface machining.
- Utilization of thermally isolating gloves, minimal work piece contact and tightly controlled environment with constant temperature monitoring are critical.

Using the automatic error correction that yielded high-fidelity flats allowed the fabrication of a high-fidelity large-aperture sphere.

- The form error measured in a trace across the sphere was  $\lambda/4$  (158 nm).
- The measured sphere radius error was less than  $6 \mu\text{m}$ , which was observed as the repeatability of the length measuring laser interferometer fit to the GPI translating stage.
- The ASG-2500 can fabricating aspheric surfaces for use in optical systems.

For future diamond turning applications:

- Chuck flatness need be verified
- A best fit sphere should be cut and measured before the final asphere is cut
- The chucking surface should have a low aspect ratio (thickness to diameter)

## 5.2 SURFACE FINISH

### 5.2.1 *PV Approximation Regime Test with Servo*

Experiments were conducted to verify surface finish in a regime where the parabolic approximation would predict roughness.

- Results exhibited little to indicate that finish is affected by changes in depth of cut or surface speed.
- Cross-feed rate predicted surface roughness closely at large cross-feeds.
- Minimum chip thickness and asynchronous spindle motion effects became dominant as cross-feed was reduced.
- Spacing of the tool passes matched the programmed cross-feed rate.

- Tool edge quality is extremely important as nicks can easily produce defects many nanometers in size.

### *5.2.2 Machine Vibration*

The conventional wisdom that there is little merit in machining at feed rates where the measured surface finish is worse than the theoretical finish simply does not hold.

- At small cross-feeds, many tool passes are not represented in the surface profile.
- Finer feed rates continue to reduce RMS roughness below the amplitude of machine vibration.
- Material properties, tool edge quality and tool edge sharpness become dominate factors at RMS roughness below 2 nm in electroplated copper.
- For optical systems fabricated with 6061-T6 aluminum alloy, use of a pure aluminum coating such as Alumiplate® will achieve finishes similar to those discussed in this thesis using electroplated copper.

### *5.2.3 Cross-feed Tool Dithering*

Through modeling and analysis, it was theorized that cross feed tool dithering can randomize the regularly spaced grooves formed in diamond turning that cause the surface to act like a diffraction grating.

- A surface with randomized cusp spacing would produce a scatter pattern where the undesirable scatter structure (Figure 4-42c) is absent and only a faint line that is parallel to the cross-feed direction would appear (Figure 4-42d).
- Analytic model analysis showed cross-feed dithering would randomize groove spacing but increase RMS roughness.
- Scatter pattern measurement of the vibration experiment workpiece showed randomization at low cross-feeds where all tool passes were not represented in the final surface.
- Machine vibration causes surfaces with low cross-feeds, where optical quality surface roughness is achieved, to demonstrate randomized grating properties.

## **REFERENCES**

- 1 Dow, T.A., R. Woodside. Metrology for Reflective Optical Systems. Precision Engineering Center 2005 Annual Report, 23, 169-197, (2006).
- 2 Grechman, M.C., Optical Tolerancing for Diamond-Turning Ogive Error. Proceedings of SPIE: Reflective Optics II, Vol. 1113, 224-230, (1989).
- 3 Miller, M.H. and T.A. Dow. Enhancements to Three Axis DTM Controller. Precision Engineer Center 1991 Annual Report, 9, 265-278, (1991).
- 4 Moorefield II, G.M. and T.A. Dow. Error Budget for Diamond Turning Machine. Precision Engineering Center 1989 Annual Report, 7, 65-70, (1989).
- 5 Moorefield II, G.M. and T.A. Dow. Error Budget for Diamond Turning Machine. Precision Engineering Center 1990 Annual Report, 8, 239-261, (1990).
- 6 Dow, T.A. and A. Sohn. Course Notes: Metrology in Precision Manufacturing. Precision Engineering Center, North Carolina State University, Spring 2005.
- 7 Hubbel, P., G.M. Moorefield II and T.A. Dow. DTM Metrology. Precision Engineering Center 1991 Annual Report, 9, 83-107, (1991).

- 8 Drescher, J. and T. Dow. Tool Force and Surface Finish Aspects in Diamond Turning of Ductile Metals. Precision Engineer Center 1991 Annual Report, 9, 109-138, (1991).
- 9 Schaefer, J.P. Progress in Precision – Single Point Diamond Turning (SPDT) of Optical Components, Presented at ASPE 2002 Spring Topical Meeting on Progress in Precision, (2002).
- 10 Church, E.L., P.Z. Takacs, Survey of the Finish Characteristics of Machined Optical Surfaces. Optical Engineering, Vol. 24, No.3, 1985, 396-403.
- 11 Ogleza, A.A., D.L. Decker, P.C. Archiblad, D.A. O'Conner, E.R. Bueltmann. Optical Properties and Thermal Stability of Single-Point Diamond-Machined Aluminum Alloys. Proceedings of the SPIE - The International Society for Optical Engineering, v 966, 1989 Conference: Advances in Fabrication and Metrology for Optics and Large Optics, 17-19/08/198.
- 12 Drescher, J.D., Tool Force, Tool Edge, and Surface Finish Relationships in Diamond Turning. PhD Thesis, North Carolina State University, (1991).
- 13 Arcona, C., Tool Force, Chip Formation, and Surface Finish in Diamond Turning. PhD Thesis, North Carolina State University, (1996).

- 14 Abler, J.A., Process Modeling and Correction of Dynamic Errors in Diamond Turning. PhD Thesis, North Carolina State University, (1994).
- 15 Alexander H. Slocum, “Precision Machine Design” 1994 John Wiley, New York.
- 16 Bennett, J.M., L. Mattsson., Introduction to Surface Roughness and Scattering. Optical Society of America, Washington, D.C., 1989, pp 44-47.
- 17 Thrane, N., J. Wismer, H.Konstantin-Hanson and S. Gade. Practical use of the “Hilbert transform”, Brüel & Kjær, Denmark.  
<http://www.bksv.com/pdf/Bo0437.pdf>.
- 18 Matweb Material Property Data. Blacksburg, Virginia. <http://www.matweb.com>
- 19 Hegge, M.J., J.W. Baer, L.M.R Hardaway, G. Taudien, D.S. Sabatke, S.R. Shidemantle, J.J. Santman, and L.E. Comstock. Diamond Turned, Light Weight, Athermal, Visible TMA Telescope for the Planned New Horizons Mission to Pluto. Proceedings of SPIE Vol. 5877, Bellingham, WA, 2005.
- 20 Moriwaki, T., K. Okuda, “Machinability of Copper in Ultra-Precision Micro Diamond Cutting”, Annals of the CIRP, Vol. 38, No. 1, 1989. 115-118.
- 21 Falter, P.J., Diamond Turning of Nonrotationally Symmetric Surfaces. PhD Thesis,

North Carolina State University, (1990).

- 22 Dow, T.A., K. Garrard, L. Lamonds, and A. Sohn. Modeling of Vibration and Dithering in SPDT. Precision Engineering Center 2006 Interim Report, 25-36, 2006.
- 23 Thomson, W.T. and M.D. Dahleh. Theory of Vibration and Applications. Prentice Hall, Upper Saddle River, New Jersey. 5<sup>th</sup> ed., 1998.
- 24 Dow, T.A., L. Lamonds, Fabrication of Optical Surfaces and Fiducials, Precision Engineering Center 2005 Annual Report, 23, 85-107, (2006).
- 25 Dow, T.A., N. Wanna, Design of Reflective Optical Systems, Precision Engineering Center 2005 Annual Report, 23, 27-49, (2006).
- 26 Sphericity and radius of curvature metrology. Tucson, AZ. <http://www.phase-shift.com/products/interferometer-sphericity.shtml>.
- 27 Stover, J.C., Optical Scattering : Measurement and Analysis. McGraw-Hill, Inc., New York, New York. 1990.
- 28 Wanna, N.G. Design of Reflective Optical Systems. Masters Thesis, North Carolina State University, (2006).

- 29 Smith, W.S. The Scientist and Engineer's Guide to Digital Signal Processing. 2<sup>nd</sup> ed. California Technical Publishing, San Diego, California. 1999.
- 30 United States Patent 6,969,840 B1. Imaging Optical System including a Telescope and an Uncooled Warm-Stop Structure. P Chris Theriault, Rudolph E. Radau, Jr. (2005).
- 31 Doyle, K.B., V. Genber, G. Michels. Integrated Optomechanical Analysis. SPIE – The International Society for Optical Engineering, Bellingham, Washington. 2002.
- 32 Abler, J., P. Ro. Slide Motion Control of the DTM for Vibration Reduction. Precision Engineering Center 1990 Annual Report, 8, 285-306, (1990).
- 33 Woodside, R.M. Metrology of Reflective Optical Systems. Masters Thesis, North Carolina State University, (2006).
- 34 Juergens, J.C., R.H. Shepard III, J.P. Schaefer. Simulation of Single Point Diamond Turning Fabrication Process Errors. Proceedings of SPIE Vol. 5174 Novel Optical Systems Design and Optimization VI, 93-104. Bellingham, WA, 2003.

- 35 Takasu, S., M. Masuda and T. Nishiguchi. Influence of study vibration with small amplitude upon surface roughness in diamond machining. *Annals of the CIRP*, Volume 34 1 1985, pp. 463–467.
- 36 Hilbert from Wolfram.

## **6 APPENDIX**

## 6.1 APPENDIX A: MATLAB PROGRAMS

### 6.1.1 *Surface finish model with machine vibration and tool dithering*

#### MATLAB Program: dither\_3d

```
% Tool dithering model using circular tool cusps with z-axis/spindle  
% asynchronous motion.  
  
% Parameters of Motion & Finish  
feed      = 5;          % feedrate          (um/rev)  
tool_rad   = 570;        % tool radius        (um)  
rad_wp     = 20000;       % workpiece radius   (um)  
theta_offset = 0.;  
  
w_Hz      = 63.6;        % spindle motion frequency (Hz) %  
amp_spin   = 0.011;       % spindle motion amplitude (um)  
W_rpm     = 500;         % spindle speed        (rev/min)  
  
amp_dith   = 0*feed;      % dithering amplitude   (um)  
dith_ratio = amp_dith;  
lambda     = 40.56565656; % dithering frequency   (cycles/rev)  
  
% Parameters of the Model  
w         = w_Hz * 2*pi ; % convert (2Pi_rad/1_rev)  
W         = W_rpm * 2*pi/60; % convert (above * 1_min/60_sec)  
num_pts   = 401;  
num_pass  = 10;  
  
% Create vectors for tool center grid  
x         = 0 : feed : feed*num_pass;  
theta     = linspace(feed*num_pass/rad_wp,0,num_pts);  
%theta    = theta + 2*pi*theta_offset;  
  
% Create Tool Center Grid & Axis Vibration Depths  
[X, Theta] = meshgrid(x,theta);  
Z_tip     = amp_spin * sin(w/W * 2*pi*(X+feed*Theta/2/pi)/feed);  
  
% Modify X Centers to Model Dithering (Sinusoidal, Uniform and Normal).
```

```

% + amp_dith * sin (lambda * 2*pi*(X + feed*(Theta/2/pi))/feed);
% + ones(num_pts,1) * (rand(1,length(x))*feed*dith_ratio-feed*dith_ratio/2);
% + ones(num_pts,1)* random('Normal',0,dith_ratio*.333333,1,length(x));
X_dith = X + ones(num_pts,1)* random('Normal',0,dith_ratio*.333333,1,length(x));

% Create tool edges
x_plot = linspace(0,feed*num_pass,num_pts);
Z_plot = zeros(num_pts,num_pts);
Zc = abs(min(Z_tip(:))) + tool_rad;

% Create grid for drawing 2D traces
[X_plot,Theta_plot] = meshgrid(x_plot,theta);

% Loop to draw traces (Inner loop for each trace, outer loop for each
% trace) with result in Z_plot.
for l = 1:num_pts
ll=num_pts-l+1;
for k = 1:num_pts
Z_plot(ll,k) = min(-sqrt(tool_rad^2 - (x_plot(k) - X_dith(ll,:)).^2) + Z_tip(ll,:) + Zc );
end;
end;

% Plot 2D trace
figure, plot(x_plot, Z_plot(1,:), 'r-+', X_dith(1,:), Z_tip(1,:) + abs(min(Z_tip(:))), 'g.');

%plot 3D trace
figure, [Xi,Yi,Zi,Zc] = surf3([X_plot(:),Theta_plot(:)*rad_wp,Z_plot(:)], [401 401 1], 'nearest');
tstr = {[ ' Spindle ',' Z-axis ',' Dither ' ] ;...
[num2str(W_rpm,'%6.0f'), ' rpm = ', num2str(W_rpm/60,'%6.2f'), ' Hz ' ,...
num2str(w_Hz,'%6.2f'), ' Hz ', num2str(lambda*W_rpm/60,'%6.2f'), 'Hz' ];...
['z-cycles/rev = ', num2str(w/W,'%6.2f') ] ;...
['dithers/rev = ', num2str(lambda,'%6.2f'),...];
];
title(tstr,'FontName','Arial','FontSize',14,'FontWeight','Bold');
xlabel('X (μm)', 'FontName','Arial','FontSize',14,'FontWeight','Bold');
ylabel('Y (μm)', 'FontName','Arial','FontSize',14,'FontWeight','Bold');
zlabel('Z
(μm)', 'FontName','Arial','FontSize',14,'FontWeight','Bold','Rotation',0,'Position',[-1,-1,0]);
set(gca,'DataAspectRatio',[1 1 .7e-3]);

```

```

% alternative 3D plots commented out
% figure, surf(Z_plot);
% figure, plot3k([X_plot(:,Theta_plot(:)),Z_plot(:)]);

% Calculate Surface Statistics
Stats      = metro(Z_plot');
[pv, pv_trace] = max(Stats.Rt);
[rms,rms_trace] = max(Stats.Rq);
pv         = pv *1000;
rms        = rms*1000;

test = metro(Z_plot(100,:)); rms2 = test.Rq*1000, pv2 = test.Rt*1000;

```

### 6.1.2 Hilbert Transform with Decay Fit and Autocovariance

#### MATLAB Script: linear\_fit.m

```

%set variables
feed = 5;
feed_factor = 0;
dith_ratio = feed*feed_factor;
amp_dith = dith_ratio;

% Call machine vibration & tool dither program
dither_3d;

% Calculate autocovariance of profile
figure, [r,g,t]=autocovariance([x_plot' Z_plot(50,:)'-mean(Z_plot(50,:))],'-+r');
close(gcf);

% Calculate Hilbert transform
gh = abs(hilbert(g));

% Call MATLAB curve fit function and plot autocovariance, Hilbert transform &
% curve fit
ghfit = fit(t(1:375), gh(1:375)/gh(1), 'poly1');%exp1')
figure, plot(t(1:375), gh(1:375)/gh(1), 'b', t(1:375), ghfit.p1*t(1:375)+ghfit.p2, 'r', t, g/g(1)
,'g');
feed_factor, ghfit.p1,ghfit.p2

```

### MATLAB Function: autocovariance.m

```
function [rms_out, g_out, Tau_out] = autocovariance (array,pltopts);

% function [rms_out, g_out, Tau_out] = autocovariance (array);
%
% Calculates the autocovariance of a 2D surface trace.  Expects a (nx2)
% matrix input.  Array(:,1) = trace length vector. array(:,2)= trace
% hieght vector.

error(nargchk (2,2,nargin));
error(nargoutchk(0,3,nargout));

N    = length(array);
g    = zeros(N,1);

x = array(:,1);
z = array(:,2);

for l = 0:(N-1)
    for n = 1:(N-l)
        g(l+1) = g(l+1) + (z(n)*z(n+l));
    end
    g(l+1)= g(l+1) / N;
end

Tau=x;
plot(Tau,g,pltopts);

total = 0;
for n = 1:N
    total = total + z(n)^2;
end;
rms = sqrt(total/N);

title (['Autocovariance (rms = ', num2str(rms),')'])
xlabel('Lag Length ');
ylabel('G(z) (z-unit)^2','Rotation',0);

if nargout >= 1
    rms_out = rms;
    if nargout >= 2
```

```

g_out = g;
if nargout == 3
    Tau_out = Tau;
end;
end;
end;

```

### 6.1.3 Theoretical Tool Nose Radius & DOC Alignment

#### MATLAB Function: plot\_tool\_nose.m

```

function [out] = plot_tool (tool_rad, feed, num_passes, x_offset, z_offset, plot_opts)
%
%Generate a plot of diamond tool nose radius using the parabolic
%approximation.
%
%Input
% tool_rad radius of the diamond tool
% feed distance per pass
% num_passes number of passes in the plot
% x_offset x offset for generated theoretical tool path
% z_offset z offset for generated theoretical tool path
% plot_opts plot window options
%
%Output
% out data in the plot array ([x z])
%
%function [out] = plot_tool (tool_rad, feed, num_passes, x_offset, z_offset, plot_opts)

%check for correct input & output syntax

error(nargchk (2,6,nargin));
error(nargoutchk(0,1,nargout));

%create tool

x_tool = -feed/2: feed*0.001 :feed/2;
z_tool = (x_tool.^2)/(2*tool_rad);
x_plot = [];
z_plot = [];
count = 0;

```

```

%repeat tool if values input

if nargin <3
    num_passes = 3;
end;

for n = 1:num_passes %feedrate:(plot_data(half_pts,1) - plot_data(1,1))
    x_temp = x_tool + (feed*count);
    x_plot = [x_plot x_temp];
    z_plot = [z_plot z_tool];
    count = count +1;
end;

%If input, set offsets

if nargin >= 4
    x_plot = x_plot + x_offset;

    if nargin >=5
        z_plot = z_plot + z_offset;
    end;
end;

%set default plot options

if nargin <= 5
    plot_opts = '-r';
end;

%generate plot of tool

plot (x_plot, z_plot, plot_opts);

%check for output variable and fill if available

if nargout > 0
    out = [x_plot' z_plot'];
end;

```

## MATLAB Script: Depth of Cut Change Alignment

```
% Import MetroPro data and flip data in Y-dirction--only do once
[zz,y,x,hdr]=import_metropro('10mid100x.dat','bpmrsnk');
y=flipud(y);

% Call Slicer (Graphical Program by K. Garrard) and export data as "data_slice"
save 1mid100.mat

% Rotate trace to horizontal and plot results
theta= atan(.000050/.055);
ytrace = data_slice.z + data_slice.x*theta*1000;
xtrace = data_slice.x;
plot(xtrace,ytrace);

% generate theoretical matrix and close plot created by plot_tool_nose.m
feed      = 5.2296;
count     = 10;
tool_rad  = 770;
x_offset  = 4.5;
z_offset  = .014;
[theory]  = plot_tool_nose (tool_rad,feed,count,x_offset,z_offset);
close(gcf)

% generate final tool pass as cause by instant DOC change
x_tool    = -feed/2: feed*0.001 :feed*3;
z_tool    = (x_tool.^2)/(2*tool_rad);
x_tool    = x_tool' + count*feed + x_offset;
z_tool    = z_tool'           + z_offset;
theory = [ [theory(:,1); x_tool] [theory(:,2); z_tool] ];

%scale to match MetroPro data output
theory(:,1)=theory(:,1)/1000;

% open new figure to plot theoretical and actual simultanesously
figure;
hold;
plot( theory(:,1), theory(:,2),'r');
plot( xtrace    , ytrace    );
hold;
```

#### 6.1.4 Two Mirror Scripts

##### MATLAB Script: primary.m

```
% Variables
r = 300;
c = 1/r;
K = -1.019483;
y = 12:.049:74;
tool_rad = 3.125;

y_length = length(y);

% Formula for a conic and radius compensation
z = c .* (y.^2) ./ (1+sqrt(1-(1+K).*(c^2).*(y.^2)));
[x_tool, z_tool]=radius_comp (y,z,tool_rad,'concave');

theta = 0:(.1/180*pi):(359.9/180*pi);

% Plot desires surface, compensated tool path, and circles representing
% tool radius to verify that tool is normal
plot(z,y,'r',z_tool,x_tool,'b',...
sin(theta)*tool_rad+z_tool(2),cos(theta)*tool_rad+x_tool(2),'g',...
sin(theta)*tool_rad+z_tool(y_length/2),cos(theta)*tool_rad+x_tool(y_length/2),'g',...
sin(theta)*tool_rad+z_tool(y_length-1),cos(theta)*tool_rad+x_tool(y_length-1),'g');

% Offset z so apex of tool reference point and feed data into a matrix
z_tool = z_tool - tool_rad;
coords = [x_tool z_tool];
count = length (x_tool);

% Output tool matrix into a text file for the ASG-2500 controller. Write
% once ONLY.
% fid = fopen('primir_f.mm','w');
% fprintf(fid,'units mm\n\n');
% 
% for n = count:-1:1
% 
%   fprintf(fid, 'line %10.6f %10.6f feed\n', coords(n,:));
% end;
%
% status = fclose(fid);
```

### MATLAB Script: secondary\_f.m

```
% Set variables and add points beyond center and OD.  
r = -88.122476;  
K = -2.166620;  
tool_rad = 3.135;  
y = 0:.026551:20.695; % 1mm past od  
y = y-0.026551; % satisfy radius_comp with a point past center  
c = 1/r;  
  
y_length = length(y);  
  
% Calculate Conic surface and perform radius comp.  
z = c .* (y.^2) ./ (1+sqrt(1-(1+K).*(c^2).* (y.^2)));  
[x_tool, z_tool] = radius_comp (y,z,tool_rad,'concave');  
  
theta = 0:(.1/180*pi):(359.9/180*pi);  
  
% Plot surface, tool path, and circles to represent tool.  
figure,plot(z,y,'b-', z_tool,x_tool,'g-',...
sin(theta)*tool_rad+z_tool(2),cos(theta)*tool_rad+x_tool(2),...
sin(theta)*tool_rad+z_tool(y_length/2),cos(theta)*tool_rad+x_tool(y_length/2),...
sin(theta)*tool_rad+z_tool(y_length-1),cos(theta)*tool_rad+x_tool(y_length-1));  
  
z_tool = z_tool - tool_rad;  
coords = [x_tool z_tool];  
  
% Output tool path to a text file for the ASG-2500 controller. Write ONLY  
% once.  
% count = length (x_tool);  
%  
% fid = fopen('secmir_f.mm','w');  
% fprintf(fid,'units mm\n\n');  
%  
% for n = count:-1:2 % don't put neg x point in .mm file  
%  
%   fprintf(fid, 'line %10.6f %10.6f feed\n', coords(n,:));  
%  
% end;  
%  
% status = fclose(fid);
```

### 6.1.5 Spiral Alignment for Vibration Analysis

#### MATLAB Script: spiral\_align.m

```
% Prepare measured surface data (high point density) for plot fuction
% (surf)
[Xi,Yi] = meshgrid(linspace(min(x),max(x),201),linspace(min(y),max(y),201));
Zi = griddata(x,y,zz,Xi,Yi,'linear',{'QJ'});
Zi = Zi-max(max(Zi))-0.1;

% Draw contour plot of prepared surface
cla;
surf(Xi,Yi,Zi,'EdgeColor','none')      % draw contour plot
set(gca,'FontWeight','Bold');
set(gca,'DataAspectRatioMode','Manual','DataAspectRatio',[1 1 1]);
view([0 90]);                         % view plot from above without a grid
grid('off');

% Calculate point density in spiral for original measured data and for the
% interp2 MATLAB function which is called after this program to find spiral
pt_density = 0.9 / 640;                % mm/(data points = pixels)
base_circum = 2*pi*0.284;              % mm
theta_num = base_circum/pt_density;    % mm/mm*data points = data_points

% Calculated points on spiral in polar coordinates
theta = linspace(0,5*2*pi,1270*5);    % 1270 points per rev and 5 revolutions
r = 0.058 + theta/2/pi*0.039;
theta = theta + 2*pi*.17;

% Convert to Cartesian coordinates for plotting, adjust spiral center, and
% plot spiral on contour plot.
[x_spir,y_spir] = pol2cart(theta,r);
x_spir = x_spir+0.508;
y_spir = y_spir+0.360;
hold on
plot(x_spir,y_spir,'ok')
hold off
```

Some of the preceding programs called routines written by K. Garrard. They are freq.m  
(for FFT analysis and packaging which calls magphase.m, cplxfilt.m and plotfreq.m)

metro.m (simple surface statistics of PV, RMS, Roughness average), import\_metropro.m (import MetroPro data file), export\_metropro.m (export to MetroPro data file) and radius\_comp.m (calculate normal vector of a point from the slope between the next and previous point).

## 6.2 APPENDIX B: ASG-2500 DTM PROGRAMS FOR TWO MIRROR

### Primary roughing program using 0.1057 mm tool: primir\_r.mm

```
!using .0157 tool
!programing center of tool

units mm

move 74.0      15.0      250
move 74.0      10.0      50
move 74.0      9.230    feed
dwell 0
line 73.959713 9.222894 feed
line 73.910721 9.210823 feed
```

---removed all but first two and last two commands for brevity---

```
line 12.044758 0.347577 feed
line 11.995767 0.345613 feed
dwell 1000
move 12.0      15.0
move 74.0      15.0
```

### Primary finish program using 3.135 mm tool: prmir\_f.mm

```
units mm

move 73.286    20.0      250
move 73.286    9.5       25
move 73.286    9.041    feed
```

```

dwell 0
line 73.237392  9.029522  feed
line 73.188625  9.017506  feed

---removed all but first two and last two commands for brevity---

line 11.923593  0.239445  feed
line 11.874847  0.237491  feed

dwell 1000
move 11.875      20.0       250
move 73.286      20.0       250

```

Primary Fiducial program using 0.1057 mm tool: prifid.mm

```

units mm

move 7          16  250
move 7          0   250
line 0          0   10
line -0.1396299 16  10
move 7          16  250

```

Secondary roughing program using 0.1057 mm tool: secmir\_r.mm

```

units mm

move 20.707      5       250
move 20.707     -2.        25
move 20.707    -2.392      10

dwell 0

line 20.680087  -2.386074  feed
line 20.653522  -2.380041  feed

---removed all but first two and last two commands for brevity---

line 0.026583  -0.000004  feed

```

```
line  0.000000  0.000000  feed  
  
dwell 1000  
move  0          1          10  
move  0          5          250  
move  20.707    5          250
```

Secondary finish program using 3.135 mm tool: secmir\_f.mm

```
units mm  
  
move  21.376      5.0       250  
move  21.376      -2.2      25  
move  21.376     -2.467     feed  
  
dwell 0  
line  21.350962  -2.461295 feed  
line  21.324012  -2.455175 feed
```

---removed all but first two and last two commands for brevity---

```
line  0.027496  -0.000004  feed  
line  0.000000  0.000000  feed  
dwell 1000  
  
move  0.0        1.0       feed  
move  0.0        5.0       250  
move  21.376     5.0       250
```

Secondary fiducial program using 0.1057 mm tool: secfid.mm

```
units mm  
  
move  7          9          250  
move  7          0          250  
line  0          0          10  
line  -0.078542  9          10  
move  7.0        9          250
```

Tube primary fiducial: tubeprim.mm

units mm

```
move -84      5      250
move -84      0      250
line -75.82443 0      7.5
circle -76.36490 -7.5197 7.5 60.5197 ccw
line -76.36490 -17    7.5
line -74     -19.8129 7.5
move -74      5      250
move -84      5      250
```

Tube secondary fiducial: tubeseco.mm

units mm

```
move -84      5      250
move -84      0      250
line -76.777395 0      7.5
circle -76.2932 -4.5197 7.5 60.5197 ccw
line -76.2932 -14    7.5
line -74     -16.2932 7.5
move -74      5      250
move -84      5      250
```